Thermodynamics Laboratory
Aerospace and Mechanical Engineering Department

Faculty of Applied Sciences
University of Liège

Frost Accretion and Distribution in Heat Exchangers of Refrigeration Systems, Accounting for Surface Wettability

Author:
Antoine Parthoens

Supervisor:
Pr. Vincent Lemort

A thesis submitted in fulfillment of the requirements for the degree of

Doctor of Applied Sciences

Liège, March 2022

Frost accretion and distribution in heat exchangers of refrigeration systems, accounting for surface wettability

Thermodynamics Laboratory
Aerospace and Mechanical Engineering Department
Faculty of Applied Sciences - University of Liège
Allée de la Découverte 17
B-4000, Liège (BELGIUM)
a.parthoens@uliege.be
+32 498 53 23 53

Members of the Examination Committee:

Pr. Dr. Ir. Vincent Lemort, *Supervisor*
(University of Liège, Belgium)

Pr. Dr. Ir. Tristan Gilet
(University of Liège, Belgium)

Pr. Dr. Ir. Chrisitan Hermes
(Federal University of Santa Catarina, Brazil)

Pr. Dr. Ir. Romuald Rulliere
(INSA Lyon, France)

Pr. Dr. Ir. Michel De Paepe
(Ghent University, Belgium)

Dr. Ir. Eric Winandy
(Emerson Climate Technologies GmbH , Germany)

Pr. Dr. Ir. Pierre Dewallef
(University of Liège, Belgium)

"*All in all it's just another brick in the wall*"

Roger Waters

Abstract

Antoine Parthoens

Frost Accretion and Distribution in Heat Exchangers of Refrigeration Systems, Accounting for Surface Wettability

Frost accretion in heat exchangers of refrigeration systems is a major issue involving energy consumption penalty in the heating or cooling devices. Numerous studies try to suppress, or at least delay, this frost formation. Among them, the use of (super-)hydrophobic coatings has shown encouraging results. The present thesis aims at investigating one step further the use of such materials in a heat pump evaporator.

The first step is to understand the physical phenomena involved in such process. A first classical heat pump has been built and has been highly instrumented, especially around the evaporator. At this stage, the surface of the fins and tubes evaporator is classical aluminum. It allows to get a very fine understanding of the frost problematic in these devices. In parallel another test rig is set up, to understand how frost may behave on superhydrophobic surfaces on elementary geometries, such as flat plates. Beside the the physical phenomena observation, those test benches allow to build a experimental data set.

Based on observations, new simulation models are implemented. A segment-by-segment discretization is envisaged for the modeling of the evaporator. It allows to get independent frost layers on each tubes, as observed during the experimental campaign. An originality of this model is to account for the fin thermal conductivity, which is determinant in the frost distribution through the device. For numerical robustness, the model is implemented as a dynamic one. A modeling work is also conducted at the surface scale. It accounts for major parameters impacting the macroscopic scale, such as contact angles or roughness. The major objective of this model is to predict the nucleation time (defined here as the time necessary, for a given surface, to be fully covered by frost nuclei).

The next step is, still separately, to compare the measurement results to the model predictions. At the evaporator scale, the results are compared for the refrigerant side and for the air side in dry, wet or frosted conditions. This allows to successfully validate the model and clearly underline the effect of the fin thermal conductivity. At the surface scale, the same task is conducted, leading to the validation of the model.

As models can now be trusted, the ultimate step of the work is to merge them to predict the performance of heat exchanger in frost conditions, with different surface characteristics. The main result found there is that a real frost delay can be observed compared to regular surfaces, only if the hydrophobic level is sufficiently high. Slightly hydrophobic materials do not have any significant impact while superhydrophobic ones are game changers.

Résumé

Antoine Parthoens

Frost Accretion and Distribution in Heat Exchangers of Refrigeration Systems, Accounting for Surface Wettability

L'accumulation de givre dans les échangeurs de chaleur des systèmes de réfrigération présente un problème impliquant des pénalités énergétiques au niveau des machines de climatisation. Un bon nombre d'études tente donc de diminuer, voire supprimer, cette formation de givre. Parmi elles, l'utilisation de matériaux (super-)hydrophobes semble montrer des résultats prometteurs. Cette thèse a pour but d'investiguer l'utilisation de tels matériaux dans un évaporateur de pompe à chaleur.

La première étape est de comprendre les phénomènes physiques en jeu dans un tel processus. Une pompe a chaleur à été construite et hautement instrumentée, principalement autour de son évaporateur. À ce niveau, la surface de cet évaporateur tubes et ailettes est de l'aluminium classique. Ceci permet une étude très fine de la formation de givre dans de tels composants. En parallèle, un banc est construit pour comprendre la formation de givre sur des géométries simples présentant un caractère hydrophobe. En plus de l'observation et la compréhension des phénomènes, ces dispositifs permettent de construire une banque de données expérimentales.

Sur base des observations faites préalablement, différents modèles numériques sont implémentés. Pour l'évaporateur, un modèle segment-par-segment est envisagé. Ceci permet d'avoir une prédiction de givre indépendante pour chacun des tubes, comme observé lors de la campagne d'essais. Une originalité apportée à ce modèle est la prise en compte de la conductivité thermique des ailettes, qui se montrera déterminante dans la répartition du givre au sein de l'échangeur. Pour augmenter la robustesse numérique, ce modèle est dynamique. Un travail de modélisation est aussi réalisé au niveau des phénomènes de surface. Ce dernier prend en compte des paramètres majeurs comme l'angle de contact ou la rugosité de la surface. L'objectif premier de ce modèle est de prédire le temps de nucléation (défini ici comme le temps nécessaire pour couvrir totalement de nuclei une surface donnée). L'étape suivante est de comparer les résultats des simulations avec les données expérimentales. A l'échelle de l'évaporateur, la validation est appliquée du côté réfrigérant, ainsi que du côté air, dans un régime sec, humide ou de givre. Cette étape permet de valider le modèle et de souligner explicitement l'impact de la conductivité thermique des ailettes. Le même processus est suivi à l'échelle de la surface.

Les différents modèles étant validés, ils sont ensuite fusionnés afin de prédire les performance d'un évaporateur avec un revêtement plus ou moins hydrophobe. Le résultat principal est qu'il faut une surface très hydrophobe pour observer une réelle différence au niveau de la formation de givre

Acknowledgements

In a very first time, I would like to warmly thank Professor Vincent Lemort for letting me accomplish my own journey, with a perfect balance between working structure and creativity freedom.

I am very grateful to the examination committee for their time dedicated in the reading and evaluating the present manuscript. I would also like to express my gratitude to FRS-FRNS (Fond de la Recherche Scientifique) for trusting me and giving me a 3-year+ FRIA grant.

Undoubtedly, a huge thank goes to the Thermodynamics Laboratory community, from academic staff to technicians or other PhD students. It was a real honor to evolve by your side. The toughest part of the journey is to leave this environment. All the best I can wish to a young researcher is to cross the road of this amazing team.

Then, I would like to thank Mathilde and more broadly my family, for providing me all the necessary love and support to accomplish this work !

And last but not least, I would like to give a special thank to Sam without whom this work would have been completely different (and not for the best). Sam was always super available, from Liège, Haifa or Brussels. He extensively brought scientific inputs, as much as good mood. Thanks.

Marcel

Contents

List of Figures

List of Tables

List of Abbreviations

ASHP	**A**ir **S**ource **H**eat **P**ump
BR	**B**lockage **R**atio
CA	**C**ontact **A**ngle
CD	**C**on**d**enser
COP	**C**oefficent **O**f **P**erformance
CP	**C**om**p**ressor
EV	**Ev**aporaor
EXV	**Ex**pension **V**alve
FTC	**F**ins **T**hermal **C**onductivity
HVAC	**H**eating **V**entilation and **A**ir-**C**onditioning
LG	**L**iquid **G**as
LT	**L**iquid **T**ank
RMSE	**R**oot **M**eans **S**quare **D**eviation
SG	**S**olid **G**as
SL	**S**olid **L**iquid
TC	**T**hermo**C**ouple

Physical Constants

g	gravity acceleration	$= 9.806\,65\,\mathrm{m\,s^{-2}}$
k	Boltzmann's constant	$= 1.380\,650\,4 \times 10^{-23}\,\mathrm{J\,K^{-1}}$
R	ideal gas constant	$= 8.314\,472\,\mathrm{J\,mol^{-1}\,K^{-1}}$

List of Symbols

SYMBOLS

A	exchange surface	m^2
AU	global heat transfer coefficient	$\mathrm{W\,K^{-1}}$
Bo	boiling number	-
Bn	Bond number	-
Co	convective number	-
$\dot{C}$	capacity flowrate	$\mathrm{W\,K^{-1}}$
D	diameter	m
D_v	vapor diffusivity	$\mathrm{m^2\,s^{-1}}$
f	friction factor	-
Fr	Froude number	-
H	heat transfer coefficient	$\mathrm{W\,m^{-2}\,K^{-1}}$
H_m	mass transfer coefficient	$\mathrm{kg\,m^{-2}\,K^{-1}}$
Ha	Hatta number	-
h	specific enthalpy	$\mathrm{J\,kg^{-1}}$
k	thermal conductivity	$\mathrm{W\,m^{-1}\,K^{-1}}$
L	length	m
Le	Lewis number	-
MM	molecular mass	$\mathrm{g\,mol^{-1}}$
$\dot{M}$	mass flow rate	$\mathrm{kg\,s^{-1}}$
$\dot{m}$	mass flux	$\mathrm{kg\,s^{-1}\,m^{-2}}$
NTU	number of transfer units	-
Nu	Nusselt number	-
Oh	Ohnesorge number	-
P	pressure	Pa *or* bar
Pr	Prandtl number	-
$\dot{Q}$	heat transfer rate	W
$\dot{q}$	heating flux	$\mathrm{W\,m^{-2}}$
T	temperature	K *or* °C
r	roughness factor, radius	-, m
Re	Reynolds number	-
RH	relative humidity	%
$\dot{V}$	volumetric flow rate	$\mathrm{m^3\,h^{-1}}$
We	Webber number	-
$\dot{W}$	mechanical or electrical power	W
x	vapor quality	-

GREEK SYMBOLS

η	efficiency	-
ω	absolute humidity	$\mathrm{kg_{water}\ kg_{air}^{-1}}$
θ	static contact angle	°
σ	surface tension/energy	$\mathrm{N\,m^{-1}}$ *or* $\mathrm{J\,m^{-2}}$

SUBSCRIPTS

$2P$	two-phase
CS	cross-section
dp	dew-point
eq	equilibrium
ex	exhaust
ext	external
$fict$	fictitious
fl	fluid
h	hydraulic
in	inside
L	liquid
lat	latent
ref	refrigerant
S	solid
sat	saturation
$sens$	sensible
su	supply
$surf$	surface
$thick$	thickness
tot	total
V	vapor
w	water
wb	wet-bulb

For Nany...

Chapter 1

Introduction

1.1 Energy Context and Heat Pump Technology

In the 19th century, industrial revolution brought many technological advances and energy consumption linked to it. Since that period, energy consumption and its impact on the climate change has never decreased. Few decades ago, the explicit link between the CO_2 emissions and Earth temperature increase was clearly exposed. For the planet preservation and economic reasons (e.g. Oil Crisis, 1973), fossil fuels alternatives were investigated.

Each energy consuming sector must do specific efforts to decrease its own impact and residential sector is one of them, representing a consequent part of the greenhouse gas emissions in the atmosphere (13% in the USA in 2019 [2]). HVAC (*Heating Ventilation and Air-Conditioning*) represents more than 50 % of the energy use in 2015 for houses of USA. If water heating and air-conditioning are added, it goes up to 73% [1]. Even if the concept is much older (Peter von Rittinger, 1855-1857 [95]), since the 1990's, the heat pump has established itself as the main alternative to fossil fuels-based heating systems, thanks to the technology maturity, components' improvement and new generation refrigerants [109]. IEA states that in 2010, heat pumps represented less than 3% of the purchasing for heating and hot water production. In 2019 the shares grew up to nearly 5%. To meet the SDS *Sustainable Development Scenario*, the share should rise up to 22% [35].

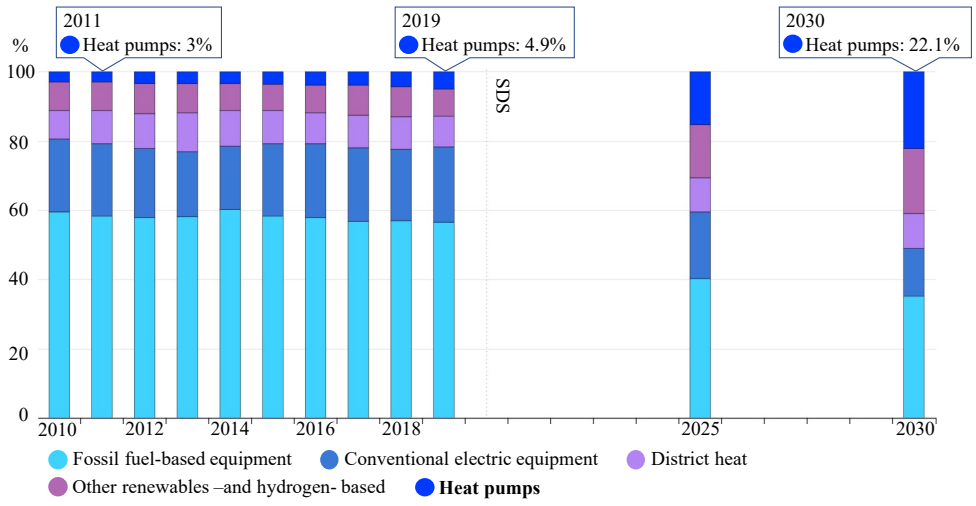

FIGURE 1.1: Share of households purchasing heat pumps for heating and hot water production in the Sustainable Development Scenario, 2010-2030 (North America, Europe and Northern Asia) [35]

A heat pump is a device based on a vapor compression cycle relying on heat source and heat sink. In its simple shape, it consists in four main components, namely the compressor, the condenser, the expansion valve and the evaporator. The working fluid, so called refrigerant, is running through a thermodynamic loop.

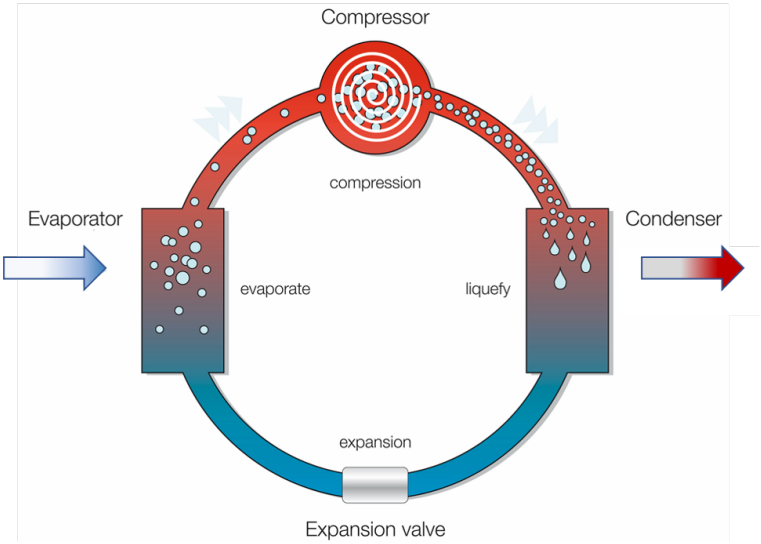

FIGURE 1.2: Working principle of a heat pump [30]

It aims at extracting energy from a heat source at a low temperature (evaporation), to deliver it to a heat sink at a higher temperature (condensation). This can be possible, paying the price of bringing to the system mechanical energy (compression) through an electric compressor. While a traditional electrical heater delivers 1 unit of heat for 1 unit of electricity consumed, the heat pumps device allows, for 1 unit of electricity spent, to deliver more than 1 unit of heat. The ratio between the useful heat transfer rate compared to the necessary electrical power (compressor and auxiliaries) is called *coefficient of performance* (COP). Depending on the set-up and conditions, normal values of COP range between 2 and 6. Combined to green electricity from renewable sources, this system is a clean and efficient solution for building heating and air-conditioning.

For the residential heat pumps heating and/or conditioning buildings, different type of systems exist.

First, the heat pump can be reversible or not. When a machine is reversible, it means that this only device can either heat the building up during cold days and cool it down during hot periods. It only needs an additional expansion valve and flow direction valves. Only a single compressor is required and the exchangers are the same (they switch their role, depending on the mode).

Even if heat pump applications are numerous (electric car conditioning, clothes dryer, building conditioning, industrial heat pumps,...) this thesis focuses on building heating and cooling. In this specific context, heat pumps can differentiate, depending on their heat source and sink. As shown in Figure 1.3, there are usually two kinds of heat sinks (i.e. media used to exchange heat with the rooms). The first solution is a hot water-loop[1]. This loop either directly runs through the floor or can be sent to

[1]For the sake of lightness, only heating mode is described. However, every concept can be transposed in cooling mode

convective devices (active or passive). The other common solution is to exchange the condensing heat transfer rate with an air flow, pulsed to the room, directly or through a duct network.

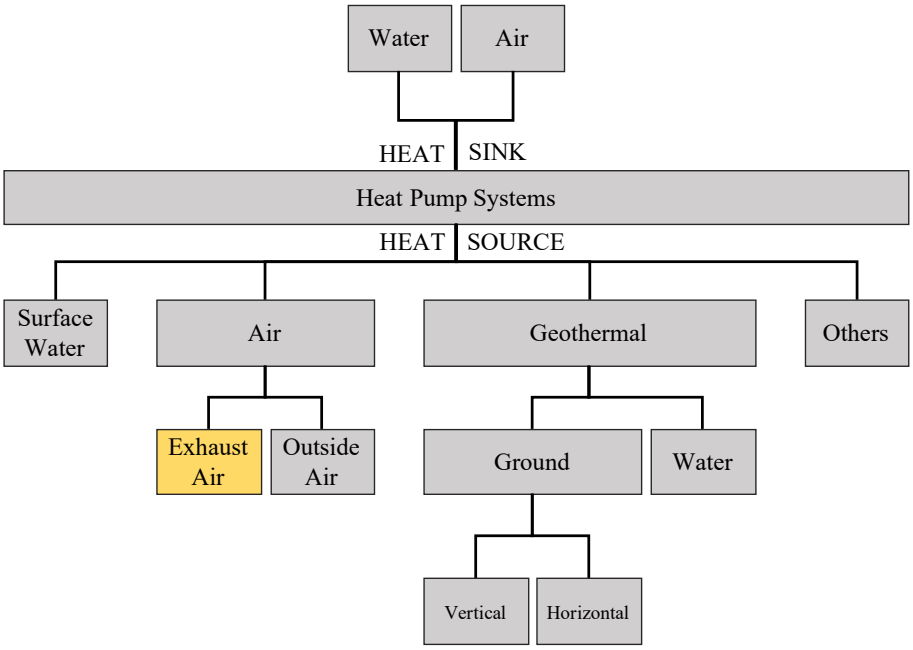

FIGURE 1.3: Heat pump classification regarding its heat source and sink

The heat sources (i.e. media in which the system extracts the energy, at a low temperature) are more varied. Even if Figure 1.3 is synthetic, plenty subsystems exist. Significant reviewing work has been conducted by different authors. Some of them are referenced here.

Heat pump devices can extract heat from surface level, such as lakes, rivers, oceans [31, 60]. Their potential is interesting, however they are not available everywhere. Another very common heat source is the air, which can either be from the outside atmosphere or from the ventilation extraction [12, 71]. The advantage is that the air is always available but its temperature can be very fluctuating, depending on season and location. A different technology consists in harvesting energy from the ground, through geothermal systems [55, 77, 80]. The main advantage is the deeper the drilling the more constant and the hotter the temperature. The counterpart is that the deeper the drilling, the more expensive. The aforementioned technologies are the most widespread. However, other more exotic systems can be found.

Among those systems, the air source heat pump (ASHP) imposed itself on the different markets. Figure 1.4 shows that from 2014 to 2025 proportion, the share of ASHP in the US market is much larger than water and ground source systems.

In heat pump and air conditioning systems in general, while heat exchangers are fed with air, they are the more often fed with humid air. This mixture exposes the system to condensing and frosting issues, detailed in the very next section.

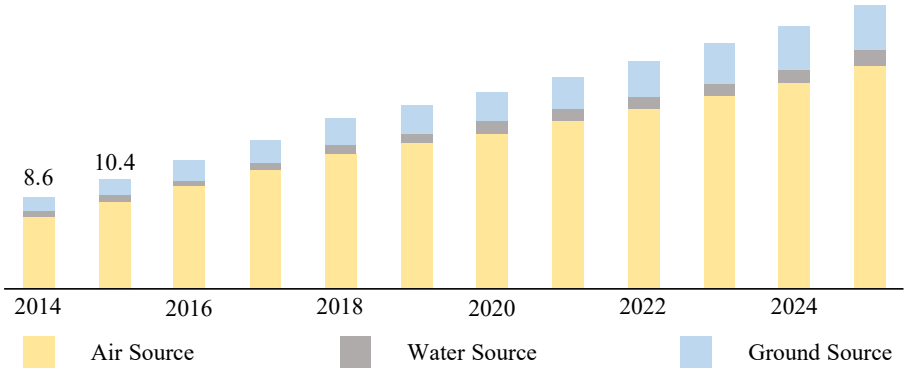

FIGURE 1.4: US heat pump market size, by technology, 2014-2025 (USD Billion) [73]

1.2 Frost Problematic in Refrigeration

As seen in Figure 1.5, if the evaporation pressure is under a given value (respectively 2.9 and 8 bars for R134a and R410a), the refrigerant shows negative temperatures. Depending on the air side conditions, it may lead to negative wall temperatures. If it is under the air dew-point, a frost event may happen.

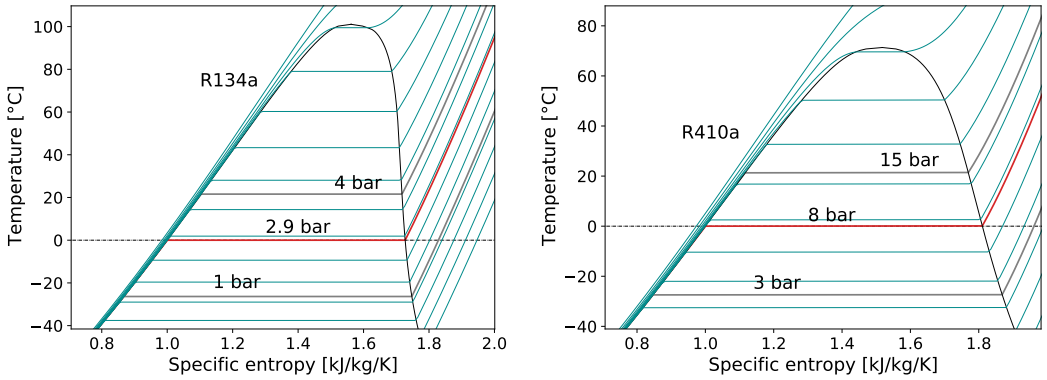

FIGURE 1.5: T-s diagram of R134a (left) and R410a (right) with different pressure levels

Frost formation can be a major problem in heat exchangers. Under certain conditions, so-called frosting conditions, a frost layer can form on the heat exchanger surface. This frost layer leads to a reduction of the cross-section area. Obviously, this reduction then generates an increase in the pressure drop through the heat exchanger and thus an increase in the electrical power delivered to the fans [86]. If the electrical power delivered to the fans remains constant, the air flowrate flowing through the heat exchanger decreases [13]. In extreme cases, the frost layer can create a full blockage of air flow passages [99]. Frost layer also corresponds to an additional thermal resistance that affects the exchanged heat transfer rate between the air stream and the refrigerant [103]. As a consequence, the evaporator energy performance will be affected by the presence of frost and will ultimately decrease the performance of the heat pump. Figure 1.6 illustrates the drop of heat transfer rate at the evaporator and the COP decrease of a heat pump, due to frost formation. The experimental data sets have been measured by respectively Yang et al. [102] and Yoo et al [105].

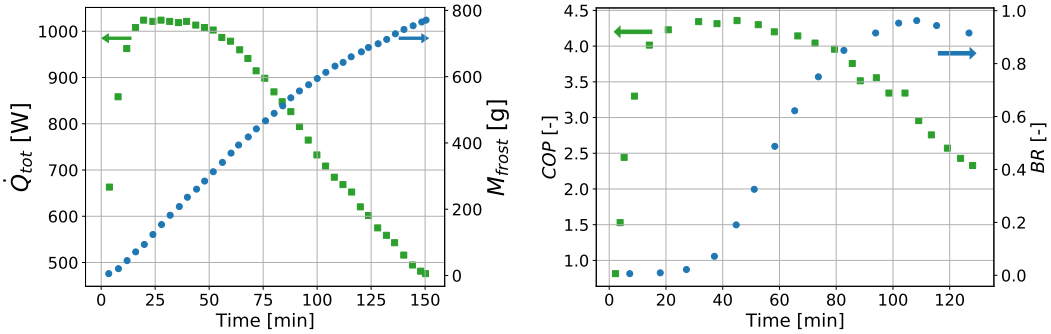

FIGURE 1.6: Left : Total heat transfer rate (green) decrease as mass of frost increases (blue). Experimental data from [102] - 2-column, 8-row fins and tubes heat exchanger - Right : heat pump COP (green) decrease as the blockage ratio (BR) of the evaporator (blue) increases [105] - fins and tubes heat exchanger

As the frost is a penalty, efforts are made to delay or suppress its appearance. Based on the review work of Nawaz and Fricke [66], methods can be classified in different categories.

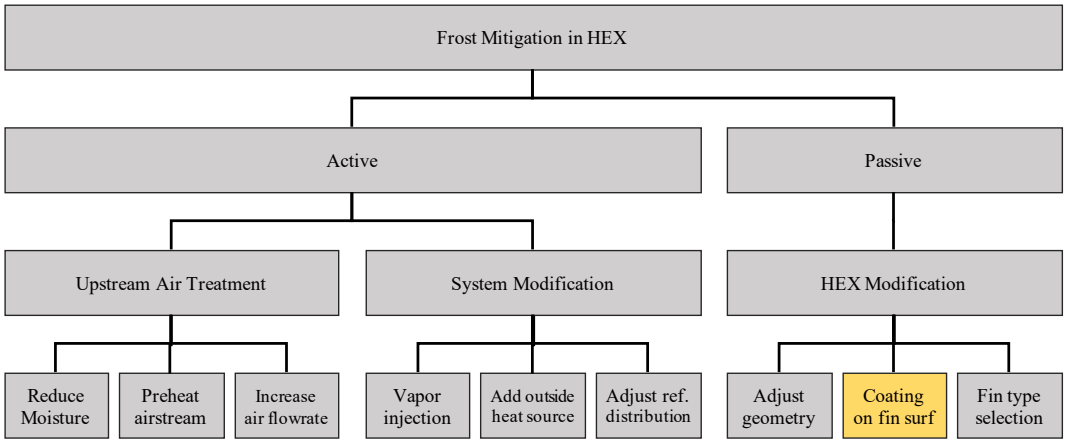

FIGURE 1.7: Classification of the different frost mitigation techniques in heat exchangers

Each of the methods listed in Figure 1.7 has their different strengths and drawbacks. The reader interested may find a more detailed description of each method in the dedicated review [66]. However, in the frame of this thesis, only the coating of the exchanger surface is put into light. Indeed, the fast progress in the surface treatment technologies places it as a very good candidate for the frost reduction. The system is passive, shows moderate costs of implementation and still gives encouraging results.

More precise description of the interactions between water and coated surfaces are detailed in the next section. But prior to that, a quick overview of frost growth phenomenon is explained here. A more exhaustive characterization is available in the dedicated section of the thesis (see Chapter 3). The frosting process has several different steps, as illustrated in Figure 1.8.

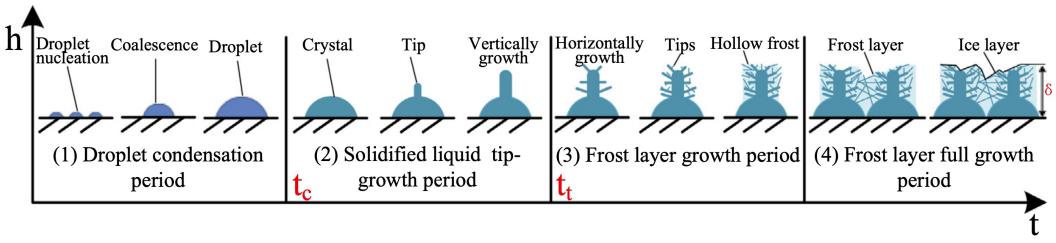

FIGURE 1.8: Different steps of frost development [85]

Depending on authors, different number of phases and names in the frost development occur. Even if Table 1.1 is not exhaustive, it sums the nomenclature widely found in the literature.

TABLE 1.1: Different frost growing phase, depending on authors

Source	Phase 1	Phase 2	Phase 3	Phase 4
[85]	Droplet condensation period	Solidified liquid tip-growth period	Frost layer growth period	Frost layer full growth period
[87]	Dropwise condensation period	Solidified liquid tip-growth period	Densification and bulk-growth period	-
[29]	Crystal growth period	Frost layer growth period	Frost layer full growth period	-

In the frame of this thesis, two main stages are considered. It is not a study focused on very specific stages of frost formation, meaning that two stages are consistent enough for the given context. The first stage is the early stage or nucleation phase. Microscopically it corresponds to the period between the dry surface and completely covered surface. The second stage is the frost growth period, corresponding to the process of frost formation during which the substrate has no more impact because it is already covered by frost.

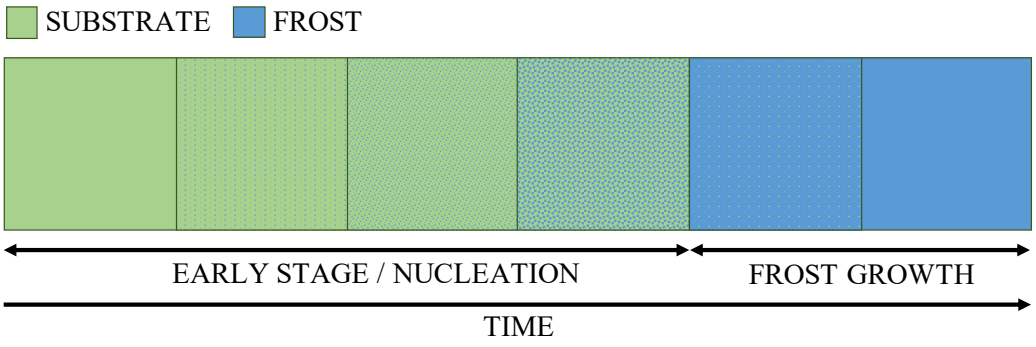

FIGURE 1.9: Different steps of frost development for the actual thesis

Therefore, delaying the frost apparition using hydrophobic coatings would correspond to the extension of the nucleation phase. As for the frost growth phase the substrate is not reachable, the hydrophobic effect disappears, leading to classical frost evolution. A special dedication to the early stage phase is made in this work.

1.3 Condensing on Specific Surfaces

Since ever, nature has evolved to take advantage of its environment. One key element for living beings is to correctly manage water, accordingly to its needs. The most famous example is the lotus leaf, showing water repelling characteristics. As water rolls on the leave, it allows it to easily eliminate dirt, stay dry and prevent from rotting.

On the other side, nature has to face very dry climates such as in deserts. However, life manages to survive by developing specific tricks to catch the very low humidity in the air. Jiu et al [37] explained that cactus collects fog in the air thanks to different mechanisms. Combining specific geometry of spines and surface with microgrooves, an advantageous Laplace pressure gradient and surface energy gradient, cactus drives humidity from air to its core for its absorption.

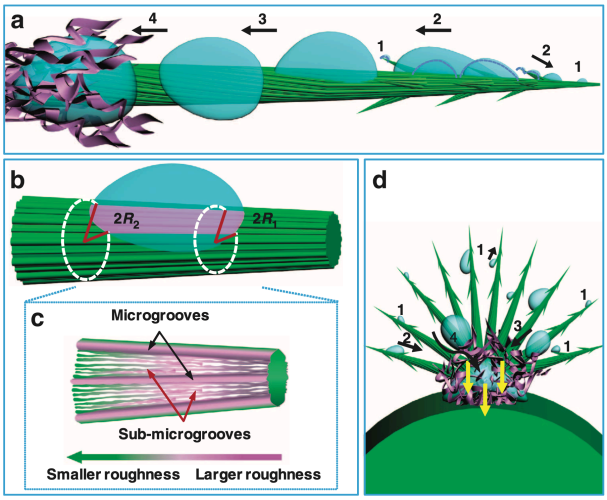

FIGURE 1.10: Mechanism of the fog collection on the cactus [37]

In the same order of ideas, Namb desert beetle has a very specific back. Parker and Lawrence [4] explain that alternating specific hydrophobic and hydrophilic patterns, fog can be collected by the animal and brought to its mouth, even in the dry, hot and windy climate of Namibian desert.

In the light of this, scientists get inspired from nature to develop artificial coatings. Biomimetics allows to reach *high performance* surfaces, as reviewed by Yue et al. [107].

The applications of such surfaces are very diversified. In aeronautics, aircrafts face very cold and humid environment. Humidity from the air freezes on the plane, modifying stall speed, increasing the global fuel consumption [8]. Recently, Laroche et al. [8] and Belaud et al. [46] developed promising materials to decrease this problematic.

The same problematic could be transposed for wind turbines. Indeed, because of ice, performance may decrease, but more impotently, an imbalance between blades can be observed, leading to degradation of the device [70]. Coating technologies may also prevent such undesired effects.

A different usage of such materials, as for the lotus leaf, may be found for surface cleaning. Showing hydrophobic properties, walls or glasses will repel water droplets

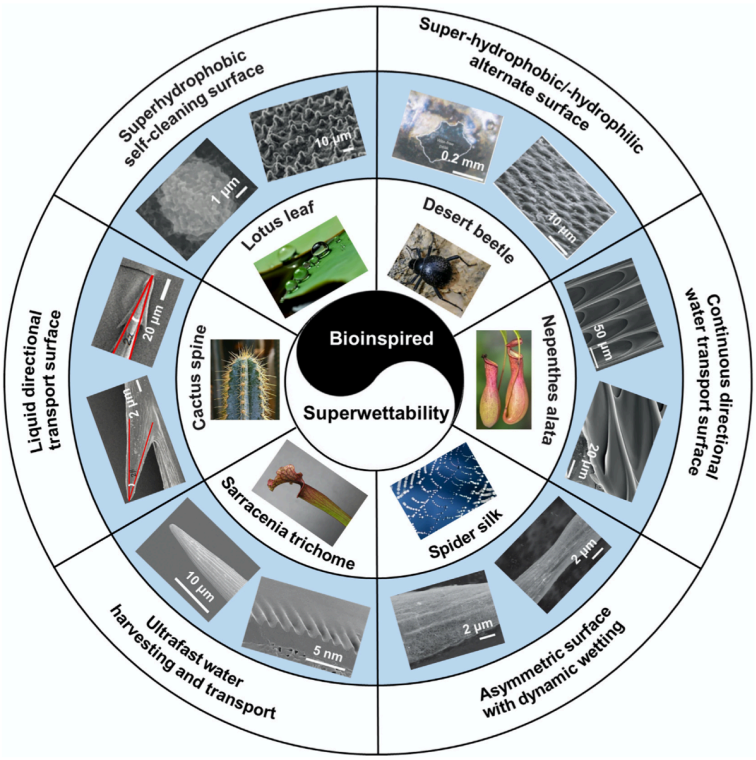

FIGURE 1.11: Inspiration from nature to develop efficient surfaces [107]

which are catching impurities, leaving a clean and healthy surface [72].

Even if the previous list is not exhaustive, the last application presented here is the application of coatings in heat exchangers. As detailed before, frost decreases their performance. Benefiting of such surface features may enhance the characteristics of the device. A more detailed investigation about it is detailed in this thesis.

To have a better understanding of the physics behind the special surfaces, **general considerations** are recalled here. As seen before, a given surface may have different affinity with water. This affinity, also called wettability, depends on its surface energy on one side and on its structure on the other side.

First, a perfectly smooth surface is considered. Its affinity with water then only depends on its surface energy. In the core of materials, atoms have generally a balanced set of bounds as they are surrounded by other atoms of the same nature. However, at its surface it is not the case. There are atoms willing to interact with their surrounding to create bounds and minimize their energy. If the interactions are strong, meaning that it has a high surface energy, it will easily attract water. Oppositely, if it has a low surface energy, it will not attract water very much.

Microscopically, the criteria to measure the hydrophobic nature is the contact angle θ, illustrated Figure 1.12. A surface is considered as hydrophilic (attracted by water) if its static contact angle θ is smaller than 90°. On the other side, if θ is larger than 90°, it is considered as hydrophobic (repelling water).

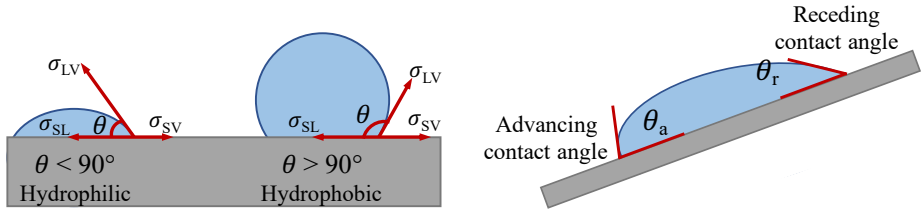

FIGURE 1.12: Static contact angle (left), dynamic angles (right)

Young established an equilibrium relation between the different surface tensions and the static contact angle for a droplet on an ideal homogeneous and smooth surface:

$$\cos(\theta) = \frac{\sigma_{SV} - \sigma_{SL}}{\sigma_{LV}} \tag{1.1}$$

Dynamic angles can also be defined, as shown in Figure 1.12 (right). The hysteresis angle is defined as the difference between the advancing and receding contact angles. A surface is considered as *superhydrophobic* if it shows a static contact angle greater than 150° and an hysteresis angle smaller than 10° [45]. Finally, the roll-off angle is defined as the angle of tilted surface at which a water drop starts to roll.

The previously defined contact angles, only depend on the surface energy if the surface is perfectly smooth. However, if surface shows some roughness, it will impact the apparent contact angles. The nature hydrophilic or hydrophobic is accentuated when increasing the roughness [82]. Basically, two main approaches are often considered. First there is the Wanzel model in which the drop penetrates the asperities as shown in Figure 1.13. The apparent contact angle is therefore accentuated by a roughness factor in the following way:

$$\cos(\theta^W) = r \cdot \cos(\theta) \tag{1.2}$$

where θ^W is the apparent contact angle and r is the roughness factor defined as:

$$r = \frac{\text{real surface area}}{\text{plannar surface area}} \tag{1.3}$$

As r is bigger than 1, if θ is smaller than 90° (hydrophillic situation), the apparent angle $\theta^\star$ will be smaller. In an opposite way, if θ is bigger than 90°, with the roughness factor, the apparent angle will be even more important leading to higher hydrophobicity. It can be physically understood in the following way (hydrophobic case): as the material fills asperities, the surface contact is increased. To avoid having a too large contact surface between liquid and solid phases, the droplet will contract, increasing its hydrophobic nature.

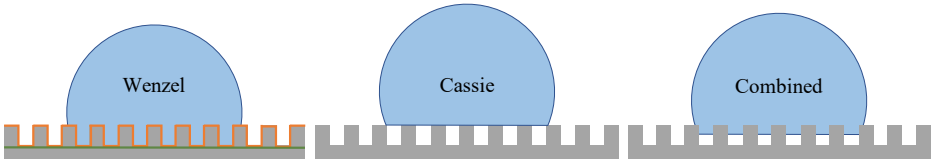

FIGURE 1.13: Wenzel, Cassie and combined model representation

The other approach considering rugosity, is the one described by Cassie. It suggests that the droplet stays completely on the top of the asperities, as shown in Figure 1.13. It leads to the CassieBaxter model:

$$\cos(\theta^C) = \varphi \cdot \cos(\theta) + (1 - \varphi) \cdot \cos(\theta_{\text{air}}) \tag{1.4}$$

φ being the fraction of solid compared to pores. Considering $\theta_{\text{air}} = 180°$ [74], Eq.(1.4) becomes:

$$\cos(\theta^C) = \varphi \cdot (\cos(\theta) + 1) - 1 \tag{1.5}$$

It is then possible to consider a hybrid situation (Figure 1.13) combining Eq.(1.2) and Eq.(1.4), leading to the more general model:

$$\cos(\theta^{CW}) = \varphi \cdot (r \cdot (\cos(\theta) + 1) - 1 \tag{1.6}$$

The above-mentioned models are the more famous ones, but there are others that have been developed.

As the ultimate goal is to delay frost, the focus is mainly set on surfaces showing hydrophobic characteristics. To understand the condensation and frost apparition on surface, lots of authors have experimentally studied the interactions between water and coated surfaces. A lot of them deeply consider very fundamental concepts such as the droplet structures or how a given droplet solidifies, regarding the coating [15, 51, 67, 92, 97, 108]. The precise phenomenon described in the above-mentioned publications are very insightful. However, their fundamental nature may be too specific for the present thesis. Nevertheless, studies also show, explicitly quantify and correlate the frost delay with the surface. Thanks to luminance meter technique Kim et al. [42] showed the direct frost retardation rate increasing with the static contact angle, going from 75 to 150°. On their side, Orbeli et al. [67] linked the rugosity characteristic size to the freezing delay. According to them, if the ice repelling is sought, it would be better to consider small size rugosity. Liu et al. [54] and Wang et al. [94] measured frost thickness as a function of time under natural convection. Both compared hydrophilic and nearly superhydrophobic materials, showing a clear advantage for the latter.

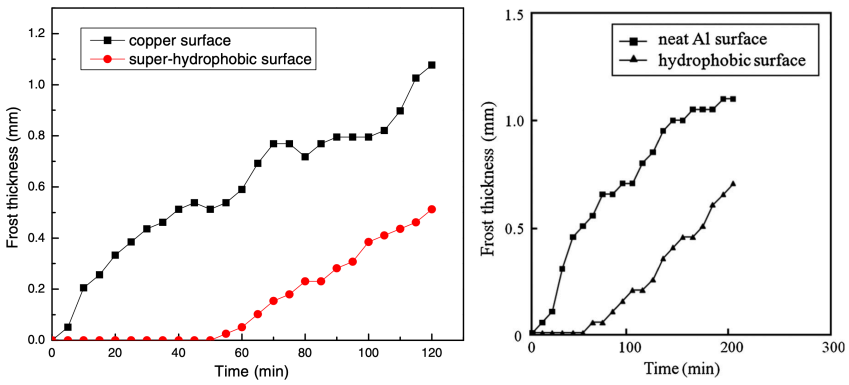

FIGURE 1.14: Frost thicknesses vs. time - Left [54] : Static CA 62 and 172°- Right [94] : Static CA 62 and 147°

The non-exhaustive surface investigations listed above show a direct link between the surface characteristic and the frost apparition. The objective here is to understand and describe nucleation at a scale which is sufficiently low to account for the substrate characteristics in a physical way but which is also sufficiently high to show

a significant impact at a macroscopic level.

1.4 Evaporator Characterization Under Frost Conditions

Frost formation in heat exchangers is not a new topic. Many authors already described uncoated devices. First, experimental investigations are necessary to observe behavior of systems showing frost accumulation. Based on the interpretation of the observed physical phenomena, equations are implemented to obtain numerical tools used to predict and design systems in such conditions.

1.4.1 Evaporator Experiments

As frost appears within the evaporator, its direct measurement is something complex. The available information is, in general, obtained via other quantities measurement. The easiest and still explicit evidence of frost accumulation is the progressive increase of pressure drop on the air side [18, 27, 49, 62]. Other indicators may also be interpreted as the presence of frost, such as refrigerant evaporating pressure or total heat transfer rate decrease.

If there is a willing to get a more precise characterization of frost, more specific studies are realized. For instance, Breque [11] studied a vehicle heat pump evaporator, remotely from the complete system. It allows to get a more comfortable access to some measurements such as mass or thickness measurement. The drawback of this system is that frost formation is investigated independently from the global heat pump behavior.

In the present thesis, a special dedication is brought to the frost measurement techniques but keeping the system as close as possible from the original one.

1.4.2 Evaporator Modeling

Many authors [18, 36, 43, 58, 63, 98, 103] developed different model of frost and of frost formation in the frame of heat exchanger devices. The different types of models are recalled in Section 3.2. Basically, the more precise the model, the more computational resource needed. However, relatively simple models, as described in the present thesis, can lead to satisfying prediction results.

A novelty in this thesis is to account for the fin thermal conductivity in the numerical models. Even if it is not new in heat exchangers without frost apparition [52, 75, 79, 83], from the best author's knwoledge, it is a first time that this phenomenon is accounted in heat exchangers with frost formation. It is seen in this work that it has a capital importance in the frost distribution predictions.

The other major contribution of this thesis is to consider surface phenomena at the exchanger scale. Indeed, as previously said, different work previously cited account for hydrophobic surfaces in the exchanger, but only in the frame of experimental works. The goal here is to merge surface modeling with macroscopic description of the evaporator. The ultimate result of the present thesis is then an efficient model of heat exchanger submitted to frost conditions, accounting for the surface wettability and fin thermal conductivity.

1.5 Thesis Objectives

The ultimate objective of the present thesis is to merge the macroscopic world of the heat exchanger and the surface world, to bring a new dimension in the frost modeling in such devices. This will allow to account for surface wettability and quantify the performance evolution in the simulation predictions.

Obviously, an add-on brought with this thesis is the surface models and nucleation phase description in the modeling of heat exchangers, which is, to the best author's knowledge, a world premiere. Furthermore, thanks to a deep experimental study, additional phenomena are brought to the existing models, such as fin thermal conductivity.

The thesis contribution is illustrated in Figure 1.15.

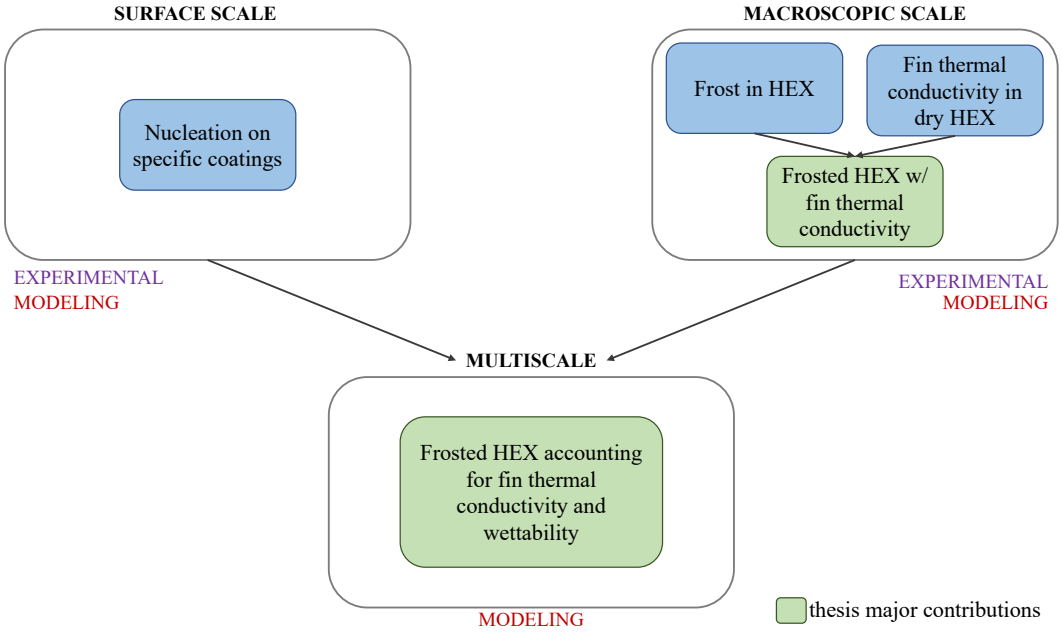

FIGURE 1.15: Thesis Contribution

1.6 Manuscript Overview

This manuscript is organized in six different chapters :

- **Chapter 1 - Introduction :**
  The first chapter, presented here above is an introduction to the problematic tackled in the present thesis. First, it explains the energy context and heat pump technology. Then, in a general way, the frost problematic in refrigeration system is introduced. To decrease this issue, the method investigated is the use of hydrophobic coatings. In this context an introduction to the behaviors and physics of such material is presented. This introduction is concluded with the frosted evaporator characterization in literature, followed by the thesis objectives

- **Chapter 2 - Experimental investigations :**
  The second chapter focuses on the experimental investigations involved in the frame of the present thesis. The main objective is to get a data set and an

understanding of the physical behaviors before writing simulation models. This chapter is split into two main sections. The first one focuses on the study of a highly instrumented heat pump submitted to frost in its evaporator. Innovative techniques are implemented to get a better overview of the frost formation within this device. The second section focuses on more fundamental study of frost accretion on bare and superhydrophobic samples. The data gathered in this chapter allows to feed and validate the simulation models

- **Chapter 3 - Modeling developments :**
  The third chapter presents the different simulation models. As for the previous one, it is split in two sections, dedicated to the modeling of the evaporator and to the surface phenomena, respectively. The evaporator model is an innovative *tube-by-tube* discretization. This configuration allows to manage frost modeling on each tube independently. Furthermore, beside classical considerations, fin thermal conductivity is accounted in this model. Regarding the surface models, it considers basic phenomena of nucleation, allowing to account for the surface contact angle, roughness and tilt. Even if not performed in this chapter, the ultimate goal is to merge both, evaporator and surface, models.

- **Chapter 4 - Experimental validation :**
  The fourth chapter focuses on the tuning of different empirical parameters to validate the simulation results by the means of the experimental data. Once more, this chapter is split into evaporator and surface dimensions. This chapter allows to have a clear overview of the different results and to acknowledge the validity of the different models.

- **Chapter 5 - Multiscale merge :**
  In this fifth chapter, the evaporator and surface models are merged. Here, only numerical simulations are considered. The objective is to quantify the the impact of a hydrophobic coating on the frost deposition in the evaporator and so its performance.

- **Chapter 6 - Conclusions :**
  The last chapters allows to get an overview of the results brought by this thesis and give some perspectives for further works on this topic.

Chapter 2

Experimental Investigations

2.1 Introduction

The experimental investigations contributes to two main aspects. First, they give the opportunity to observe the physical phenomena involved in a given process. This provides the materials mandatory to initiate a good modeling approach. Then, data is recorded throughout the different tests feeding the aforementioned models. Furthermore, the data is mandatory for the validation of the different models.

Section 2.2 is dedicated to conduct a deep study of the evaporator of a heat pump. In a first time, the test rig and the data monitoring setup are presented. The accent is put on innovative systems such as a differential mass measurement system to obtain a very accurate value of the amount of frost present in the system. Furthermore an image treatment is implemented to record the frost thickness in the device. Then, the results recorded in the experimental campaign are detailed and commented.

The next investigation is detailed in Section 2.3. It focuses on the other test bench facility dedicated to the investigation of nucleation on different surfaces showing different hydrophobicity, with static contact angles going from 90° to 162°. First, the setup is described. Then, two different criteria are developed, based on numerical image treatments to obtain a quantitative criterion determining the nucleation phase duration. The testing campaign defined by the study of the different surfaces in different conditions is conducted and commented here.

2.2 Heat pump facility

One of the test-rigs considered in the frame of the thesis is a fully monitored heat pump. This specific heat pump was firstly designed for being an exhaust air heat pump in residential buildings. Suffering from frost formation issues, it revealed to be a good candidate for the present study. This specific machine is conceived to be fed by nominal air flowrate of 200 m^3/h between 15 and 20°C, having a nominal heating capacity of 1500 W and a nominal COP of 3.4.

2.2.1 Test-rig description

This heat pump is however built for the purpose of specifically study frost formation on its evaporator with less concern about the other components performance. It shows a conventional architecture, as seen in Figure 2.1, and works with HFC-R134a (1,1,1,2-Tetrafluoroethane) as working fluid.

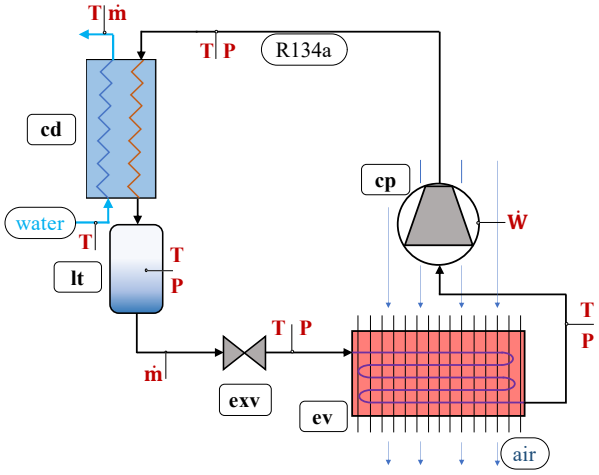

FIGURE 2.1: Architecture of the studied heat pump

The condenser (cd) is a brazed-plate heat exchanger. It is cooled down with tap water with its temperature imposed by the network. Typical steady state temperatures vary between 10 and 18 °C depending on the season. Nevertheless, the water mass flowrate can be tuned. The refrigerant at the exhaust of the condenser is connected to a liquid tank (lt), ensuring the liquid saturated state of the refrigerant at the liquid tank exhaust. The fluid is then expanded in an thermostatic expansion valve (exv). The low pressure refrigerant is then driven to the evaporator (ev). This exchanger has a tubes and fins configuration. A more important focus is dedicated to this componant later on. The refrigerant vapor is finally pressurized by a constant speed rolling piston compressor (cp) of 2300 W to close the loop. The mass of refrigerant in the circuit is about 1.7 kg. This quantity has been chosen with a rule of the thumb and tuned while running for the first time, to obtain a good subcooling level.

TABLE 2.1: Main components and fluids of the test rig.

Component	Type	Model/Brand	Comment
Working fluid	HFC	R134a	n.a.
Heat source fluid	Air	n.a.	T and RH controlled
Heat sink fluid	Water	n.a.	Tap water
Compressor (cp)	Rolling piston	Tecumseh RK5512Y	Constant speed
Condenser (cd)	Brazed Plates	Alpha Laval	n.a.
Liquid tank (lt)	Vertical tank	n.a.	Volume = 0.7L
Expension valve(exv)	Thermostatic	Danfoss	n.a.
Evaporator (ev)	Fins and tubes	EuroCoil	Visual access

As evoked before, the evaporator is a tubes and fins heat exchanger. The tubes show a staggered configuration.

FIGURE 2.2: Pictures of the evaporator

As seen in Figure 2.2, the refrigerant is split in three distinct channels. Those correspond to three vertical zones of the coil. The fluid is evaporated independently in each zone. The superheated vapor of each circuit is then driven to a collector, mixed together and brought back to a single pipe. The pipes are made of copper and the fins of aluminum.

As the ultimate objective is to study frost, the outer metallic casing of the exchanger has been replaced by transparent polymer plates, to have a visual access on the top and bottom tubes (Figure 2.3). The geometrical characteristics of the coil are summarized in Table 2.2.

FIGURE 2.3: Polymer casing of the evaporator

The heat necessary to vaporize the refrigerant is extracted from humid air. The objective is to emulate stale air from building ventilation. To do so, pressurized air at 4.2 bar from a 75 kW air compressor is available at the laboratory. The air is then dried out in a dryer before being expanded. A cooling coil has as objective to cool down and dry the air flux even more. As a result, air at about -5°C and 5% relative humidity is available for a maximum volumetric flowrate of 250 m^3/h. From this point, the mass flowrate, temperature and humidity need to be tuned, to fit the desired conditions.

TABLE 2.2: Geometrical characteristics of the evaporator.

Characteristic	Value	Characteristic	Value
Width	0.28 m	Fin pitch	2 mm
Height	0.31 m	Exchange area (refrigerant side)	0.36 m^2
Depth	0.11 m	Exchange area (air side)	7 m^2
Nbr of rows	12	Distance between tubes (horizontal)	22 mm
Nbr of columns	4	Distance between tubes (vertical)	26 mm
Nbr of fins	140	Tube external diameter	10 mm
Fin thickness	0.2 mm	Tube internal diameter	8.5 mm

To obtain the desired air stream conditions, three different lines are controlled (Figure 2.4):

- the flowrate can be tuned with a by-pass valve. It allows to set a leakage level to reject the unwanted part of the stream to the atmosphere;
- the air temperature, with three electrical resistances : two 1.2 kW constant power, and one adjustable 1.5 kW power, tuned with a PID controller;
- the humidity, by injecting a controlled amount of high pressure steam in the air flow.

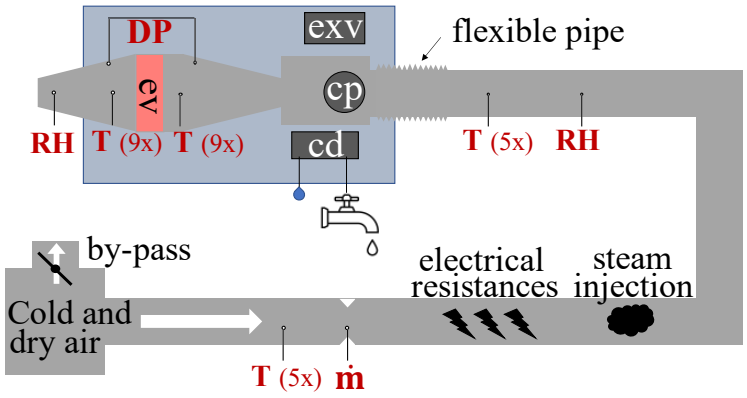

FIGURE 2.4: Set-up scheme of the test bench (top view)

This air flow is then injected to an insulated box containing the compressor to cool it down. It finally goes through a divergent, the evaporator and then a convergent. The divergent and convergent aim at uniforming the flow as much as possible. They are illustrated in Figure 2.5.

2.2.2 Data monitoring

Thermo-hydraulic measurements

As mentioned before, the heat pump is fully instrumented. Figures 2.1 and 2.4 show all measurements key locations respectively on refrigerant and air loops.

For refrigerant pressure, piezoresistive sensors are involved. The mass flowrate of refrigerant and water are measured with a Coriolis flow meter and a scale/chronometer

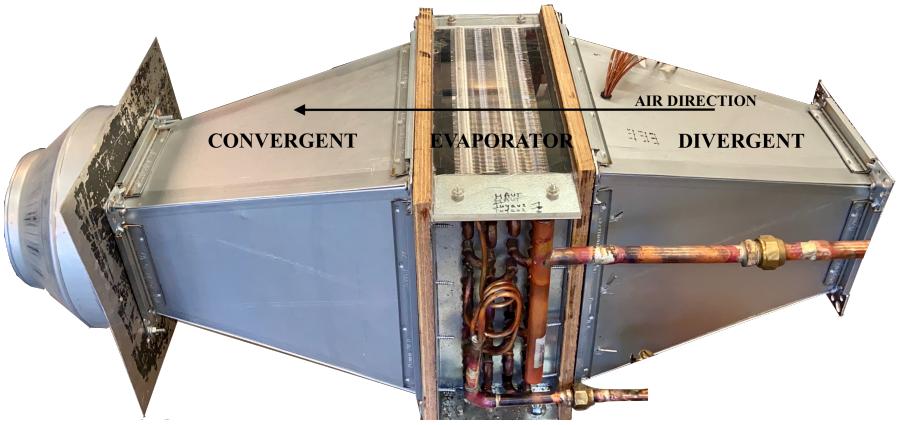

FIGURE 2.5: Picture of divergent and convergent around the evaporator

set, respectively.

All temperatures are measured with T-type thermocouples. In the air stream, the temperatures are measured through grids of thermocouples, as shown in Figure 2.6.

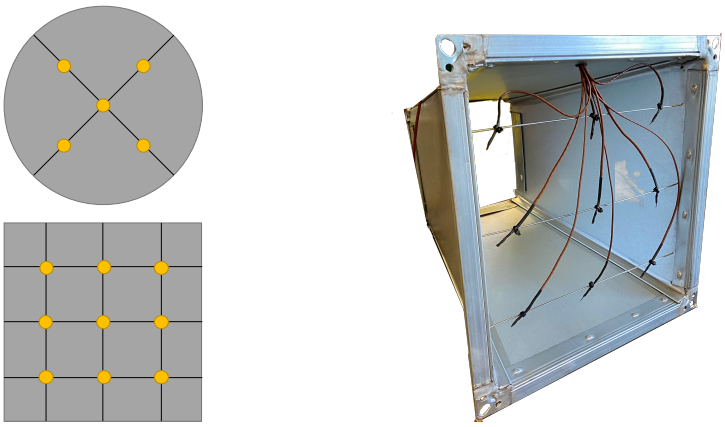

FIGURE 2.6: Position of TC in circular duct (left up), rectangular duct (left down). Picture of actual TC position in a rectangular duct (right)

To measure the air mass flowrate, a differential pressure sensor is implemented at a Trox bounds. However, this system needs a minimum length up and downstream the measurement zone. It implies that the flowrate cannot be measured very close to the heat pump, where the measurement matters. In between, many leakage sources are present (resistances, duct connections, vapor injections,...). The actual air flowrate passing through the heat exchanger is then overestimated. In case of a frosting event, an additional pressure drop is added in the system, increasing the pressure and so the leakages upstream and increasing this unwanted phenomena. A specific calibration of the measured flowrate is conducted, varying artificially the pressure drop at the exhaust of the evaporator with an iris damper, as illustrated in Figure 2.7.

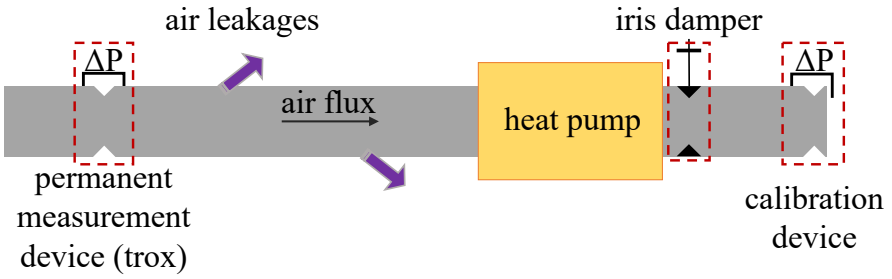

FIGURE 2.7: Air mass flowrate calibration setup

The iris damper emulates the pressure drops due to frost formation in the evaporator. It is assumed that between the heat pump and the calibraton device, the leakages are negligible. From this setup, the following map can be drawn.

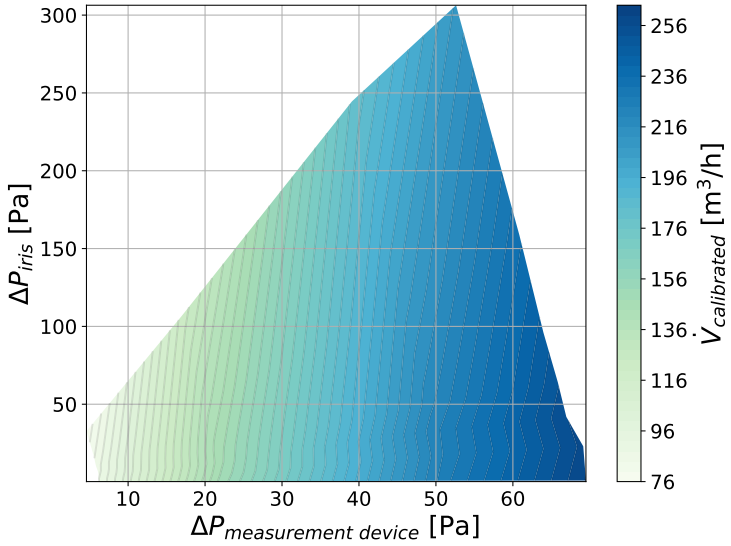

FIGURE 2.8: Air flowrate calibration map

A calibration law is deduced which is function of the differential pressure of measurement device and of evaporator additional pressure drop due to frost, to account for leakages:

$$\dot{V}_{\text{HEX}} = 42.4915 + 5.4 \cdot \Delta P_{\text{trox}} - 0.0712 \cdot \Delta P_{\text{iris}} - 0.0353 \cdot \Delta P_{\text{trox}}^2 + 0.00012 \cdot \Delta P_{\text{trox}}^3 \quad (2.1)$$

with ΔP_{trox} being the differential pressure of measurement device. It is to note that this law is valid for flowrates between 75 and 260 m^3/h.

To study air distribution, air speed velocity is recorded with a hot-wire anemometer Testo 405i. It is worth noting that these measures are qualitative because of the poor accuracy of the anemometer and more importantly because of the measurement instability. A slight move of the sensor position can induce important differences. However the measurements were repeated to increase accuracy.

Humidities are measured using capacitive-type humidity sensors. Only one up and one downstream the heat pump are installed. Their positions are specifically chosen

ensuring a good mixing of the air stream to measure representative data. Because they represent a key element in the experimental investigations, specific calibration steps are detailed here. First, the relative humidity is corrected regarding reference atmospheric conditions, controlled with saturated aqueous solutions of inorganic salts. Then, because of an absolute humidity deviation with temperature change, measurements are also corrected regarding this point.

Humidity sensors are successively immersed in different sealed bottles. In each bottle lies a different wetted salt or pure water, setting a known theoretical relative humidity, based on Raoult's law. The solutions used are $KOH_{(aq)}$, $MgCl_{2(aq)}$, $NaCl_{(aq)}$ and pure water, showing at 23°C and equilibrium, humidities of 8, 33, 75 and 100%, respectively. Figure 2.9 (left) shows the measured relative humidity values before and after the calibration. The maximal error of 5% is reduced to less then 2%, accuracy of the sensor, at 23°C.

An additional deviation is noticed. The relative humidity sensors are installed in an air flux showing a constant absolute humidity. Without injecting humidity, the air temperature is artificially increased, thanks to the electrical resistances. The absolute humidity computed based on the relative humidity and temperature measurements is increasing as well, where it should not be. To fix it, a constant absolute humidity is set and the temperature is tuned to different values between 5 and 35°C. The data at 23°C is considered as reliable and a calibration law is deduced. The 23°C temperature is chosen because it is the temperature used for the previous calibration step and it is close to the nominal temperature of the humidity sensor. The results are shown in Figure 2.9 (right).

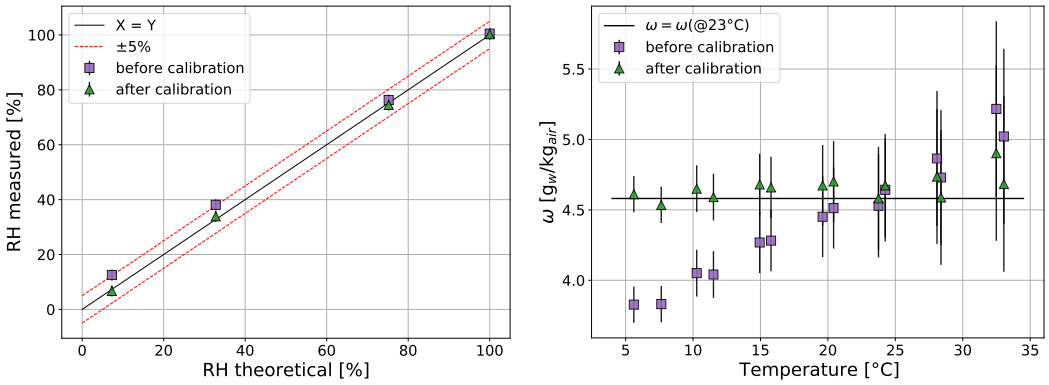

FIGURE 2.9: RH calibration - use of moistened salts (left) and absolute humidity calibration regarding temperature (right)

The calibration law is expressed as:

$$\omega_{\text{corrected}} = p_0 + p_1 \cdot T_{\text{reference}} + p_2 \cdot T^2_{\text{reference}} \tag{2.2}$$

with p_0, p_1 and p_2 being calibration coefficients and p_0 is computed as:

$$p_0 = \omega\Big|_{RH_{\text{meas}}} - p_1 \cdot T_{\text{meas}} - p_2 \cdot T^2_{\text{meas}} \tag{2.3}$$

Ultimately, the relative humidity corrected is:

$$RH_{\text{corrected}} = 1.063 \cdot RH\Big|_{\omega_{\text{corrected}}} - 0.0659 \tag{2.4}$$

Finally, the list of involved sensors in thermo-hydraulic measurements is detailed in Table 2.3.

TABLE 2.3: List of sensors

	Measure	Brand/type	Range	Total error
Air	T [°C]	T type thermocouple	-270 to 370°C	0.5K
	RH [%]	S+S Regeltechnik KFTF-20-U	0-100%	2%
	$\dot{m}$ [kg/s]	Trox + Sensirion SDP1000L05	0-0.15kg/s	5% m.v
	u [m/s]	Testo 405i	0-30 m/s	3% m.v.
Ref	T [°C]	T type thermocouple	-270 to 370°C	0.5K
	P [bar]	General Electric Druk	0-6 bar	0.5% m.v.
	P [bar]	General Electric Druk	0-16 bar	0.5% m.v.
	$\dot{m}$ [kg/s]	Krohne Optimass3300c	0-0.125kg/s	0.1% m.v.
	$\dot{W}_{cp}$ [W]	Extech 382100	0-1200 A	1% m.v. +0.08kW
	m.v. :	measured value		

Mass measurement

As frost is the heart of the research, measuring its mass is a key element. The first method, frequently met, is to express a mass and energy balance on the air side of the evaporator. Knowing mass flowrate, humidities and temperatures at the supply and exhaust of the evaporator, the frost and condensates mass can be deduced.

$$m_{\text{water,t}} = \int_0^t \dot{M}_{\text{air}} \cdot (\omega_{\text{su}} - \omega_{\text{ex}}) dt \tag{2.5}$$

The most natural method is to directly measure the mass, through a balance or load cell setup. Intuitively, the evaporator should be weighted on its own. However, this technique is not adopted here, because if frost accrates on the exchanger, the refrigerant condition is going to change. The actual refrigerant mass within the device may then vary, introducing confusion in frost mass measurement. For this reason, the whole set-up is weighted, as the quantity of refrigerant is constant.

The heat pump is mounted on a metallic frame and the air connection is made of a flexible aluminum pipe allowing the lowest possible mechanical resistance. The frame is weighted by the mean of a load cell, as shown in Figure 2.10.

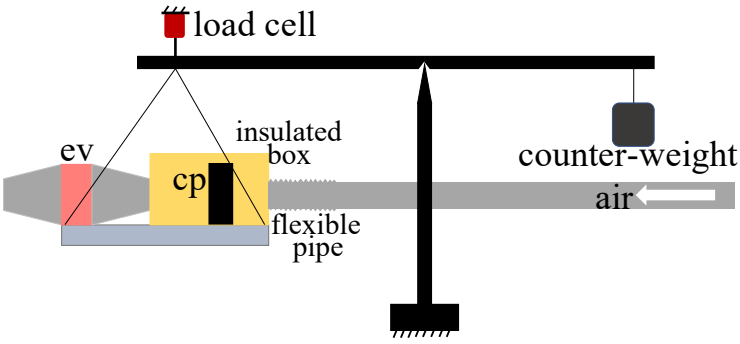

FIGURE 2.10: Differential mass scale setup

Here, a trick is used to unload the sensor. Indeed, the whole test bench set up is around 65 kg. However, the frost quantity weighted is around maximum 1.5 kg. The accuracy of a sensor of a maximum capacity above 65 kg would not be satisfying to measure precise variations under 1 kg. As a consequence, the frame is fixed to a beam, supporting a counter-weight on its opposite side, as shown in Figure 2.10 and 2.11.

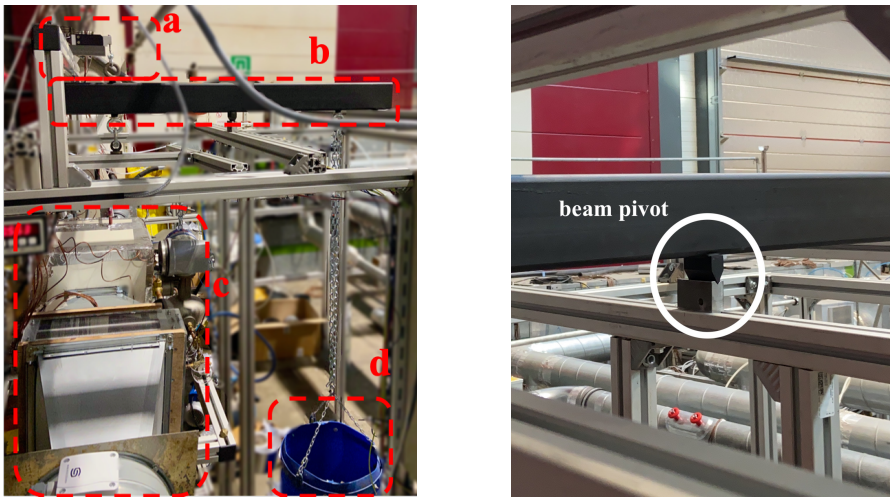

FIGURE 2.11: Pictures of the test bench : (a) load cell - (b) beam - (c) heat pump - (d) counter wight

The beam lies on a vertical structure with a mechanical interaction as small as possible. The load cell, firmly clamped, is then connected to the beam (on the HP side). In this way, the sensor range can be much smaller, as the installation weight is counterbalanced. In other words, the sensor does not measure the absolute mass anymore, but only the mass variations. Here, a 2-kg load cell is chosen, affording a 1-g precision.

For two reasons, the load cell is calibrated before each test :

- because an offset may be observed (not exactly at 0 g at the start of the test) and this offset can be different for each test, due to external factors.
- the two incoming secondary fluids (water at condenser and air at the evaporator) impose a force on the structure. This force depends on the involved flowrates and may have a vertical component, directly impacting the load cell.

The procedure is to get the complete setup in steady state, with the compressor off (to avoid any condensation or frost events). Then the the evaporator is loaded with different calibrated weights of 50, 200, 500, 1000 and 1500 g. Then, a classical calibration law is fitted and implemented in the data post treatment. Finally, the calibration weights are removed, the compressor is turned on and the test begins. A typical calibration is illustrated in Figure 2.12.

For this specific calibration, the fitting law is expressed as :

$$m_{\text{calibrated}} = -30.23 + 1.03 \cdot m_{\text{measured}} - 1.98 \cdot 10^{-5} \cdot m^2_{\text{measured}} \tag{2.6}$$

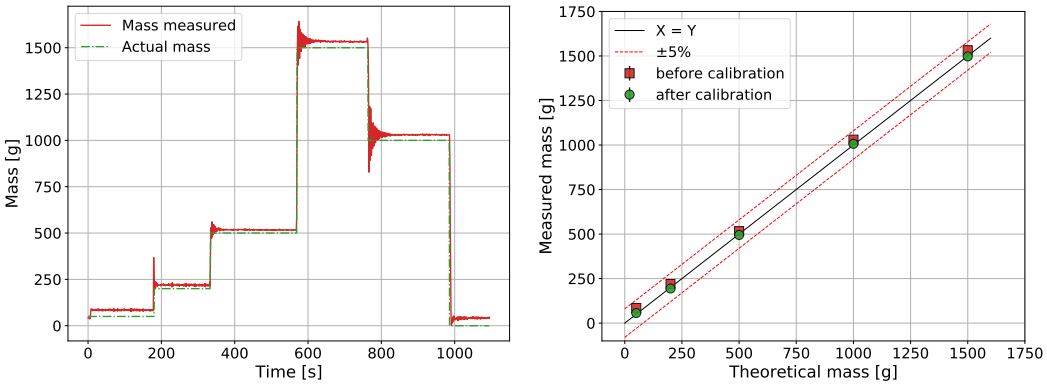

FIGURE 2.12: Load cell calibration

Optical measurement

As previously said, the refrigerant is split in three channels. In theory, the mass flowrate should be split evenly in those circuits. However, for different reasons such as manufacturing defaults, oil retention, etc. there can be a refrigerant misdistribution. A technique to quantify it would be to install three mass flowmeters, one for each channel. However, it would disturb the cycle, add pressure drops and would be expensive. Satisfying results are achieved using an infra-red camera FLIR E50. The temperature distribution of the end-tips of the tubes into which flows the working fluid can be captured. It allows to distinguish the superheated zone form the two-phase zone. Considering the airflow evenly distributed, a large superheat zone is translated by a lower refrigerant flowrate.

Regarding the frost distribution in the exchanger, as evaporator casing is partially replaced by polymer plates, visual access is available at the top and bottom of the device. To record the visual evolution, a GoPro Hero 5 Black camera is installed to take snapshots every 30 seconds in 4000x3000 resolution in a linear way. A ruler is in the frame to have a reference for the frost layer thickness.

2.2.3 Preliminary tests

Air flow distribution

An important preliminary measure is the air flow-rate distribution at supply and exhaust of the evaporator in dry condition. Nine air speed measurement points are considered, corresponding to the thermocouple positions (see Figure 2.6).

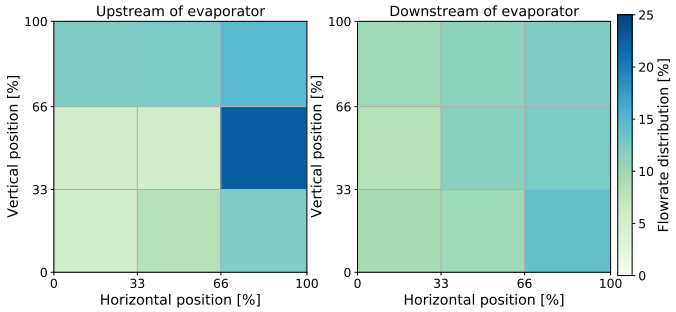

FIGURE 2.13: Air flowrate distribution map

Those maps allow to perform weighted average for temperature up and downstream the exchanger. It is noticed that the evaporator tends to smooth the air distribution.

The same exercise is conduced in frost conditions. The objective is to check how the frost blockage affects the airflow distribution. Again, the ultimate objective is to derive some trends and not quantitative results. As frost growth uniformly on the exchanger width, the speeds are averaged on the width. Only the impact on the vertical dimension is shown here.

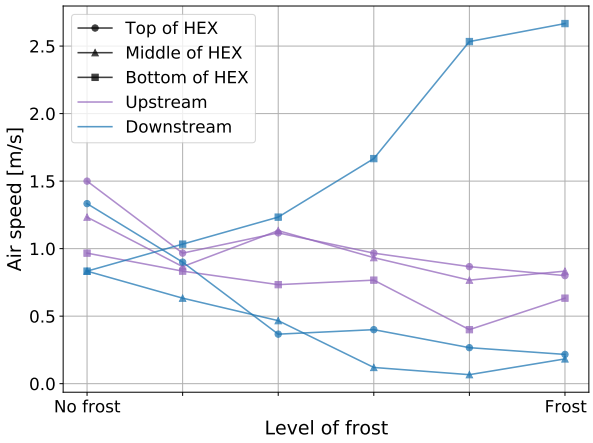

FIGURE 2.14: Air speed regarding the position and frost conditions

As seen and explained later in the thesis, the frost does not form uniformly on the height and depth of the exchanger. Basically, the air enters the evaporator evenly on the height, whatever the conditions. It underlines that the frost is principally present at the back of the exchanger (it will be visually validated later). Furthermore, the downstream speed at the bottom of the exchanger clearly increases. This observation indicates that frost forms principally on the upper part of the evaporator. The key idea here is to show that even if frost accrates at the back of the exchanger, it does not substantially impact the upstream flowrate.

Refrigerant distribution

As mentioned earlier, refrigerant may not be well distributed through the different channels. It impacts the superheat proportion of the refrigerant in each circuit and so, the frost growth for each portion of the exchanger.

Infrared pictures are shot at the first moments of a given test (i.e. when there is no frost yet) and at the end of the test (i.e. when an important part of the exchanger is frosted).

From Figure 2.15, 6 and 8 superheated tubes are counted for the top and bottom part of the exchanger, respectively. This effect is even more accented while the evaporator is frosted with a total of 2 tubes superheated and 12 for the bottom part.

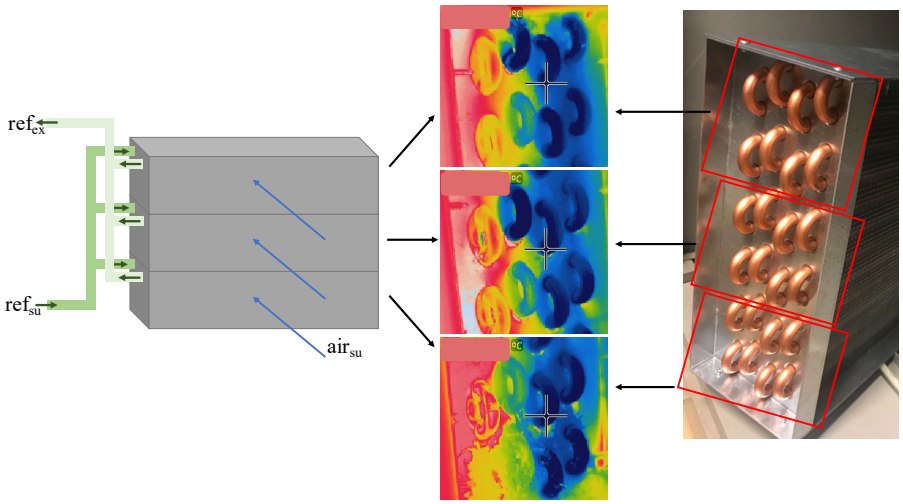

FIGURE 2.15: IR pictures of the dry evaporator

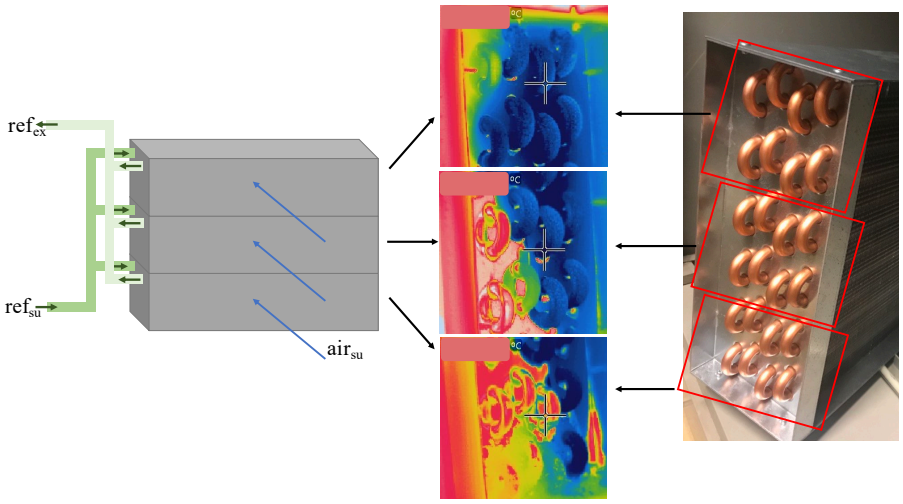

FIGURE 2.16: IR pictures of the frosted evaporator

For some reasons, such as uneven pressure drops due to manufacturing defaults, the refrigerant mass flowrate is smaller for the bottom part compared to the top of the exchanger. As the two-phase zone is larger at the top, frost conditions are more easily met. When frost grows, the upper air flowrate is deviated to the bottom part of the exchanger, because of the cross section decrease due to frost. On the air side, the heat exchange is then enhanced at the bottom part and deteriorated at the upper part. A snowball effect takes place, increasing the superheated zone at the bottom of the evaporator. This explains the results shown Figure 2.16.

2.2.4 Experimental campaign tests

Once the sensor calibrated and preliminary tests carried-out and analyzed, an experimental campaign is conducted to learn about heat pump performance and investigate frost development in the evaporator. As the compressor speed is constant, only secondary fluids conditions can be adjusted.

Heat pump condensers are important devices as they are the component exchanging the useful heat for a heating system. However, it is not the focus of the present

study, so any extensive study is dedicated to this component. The same flowrate and temperature are kept, to keep this part of the cycle in the same condition and to avoid adding an additional freedom variable to the system. The expansion valve as well is tuned once before the tests and stays in the same configuration for the complete investigation.

Having constant speed for the compressor and condenser inputs allows to isolate the evaporator behavior impact on the cycle.

The tests are separated in two main categories, namely dry and wet/frost conditions tests. The first category corresponds to tests where the air supply conditions are such that no condensation or frost event occurs. The system is then in perfect steady-state conditions so the data can be time-averaged and balances can be successfully conducted. Contrarily, even if supply conditions are kept constant, if frost accumulates in the exchanger, working conditions are slowly but surely evolving, impacting the complete cycle. Those conditions are defined as quasi-steady-state and temporal evolution is studied.

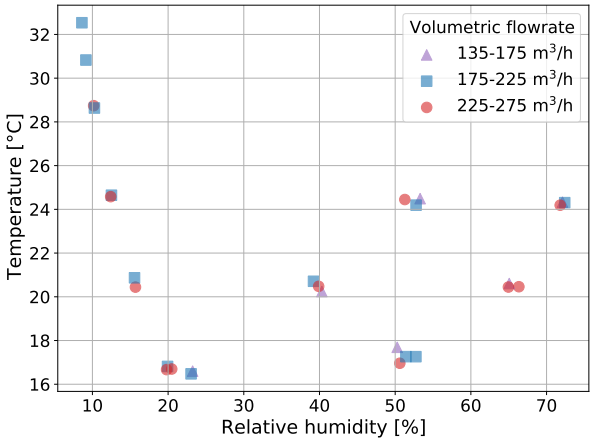

FIGURE 2.17: Visualization of the air supply conditions covered by the experimental campaign.

Figure 2.17 shows the air conditions feeding the evaporator. Those are typical values found in mini exhaust air heat pumps.

Dry conditions

As previously said, dry tests are steady-state, allowing to average the data. Here, a minimum of 10-minute for the test window in stabilized conditions is taken for each test.

First the thermal power balance on the condenser can be plotted (see Figure 2.18), with measured heat transfer rate on the water and refrigerant sides, respectively.

Globally, the measured heat transfer rate difference is under 3%, which is within the measurement device uncertainty. The uncertainty on the water side is very important. It is explained because the imposed mass flowrate is consequent, leading to a small temperature difference. The uncertainty on this ΔT is then high. To decrease this phenomenon, the mass flowrate should be increased. However, in the present

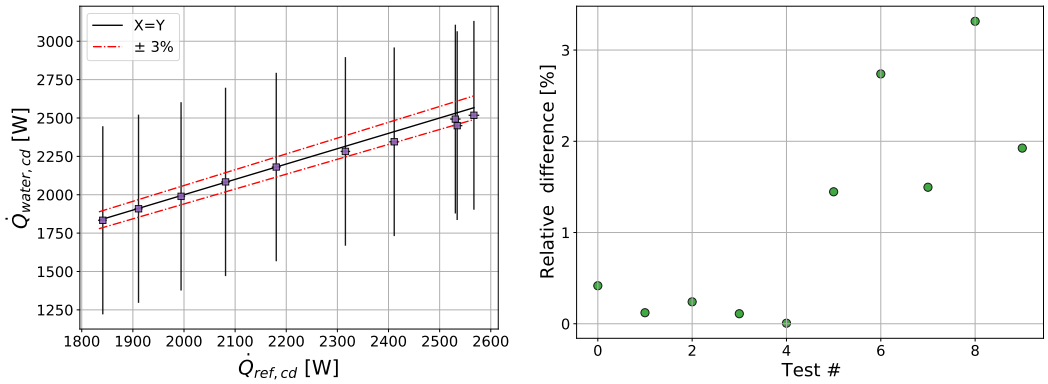

FIGURE 2.18: Heat transfer rate balance on the condenser

context, the results are considered satisfying.

The same exercise is conducted for the evaporator. An additional focus is set to increase the measurements quality. On the air side, the heat transfer rate is computed in four different ways:

1. Temperatures at the bounds of the exchanger is an arithmetic average of the 9 temperatures, up and downstream;
2. Temperatures at the bounds are computed with a weighted average, based on the air speed measurements, up and downstream;
3. Temperatures at the bounds are computed with a weighted average, based on the upstream airspeed only, for the up and downstream temperatures;
4. Temperatures at the bounds are computed with a weighted average, based on the downstream airspeed only, for the up and downstream temperatures.

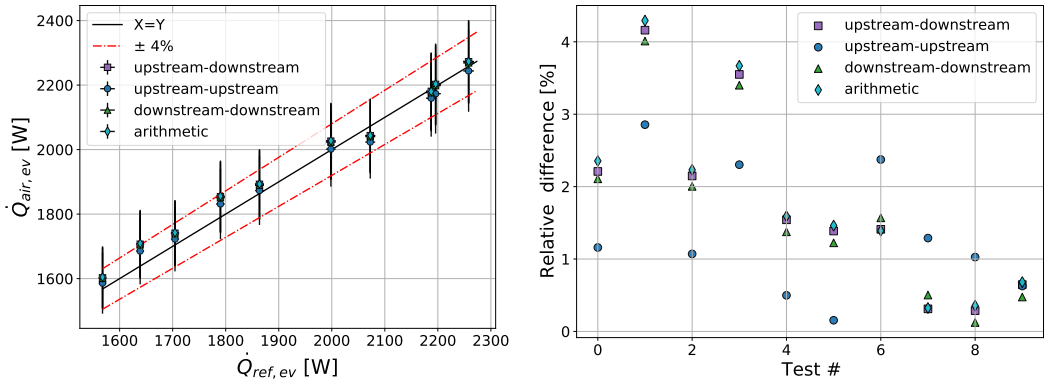

FIGURE 2.19: Heat transfer rate balance on the evaporator

Hopefully, the 4 ways of computation show similar results with an average deviation of 1.65%, which is very satisfying, especially for a balance with a air flux. The best measurements are for the "upstream-upstream" temperature average with a maximum and average deviation of 4.1 and 1.3%, respectively. This averaging technique is then considered.

This being checked, the test-bench measurement can be considered as reliable.

Wet/frost conditions

First, it is worth saying that no direct measurement system on the test bench can distinguish the liquid condensates from frost deposition. However, indirect clues can help to spot a frosting event.

In a first step, four representative tests are highlighted to study the evolution of relevant quantities. The operating conditions of those tests are described in Table 2.4.

TABLE 2.4: Air operating conditions for the different representative tests

Test	$T_{\text{air,su}}$ [°C]	ω_{su} [g_{water}/kg_{air}]	$\dot{M}_{\text{air}}$ [m^3/h]
Red	24	14	230
Blue	24	10	200
Purple	24	10	150
Green	16	6	230

The time evolution of the mass accumulation within the heat exchanger, pressure drops and heat transfer rate on the air side are illustrated in Figures 2.20, 2.21 and 2.22, respectively. From there, different conclusions can be drawn.

First, the mass accumulation in the evaporator is shown in Figure 2.20, regarding either the force sensor or humidity balance. The mass accumulation is either liquid condensates, frost accumulation or a combination of both. The ascending part of the curve corresponds to normal operation of the heat pump. At the maximum of the curves, the compressor of the heat pump is shut down but the air flux is still imposed. It leads to a defrost phase in the evaporator. A part of the water is collected in a bucket through a drain at the bottom of the exchanger. This amount of water is weighted with the complete set up, so it does not imply any variation in any measurement technique. The mass decrease is due to water carried away by the air stream or evaporated in the flux.

Then the pressure drops are displayed in Figure 2.21. It is a good indicator to deduce the frost proportion compared to liquid condensates. An increase of pressure drops followed by a plateau corresponds to a majority of liquid condensates in the evaporator (Red) while a constant ΔP increase indicates frost accumulation (Green). Obviously, a hybrid situation can be met (Purple).

Finally, the measured heat transfer rate is displayed in Figure 2.22, regarding either the refrigerant side, or the air side using two different methods to compute the latent load. First, the condensed water is computed using Eq.(2.5) based on humidity balance. The second method is the integration of load cell measurement.

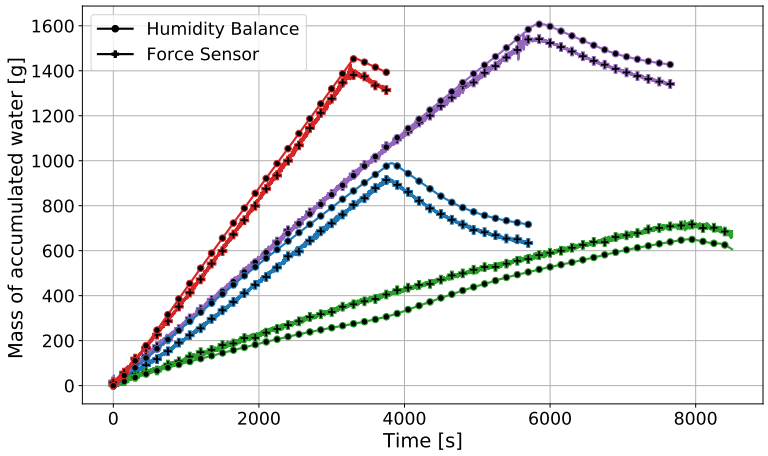

FIGURE 2.20: Time evolution of the accumulated mass evolution in the evaporator

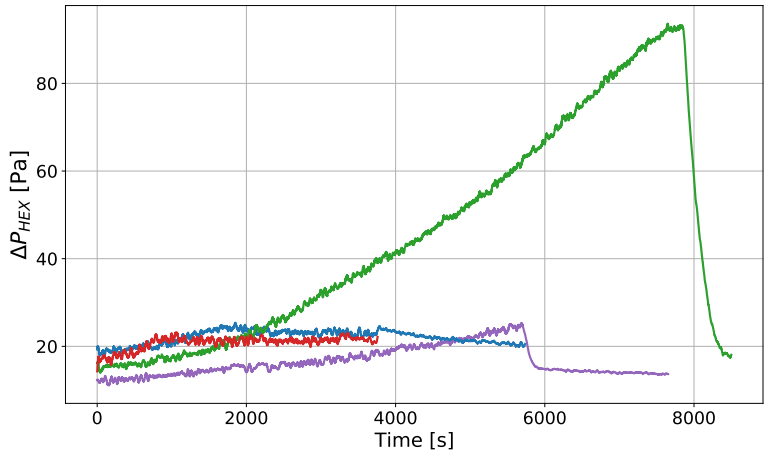

FIGURE 2.21: Time evolution of the air pressure drop evolution of evaporator

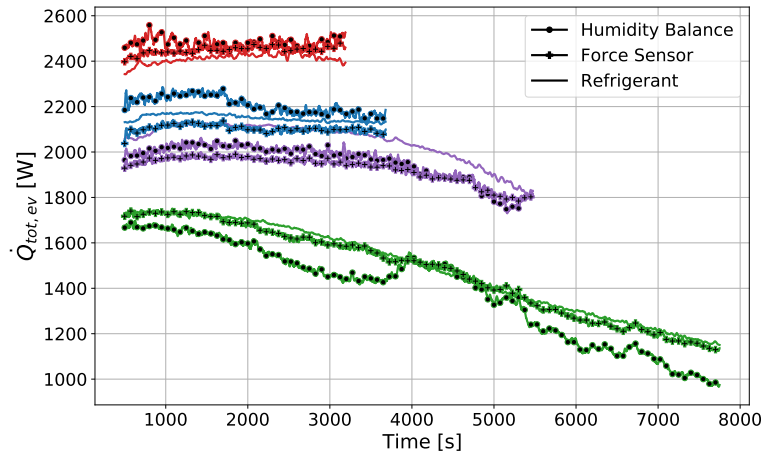

FIGURE 2.22: Time evolution of the heat transfer rate evolution of evaporator

The refrigerant side is taken as the reference, because the sensors involved are much more accurate compared to the sensors involved on the air side, as seen Figure 2.19. Only the quasi-steady-state portions of the curves are represented, for clarity reasons.

Despite a slight accuracy advantage for the load cell use, both techniques show advantages and drawbacks. First, the pros for the use of humidity sensors (method a) are exposed:

- Setup simplicity : it is intuitive and no complicated mechanical setup is needed. For the mass measurement using the load cell, the test bench has to be hanged, with a counterweight system. Moreover, the measurement of the air mass flowrate as well as the supply humidity is compulsory anyway;
- No external perturbation can occur, unlike the weighting system which can significantly deviates if anything touches it or if the setup is exposed to vibrations.

The advantages of the load cell (method b) are:

- Stability : looking at Figure 2.22, the measured power is more stable with load cell, due to the independence of the air flow conditions for the latent load computation;
- Measurement error : with humidity balance, a mass increment is measured at each time step with its associated error. On a two hours test, all these errors may be added, resulting in a global error relatively important. On the other side, the total mass is recorded at each time step. The error is in this case not cumulative;
- Accuracy : besides the error propagation, the amount of water measured relies on either three sensors (2 RH and mass flowrate) for humidity balance and only one for the load cell method. The global accuracy is then better for the load sensor cell.

To sum-up, the load cell method is more complex to implement but shows better accuracy compared to the humidity balance. In order to illustrate that, the Green test is taken on its own and associated uncertainty is analyzed. First, the water mass accumulation is studied. As evoked before, it can be liquid condensates, frost accretion or both. In the case of liquid water, it rolls along fins by gravitational effect. It is then driven to a bucket by means of a drain. Everything is weighted.

The most striking information in Figure 2.23 is the dramatic impact of uncertainty accumulation implied by the humidity balance technique. For this specific test, after 2 hours time, a 35% deviation is observed, only staying in sensors deviation range. For each time step, the uncertainty is relatively small implying that the measured power is not that much impacted, as explained after. However, if the goal is to measure the total mass in the exchanger, the method a can present major issues. On the other side, the mass measured with the load cells does not show any error in Figure 2.23. The accurate 2 kg-sensor shows a 1 g precision, so the uncertainty is not visible. However, the measures do not show a perfectly smooth line. The whole heat pump is weighted and vibrations are induced by the compressor. Yet, those are very limited and does not impact the results.

Figure 2.24 shows the total powers for the Green test, measured by means of the different techniques with their associated errors.

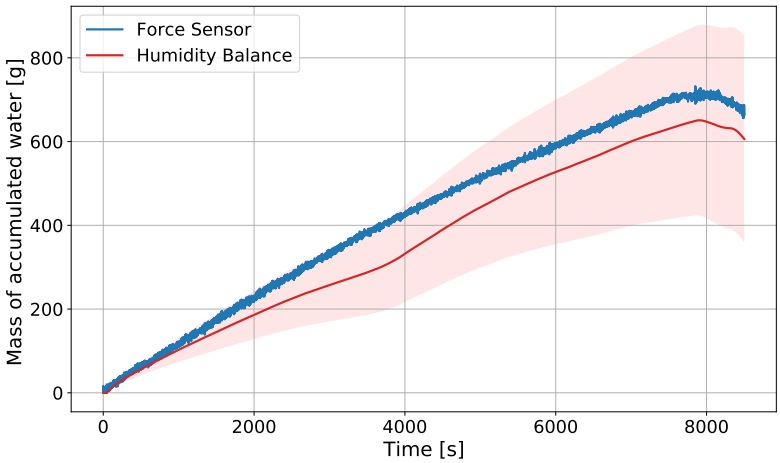

FIGURE 2.23: Mass accumulation through time with the uncertainty accumulation

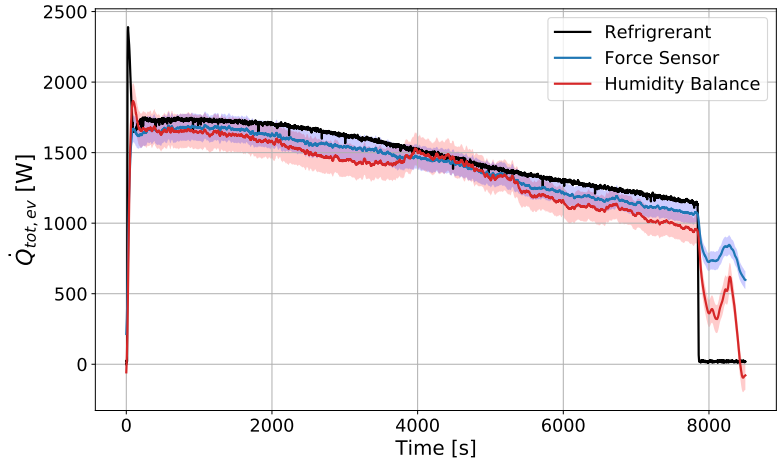

FIGURE 2.24: Total power measured with different techniques and associated uncertainties

As previously said, the refrigerant power is taken as the reference. Even if the error is larger for the humidity balance compared to the load cell method, it is still acceptable. To sum up, if the goal is to predict only powers involved in the evaporator, the load cell is not a major ad-on, even if it is slightly more accurate. Nevertheless, if the objective is to characterize the amount of condensates or frost deposition in the exchanger, the load cell is a real improvement. The set-up being installed and more accurate, the load cell method is the one chosen as the reference for the rest of this work.

As previously seen, frost can deteriorate the performance of the evaporator, and thus, of the heat pump. Different quantities are plotted, regarding the total mass of water accumulated in the evaporator in the following figures. The objective is to obtain indirect clues to determine if the water condensates are in liquid form (*wet*) or frosted (*frost*). Those appellations are set to characterize the main trends, but it should not be forgotten that intermediate situations can be found.

Figure 2.25 reveals two different trends. The first trajectory is that the performance indicators stay quasi-constant with the mass of water in the exchanger (*wet*).

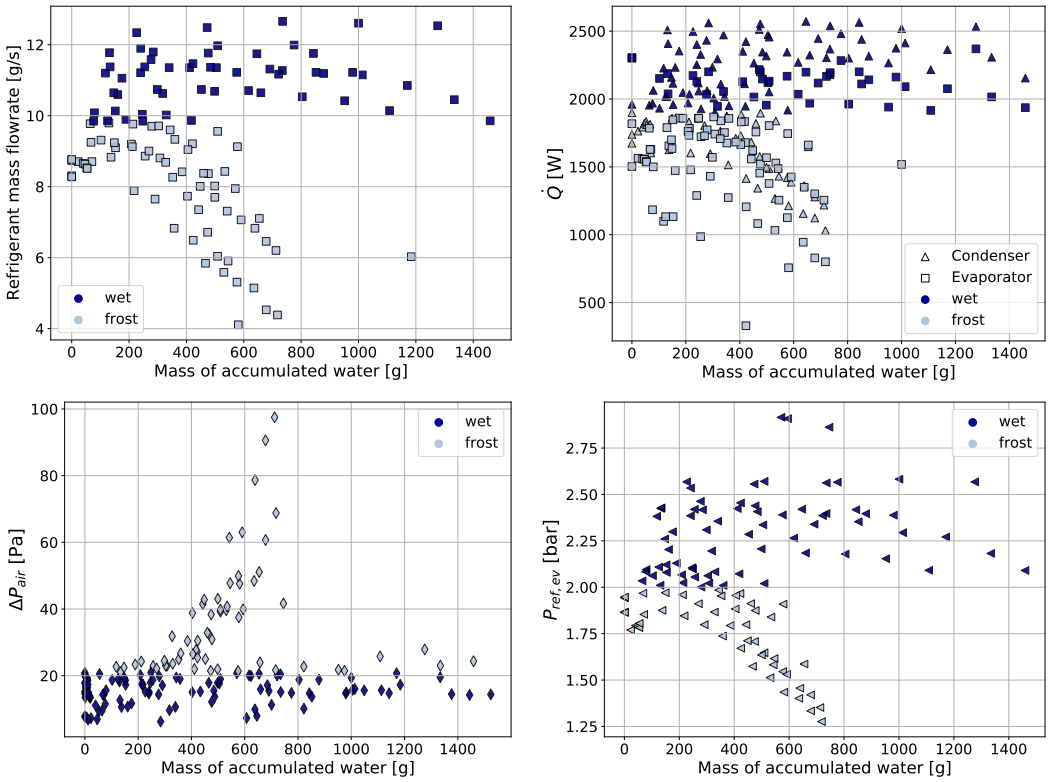

FIGURE 2.25: Refrigerant mass flowrate, heat power transfered in the exchangers, pressure drop on the air side and refrigerant pressure in the evaporator regarding the accumulated mass of water in the evaporator

It suggests the majority of this water is in liquid form. Liquid deposit on the tubes and fins surface and rolls to a liquid receiver at the bottom of the exchanger. Once the conditions are established, the system is steady state and the heat exchange is not deteriorated with time.

On the other hand some test points show a different trajectory as far as mass accumulates. Frost accumulation deteriorates the heat mass transfer because of two main mechanism. First the air cross-section decreases, increasing pressure drops (Figure 2.25 bottom left), and decreasing the air mass flowrate. Secondly, it adds a thermal resistance, decreasing the heat transfer between the air and the refrigerant. As the heat transfer power rate deteriorates, the evaporating pressure decreases (Figure 2.25 bottom right). As a direct consequence, the refrigerant density decreases, implying a decrease in the compressor internal flowrate. It induces a drop of refrigerant mass flowrate in the cycle (Figure 2.25 top left) leading to a heat transfer rate reduction. It is to underline that this trend is not linear. As all phenomena are feeding each other, a snowball effect is observed.

The different figures suggest that more water can be accumulated in the *wet* situation compared to frost. It is explained because, first, tests can be longer, as there is no frost to deteriorate the machine performance. Then, beside time and as illustrated Figure 2.20, the rate of water condensation can be higher than for frost deposition. It corresponds to higher air mass flowrate, leading to higher contact surface temperature. The combination of high air flowrate an higher surface temperatures leads to high condensation rates without frost event.

Next, the results recorded by the camera are presented. It shots a frame every 30 seconds during the complete test. A ruler is installed next to the evaporator to get a reference and measure the frost thickness. Obviously, only the top of the tubes are available for this visual analysis. A camera is not installed at the bottom of the exchanger. The main reason is that frost has never been observed in this region of the device. It is explained because of the refrigerant distribution, as illustrated Figure 2.16.

From the four representative tests picked previously, extremes tests (i.e. completely wet and frosted) are chosen to show the visual results (Figure 2.26).

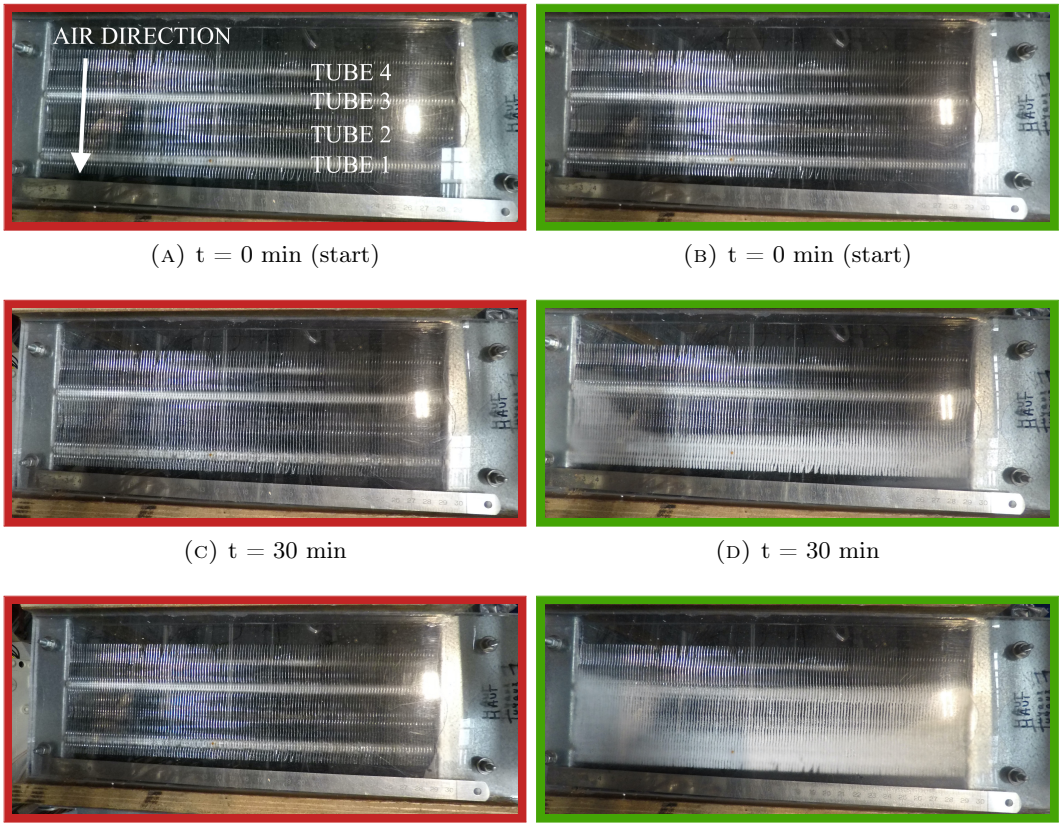

(A) t = 0 min (start) (B) t = 0 min (start)

(C) t = 30 min (D) t = 30 min

(E) t = 60 min (F) t = 60 min

FIGURE 2.26: Frost visualisation for Red test (left) and Green test (right) through time

Even if the Red test in Figure 2.26 shows a much higher accumulation rate compared to the Green one (see Figure 2.20), Figure 2.26 reveals no frost accretion, while the Red does. From those simple observations, combined to the air pressure drops analysis, it is easier to deduce if it is liquid water or frost. Unfortunately, it does not allow to assert precisely the amount of each phase. This proportion depends on the surface temperature, highly correlated with supply air temperature and flowrate.

Another fundamental result is illustrated here and representative for all the frosting events is the way frost accrates. Intuitively, it could be thought frost would start to grow at the air supply of the exchanger. Indeed, the humidity content is heavier at the supply, and the refrigerant is at evaporating temperature (two-phase state)

and not superheated. However, the frost is always observed on the tube the closest to the air exhaust at first and it goes back up to the air supply through time. This phenomenon will be explained by means of the model detailed in the next chapter.

Then, the frost thickness is evaluated for the four top tubes with the software *ImageJ*. Here, the ultimate goal is to measure the average frost thickness for a given tube. To do so, a procedure is put in place to get that measurement with the software. The different steps are illustrated Figures 2.27 and 2.28.

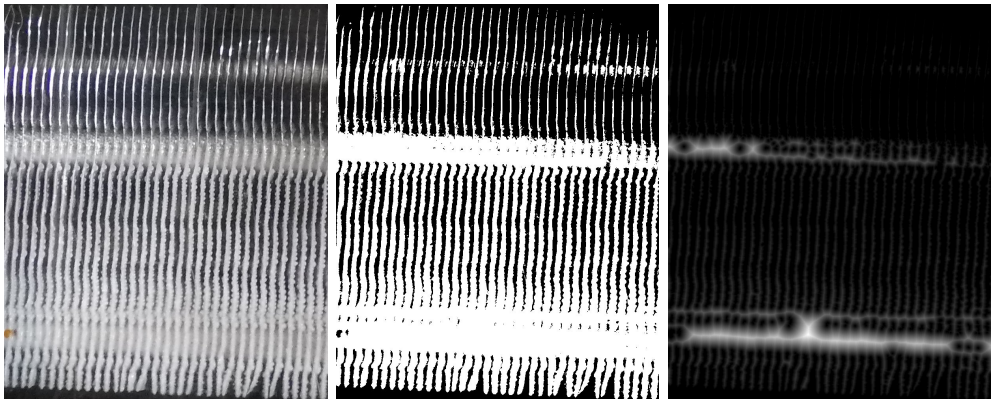

FIGURE 2.27: Visualization of *ImageJ* tool - left : original image sample - center : 8-bit binary image - right : distance map of the image

The very first step is to set the scale, thanks to the ruler graduation and its corresponding pixel number. Then, the original picture is converted to a 8-bit binary pictures, based on a given threshold level, automatically set by the software. It results in a true black and white picture. From this picture a distance map is generated. It does replace each pixel with a grey value, corresponding to the Euclidian distance from the nearest black pixel. In this way, the pixel in the middle of each (frosted) fin has a local maximum value corresponding to half of the total frosted fin thickness and thus to the frost thickness (neglecting the aluminum thickness). From there, with some specific manipulations, those middle pixels are isolated and analyzed.

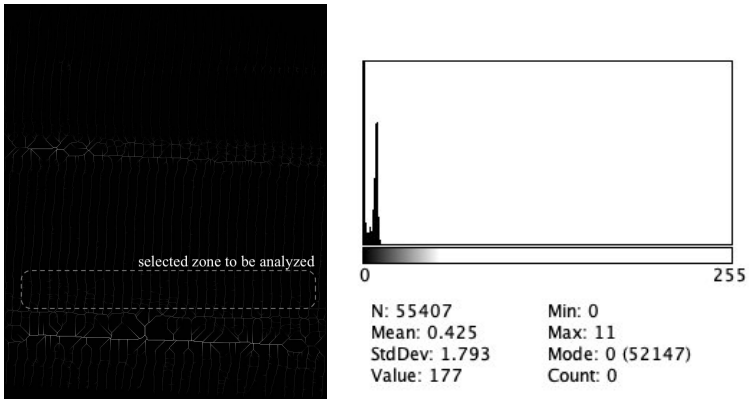

FIGURE 2.28: Visualization of *ImageJ* tool - left : middle pixels representing the maximum value - right : histogram of gray value of the selected zone

From the recurrence and value of each of those pixels and from the distance/pixel ratio, the average thickness of a selected area is deduced.

For clarity reasons, the measured thickness of only one test is represented in Figure 2.29. Numerical values of the complete dataset can be found in Appendix A.

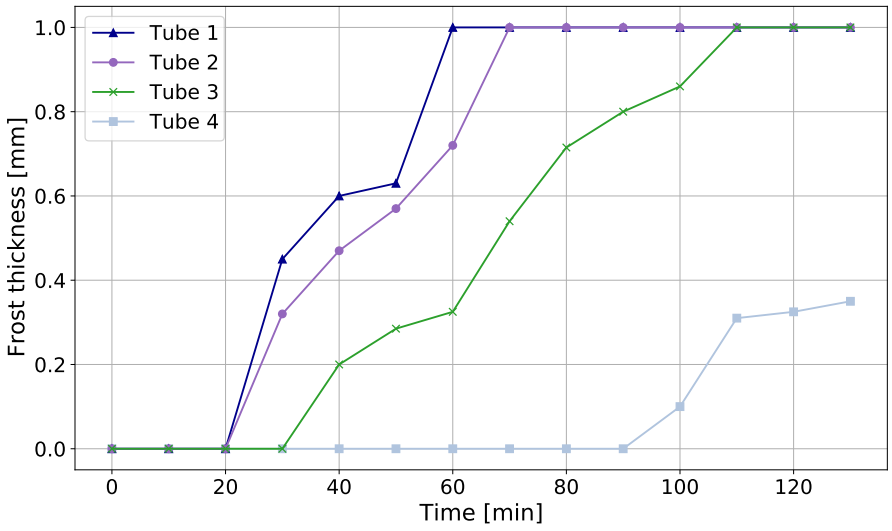

FIGURE 2.29: Experimental frost thickness through time on the different tubes at the top of the evaporator (see Figure 2.26 for the nomenclature of the tubes).

The frost appearance order (from *Tube 1* to *4*, see Figure 2.26 for the nomenclature) is underlined here with a 80 minutes delay between the frost deposition on first and last tube. A saturation is observed for three tubes at 1 mm. It corresponds to a visual frost blockage.

The information extracted from these observations are exploited in the model validation, Chapter 4.

2.3 Surface facility

To get one step further in the frost deposition analysis, a second test bench is built. This particular setup allows the study of frost on very simple surfaces (i.e. flat horizontal plates). The objective here is to test plates with different wettabilities in controlled environment.

2.3.1 Test-rig description

The test-rig consists in a Plexiglas box with controlled environment and a thermoelectric cell based on Peltier effect to cool the sample down.

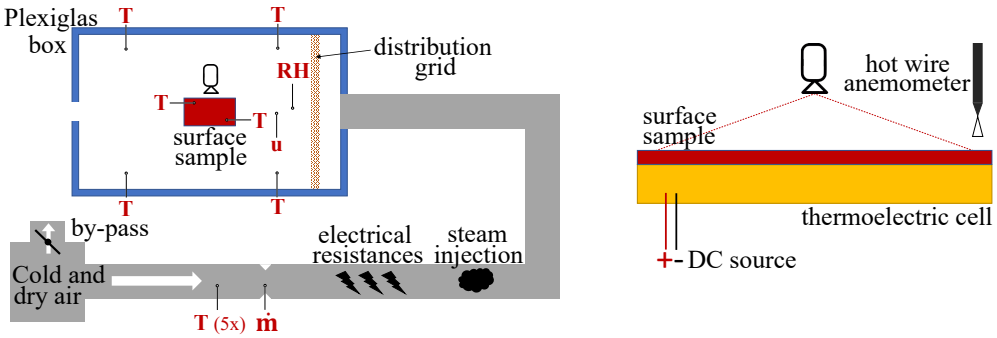

FIGURE 2.30: Set-up scheme of the surface test bench

The air supply is from the same source as the heat-pump test-rig. The air temperature and humidity are controlled in the same way. Here, the mass flowrate is not very important. What is relevant to control and measure is the air speed on the plate. To do so, a distribution grid is installed to uniform the air flux. Imposing a more or less important flowrate directly impacts the air speed.

FIGURE 2.31: Pictures of the test-bench

In a first stage, the plate is cooled down with a thermoelectric cell *Laird* CP2-127-10-L-RT-W4. However, as seen later on, this cell is not sufficiently efficient for the present application. This is why in a second stage, a self cooled assembly system *Laird* DA-075-12-02 is used. If ΔT stands for the temperature difference between the plate

and its environment, the presents a maximum cooling capacity of 71 W for $\Delta T = 0$ and a $\Delta T = 42$K for a null cooling capacity.

To record the frost accretion on the plate, pictures are taken from the top every 20 seconds. To prevent any disturbance from ambient light change (i.e. luminosity change in the room because of weather conditions), an opaque tent is installed around the test bench, as seen in Figure 2.31. A spotlight is installed inside it to provide the luminosity necessary to the pictures shooting.

2.3.2 Data monitoring

A hot wire anemometer measures the speed at the leading edge of the sample before each test. Four T-type thermocouples are installed in the box as shown in Figure 2.30. The plate temperature is also measured with T-type contact thermocouples. For the humidity, a sensor from Rotonic with the HF532 transmitter and HC2 probe is used. It shows an accuracy of ±0.8 %RH, ± 0.1 K, between 18 and 28 °C.

To shoot the frames, a Sony ILCE-6000 is employed. It shoots 6000x4000 pixels pictures. It has been set in ISO250, f/5.6 with an exposition time of 1/30 second.

Another measurement conducted, even if prior to any test, is the contact angles of the samples. The Cam 200 contact angle meter from KSV Instrument ltd is used.

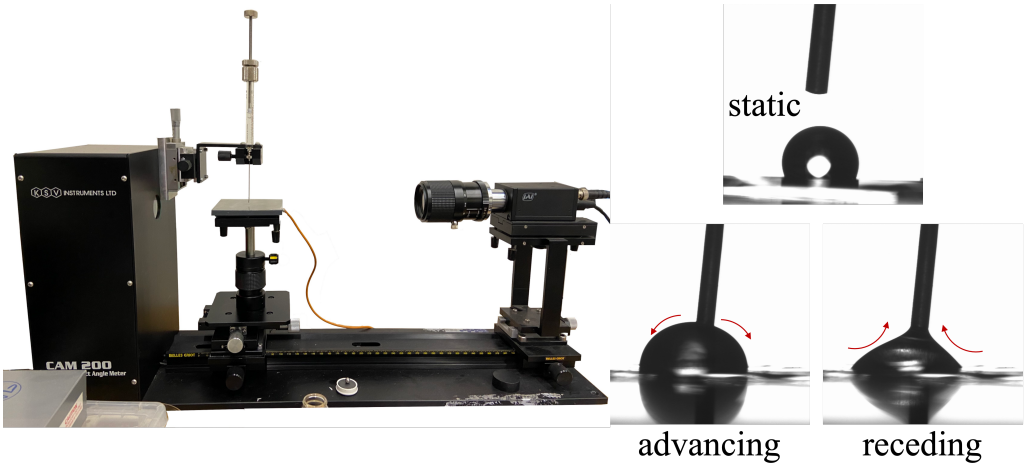

FIGURE 2.32: Contact angle measurement device and typical pictures taken for the static, advancing and receding contact angles

The pictures of the droplets are then analyzed with Attension Theta Software, to determine the different contact angles of the samples.

2.3.3 Experimental campaign tests

First experimental campaign tests on coated samples

The first idea was to study samples from actual heat exchanger fin, to get the closest match between the simple geometry and the evaporator as illustrated in Figure 2.33. Different coatings were applied to such samples, presenting static contact angles between 69° and 115° and hysteresis angles between 20° and 57°. Obviously, these

FIGURE 2.33: Picture of the first sample, made from fin

coatings present hydrophilic or hydrophobic characteristics. However, no superhydrophobicity is considered at this stage.

Ultimately, the objective is to correlate the nucleation phase duration to the plate temperature, air conditions and surface wettability. In a first time, a total of four different tests are presented, whose conditions are summarized in Table 2.5.

TABLE 2.5: Operating conditions for the different tests on surface samples

Test	$T_{\text{air},\infty}$ [°C]	RH_∞ [%]	u [m/s]	T_{wall}	θ [°]	$\theta_{\text{hysteresis}}$ [°]
1	14	82	0.2	-5.5	93	48
2	14	82	0.2	-5.5	115	60
3	14	82	0.2	-10.7	93	48
4	14	82	0.2	-7.2	115	60

Basically, the most hydrophobic coating is compared to the original aluminum fin at different wall temperatures. Tests 1 and 2 (i.e. same conditions, different coating) are compared to each other. Here, the exposed pictures correspond to three different times (0, 10 and 20 minutes).

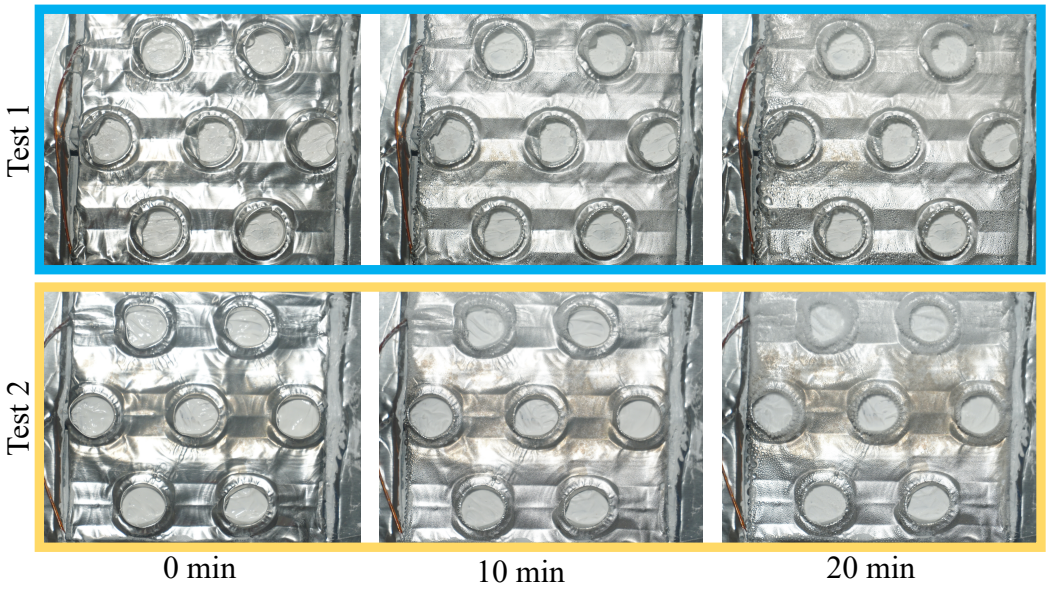

FIGURE 2.34: Pictures of bare (Test 1) and hydrophobic (Test 2) plates for three different times

As evoked in Section 2.3.2, a striking information is that the top of the pictures present frost initiation while the bottom does not. It is due to a thermoelectric cell default. The contact thermocouples confirmed an uneven temperature distribution over the plate. However, without any accurate analysis based on image processing, it can be seen that no obvious difference is noticed between the bare and coated plates. This is confirmed with the comparison of Tests 3 and 4 in Figure 2.35.

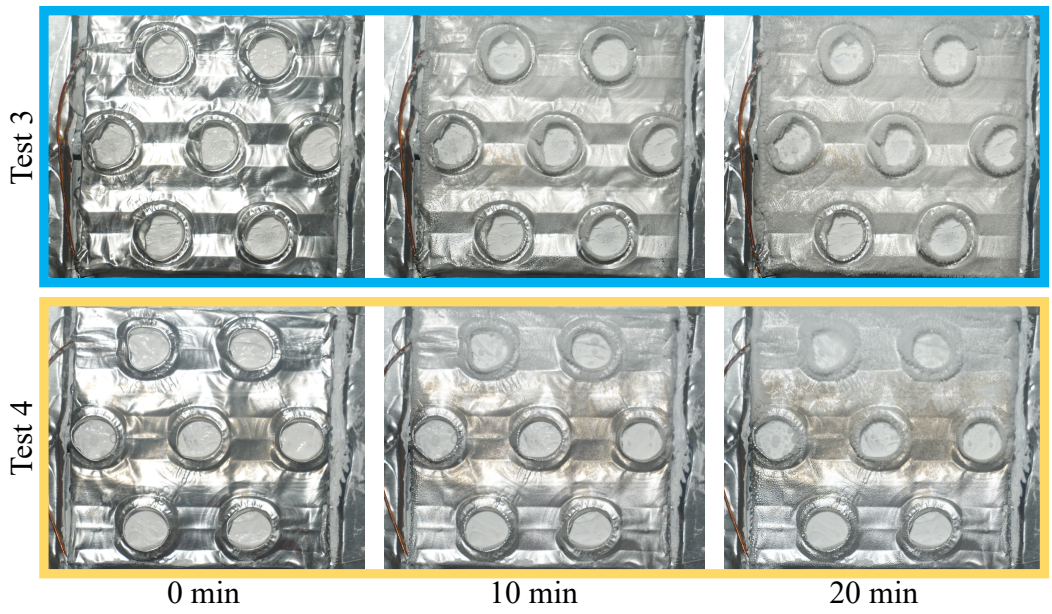

FIGURE 2.35: Pictures of bare (Test 3) and hydrophobic (Test 4) plates for three different times

Even if the plate temperature is lower for the non-treated plate compared to the coated one (due to some operating issues), at first sight, more frost seems to accumulates on the hydrophobic coating. It leads that, because of the relatively small sampling surface (62x62 mm) and because of the holes in the plate, side effects are important. However, beside those, no clear effect can be distinguished.

Based on these simple tests, conclusions are the following:

- Hydrophobic coatings showing a contact angle up to 115° do not show significant impact on the frost formation delay. This information confirms the findings of Hermes et al. [32] ;
- For small sample surfaces, a particular attention should be dedicated to side effects ;
- Because of the corrugated shape of the fins, it is complex to correctly apply the fin on the cooling plate, even with thermal paste ;
- Still because of the corrugations, a systematic image treatment is difficult to be put in place, because of the random light reflections.

Second experimental campaign tests on coated samples

Based on the previous outcomes, a different approach is considered. First, a more reliable thermoelectric cell cools down the different samples. Then, even if it is slightly further from the original exchanger fins, a perfectly plane and smooth sample is adopted.

It eliminates the main side effects, it facilitates the image treatment and it is easier to apply on the cooling element. More importantly, a further step is made in the hydrophobicity, using a superhydrophobic paint from NTTAT called HIREC^{TM}, which is a fluorine resin paint solvent (solvent-based). It shows a static contact angle of 162° and a hysteresis angle of 9°. However, this paint is white, which implies a big difference compared to the aluminum color and a complexity to observe frost accumulation.

A numerical tool should be implemented to get a rigorous criterion to determine if the plate is dry, in nucleation phase or frosted. It should be recalled here that the objective of this experimental campaign is to measure the nucleation phase duration, regarding the surface characteristics and atmospheric conditions. To do so, two different techniques are investigated in parallel.

The first technique is based on the so-called image subtraction. A picture is nothing more than a matrix where each element represents a pixel. Considering an additive color model, each pixel can be defined by its RGB (Red Green Blue) combination where each color has an intensity between 0 and 255. If two pictures of the same size (same number of pixels) are expressed in the RGB matrix convention, those matrices can be subtracted. A subtraction illustration of two 4-pixel pictures is illustrated in Figure 2.36.

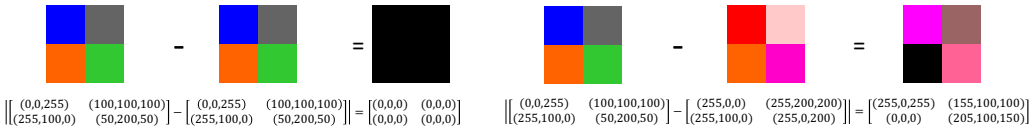

FIGURE 2.36: Illustration of image subtraction

Two pictures presenting the exact same pixels result in a null matrix (left) while two different pictures result in a new colors one (right). Based on this technique, it is possible to determine how different is a given picture compared to a reference one. In the specific context of frost detection, it is then possible to take advantage of this.

First, the first frame of the perfectly dry plate is chosen as the reference. Then, each frame (generated every 20 seconds in the present case) are compared to this reference. When liquid or ice nuclei start to appear, a difference is spotted, compared to the dry reference. During all the nucleation phase, this difference increases. However, at the time when the plate shows a uniform frost layer (end of the nucleation phase), this difference stabilizes, as the color variation is very low. At this precise stage, the nucleation phase is considered as over, leading to the frost growth phase. Figure 2.37 (left) illustrates the technique.

The RGB difference illustrated in the Figure 2.37 represents a double average. First, the difference of all pixels considered are averaged for the Red, Green and Blue matrices, respectively. Then, the mean of the three values found is taken. In the present application, it is easily shown that in practice, the Red Blue and Green matrices show the exact same trend. Averaging them does not imply any loss of information.

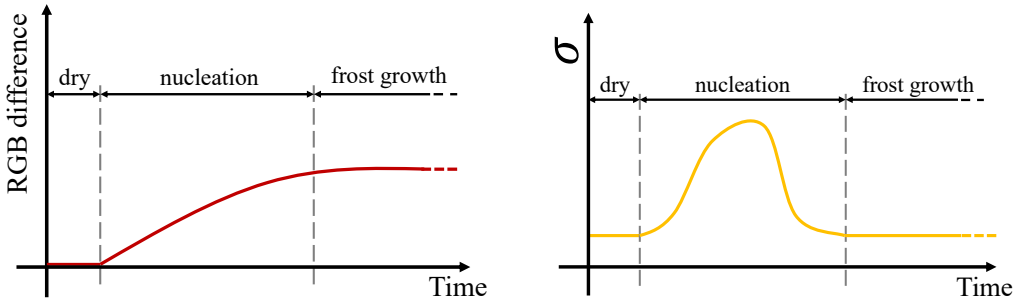

FIGURE 2.37: Illustration of the different frost formation phases, regarding the image subtraction technique (left) or the standard deviation analysis (right)

To reinforce the nucleation period determination, an additional technique is implemented. Still considering a picture as a RGB matrix, the objective is, for each frame, to compute their standard deviation σ. When the sample is dry, it shows uniform color, and then a low standard deviation (in space). When a nucleation phase starts, the colors become sparse implying a standard deviation increase. Finally, when reaching a uniform frost layer, the uniform color map and σ falls to low values again, as shown in Figure 2.37 (right).

Two comments may be raised. First, the opaque tent is determinant in this technique, as a random shadow may completely change the color map of a picture and then distort the results. Then, it is crucial to consider the outputs with a critical analysis of the different pictures in parallel. The breaking point is only to quantify and comfort the visual interpretation.

Two different tests have been picked to be analyzed intensively. The conditions are exactly the same for the two tests, beside the plate temperature. The ambient temperature and relative humidity are 18°C and 75%, respectively. The air speed is negligible (natural convection) and the surface temperature is first set to -5°C and to -11°C in a later time. The -11°C and -5°C is illustrated Figure 2.39 and 2.38, respectively (see next page). The choice is to show a representative portion of the aluminum and superhydrophobic samples at 0, 15, 30 and 45 minutes of the test. The analyzed portion shows 600x600 pixels. The RGB difference and standard deviation are then based on 3600 pixels for each sample.

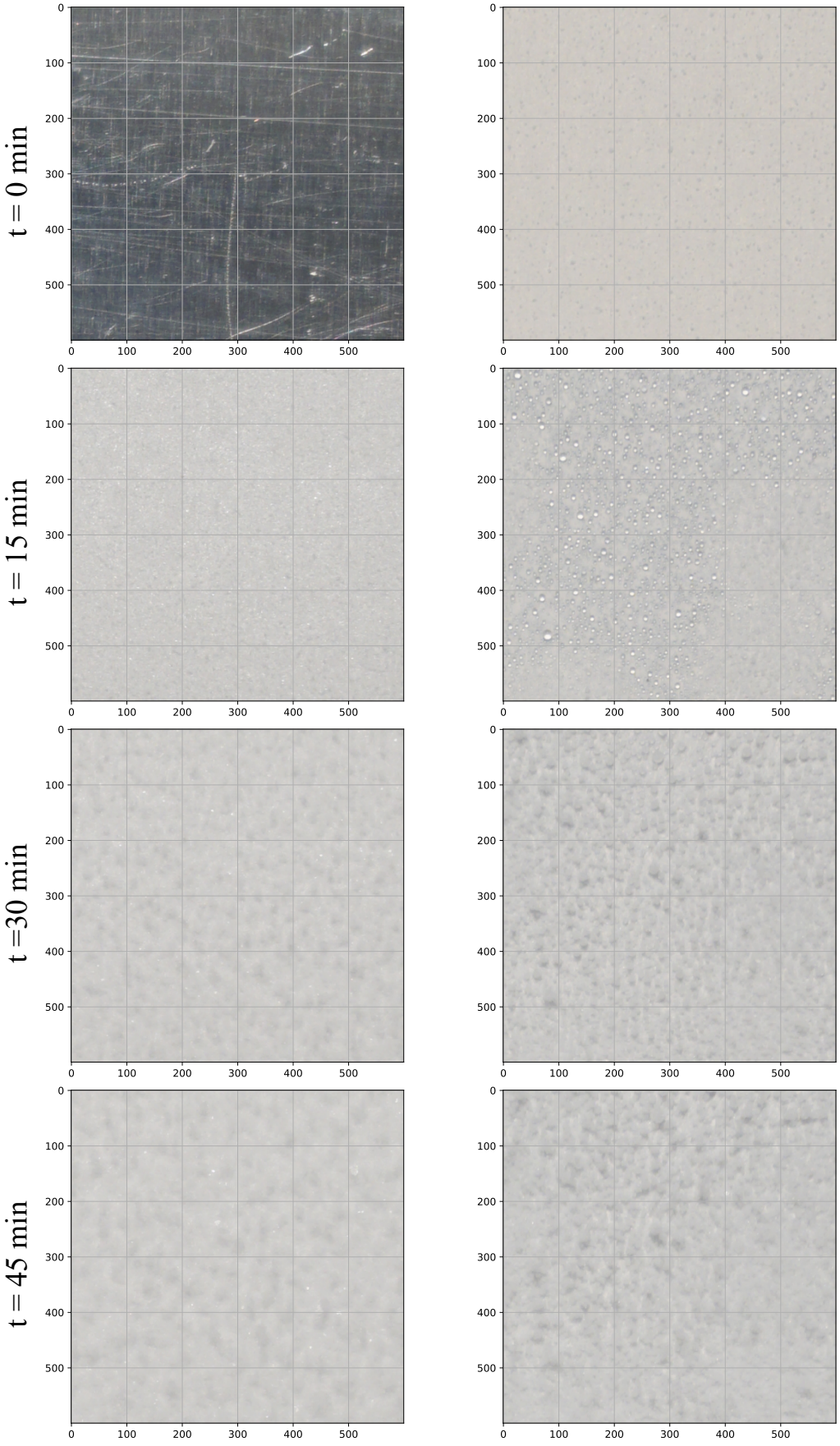

FIGURE 2.38: Pictures of the aluminum sample (left) and superhydrophobic HIREC^{TM} (right) at -11°C

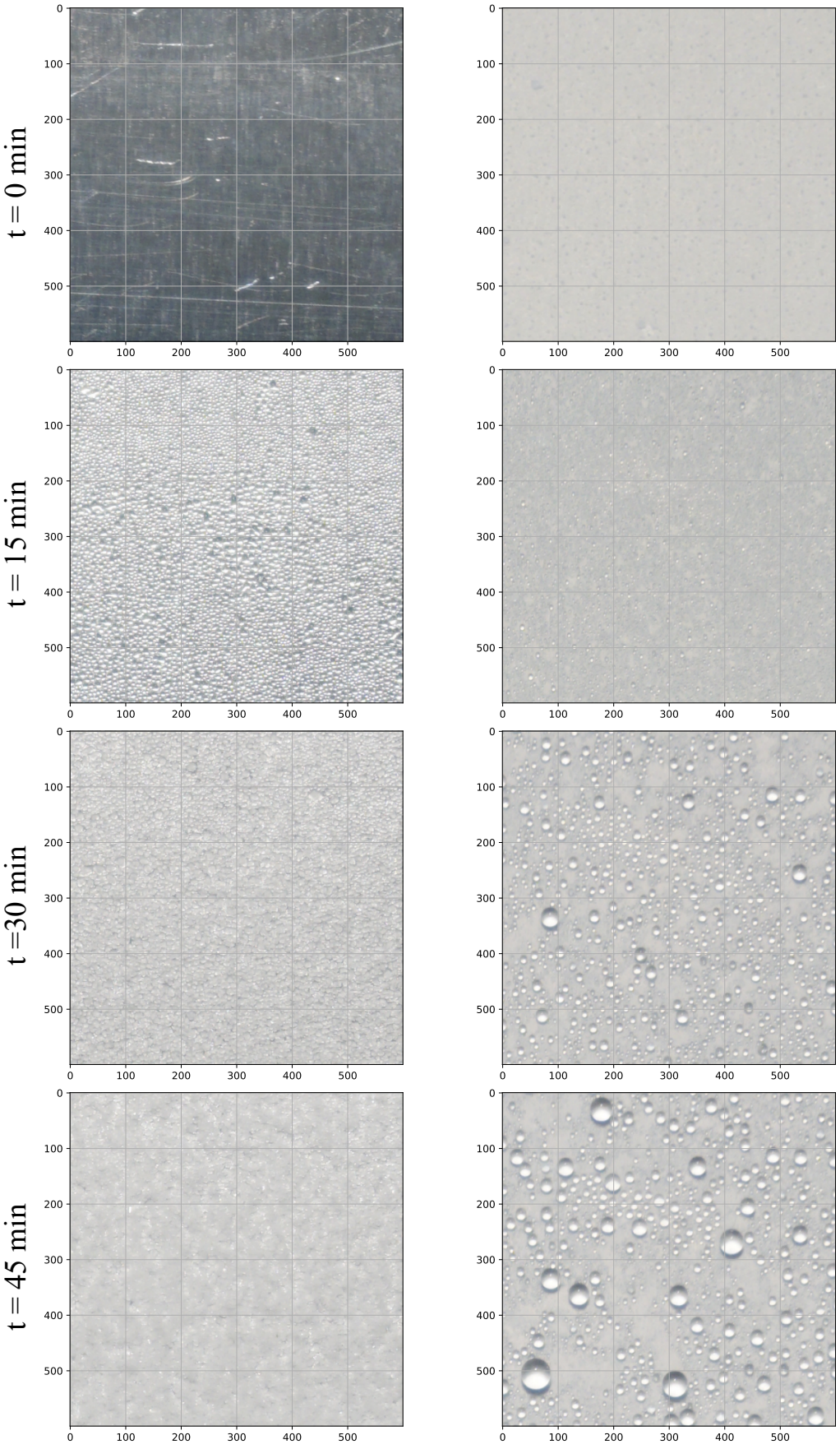

FIGURE 2.39: Pictures of the aluminum sample (left) and superhydrophobic HIREC^{TM} (right) at -5°C

The first comment is that the HIREC paint shows a white color. The color reference is then different from the aluminum and the frost formation is less marked.

For the -11°C case (Figure 2.38), frost formation occurs for both, aluminum and superhydrophobic surface. In these conditions and for this plate temperature, the superhydrophobicity does not allow to prevent frost. However, even at first sight, it is possible to observe an appearance delay. Indeed, at $t = 15$ minutes, the aluminum is already covered with a uniform layer, while the superydrophobic plate is only covered with some liquid droplets. The precise frost appearance shift is quantified later on, with the previously presented tools.

The -5°C case is different. Both samples see liquid nucleation after 15 minutes. For the aluminum, quite rapidly, the nuclei frost and soon turn into a uniform frost layer. For the superhydrophobic coating, a coalescence of the droplets is observed. The liquid droplets grow but do not freeze. It is seen later that even after a longer time (over 2 hours), the nuclei stay at the liquid state.

With those two different tests, multiple physical phenomena are underlined:

- Humidity can turn in frost, without passing through the liquid state (aluminum plate at -11°C) ;
- Humidity may condense into liquid droplet. In further times, those liquid nuclei can freeze (aluminum plate at -5°C, superhydrophobic plate at -11°C) ;
- Humidity may condense into liquid droplets stay at the liquid state, whatever the experiment length (superhydrophobic plate at -5°C) .

The physics behind those phenomena is detailed in Chapter 3. It is worth noticing that, when the liquid droplets pop on the superhydrophobic coating, they are very unstable and may roll for small tilt angles. Further investigations on vertical plates should be investigated but are not part of the present thesis.

After qualitative observations, the tools described previously to determine the nucleation phase duration are applied to the two tests. They are needed to quantify this period but, it is important to remember that an analysis of the pictures must be carried on in parallel. First, the test at -11°C is represented Figure 2.40. The normalized difference between the different frames and the reference as well as the normalized standard deviation σ are represented for the two different substrates. Even if chaotic variations can be noticed, trends conform to what is expected (see Figure 2.37) are observed. Combined to the visual analysis, it is determined that the nucleation duration is of 14 minutes for the aluminum and 29 minutes for the superhydrophobic coating. A difference of 15 minutes (i.e. positive delay) is observed between the two substrates. After this phase, the frost growth takes place and the frost deposition rate is similar in both situations (as the coatings are fully covered). It is worth noting that the "dry period" represented in Figure 2.37 is not noticeable here because it is extremely short

The same exercise is conducted for the plate at -5°C in Figure 2.41. After about 40 minutes, the indicators stabilize for the aluminum plate. This period is longer than the previous test, obviously because of the plate temperature difference. For the superhydrophobic coating, they increase until the end of more than two hours test.

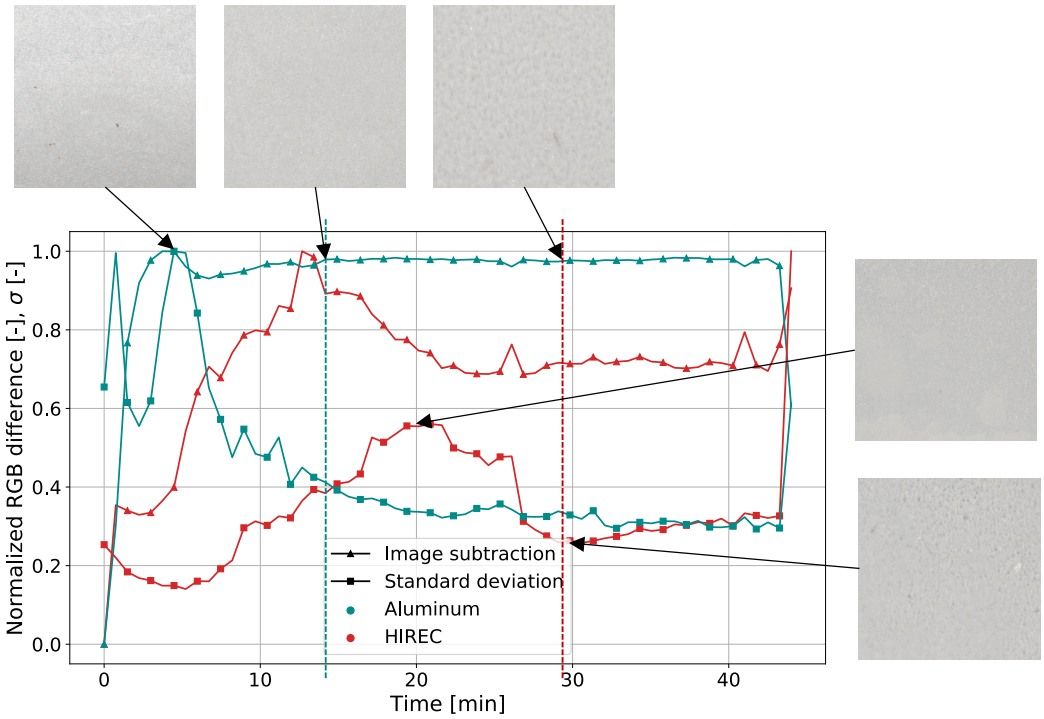

FIGURE 2.40: Normalized frame difference (RGB) and standard deviation for aluminum and superhydrophobic coatings with relevant pictures of the samples. Plate temperature = -11°C

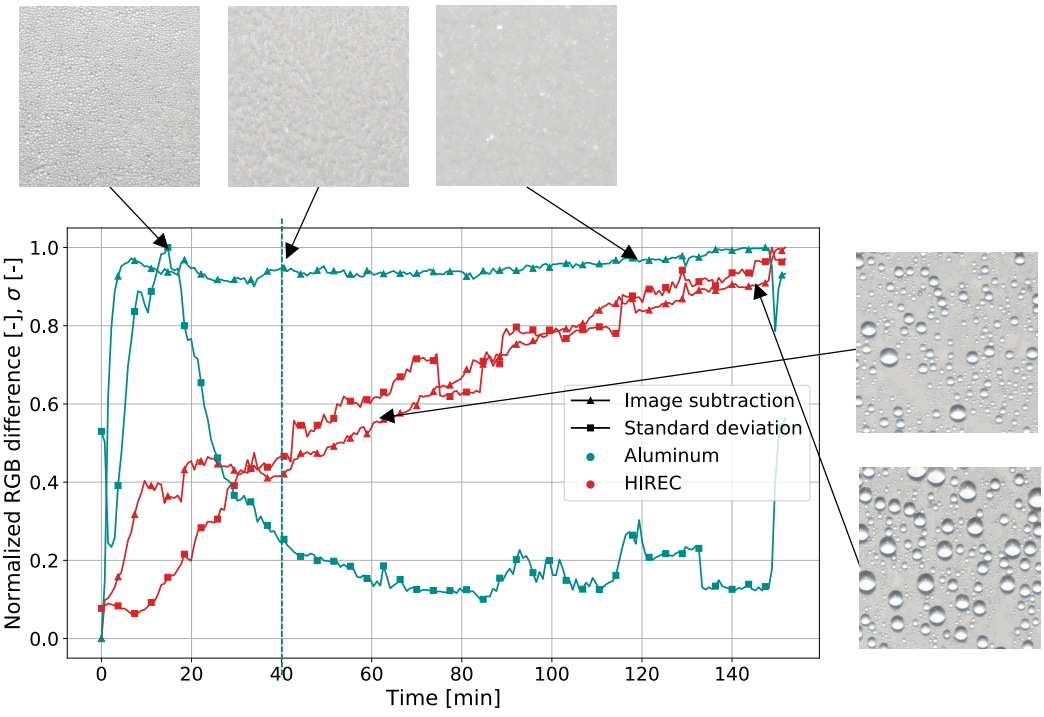

FIGURE 2.41: Normalized frame difference (RGB) and standard deviation for aluminum and superhydrophobic coatings with relevant pictures of the samples. Plate temperature = -5°C

Looking at the samples, it is explicit that droplets are liquid. The image difference and standard deviation increase as the droplets grow and move. This example clearly

shows that the image processing tool allows to determine the duration of the nucleation phase.

A total of 12 tests (on both substrates) were conducted, in natural convection context. The temperature and humidity are controlled to get an environment of 13 or 18°C and 75 or 90%, respectively. The results are presented Figure 2.42.

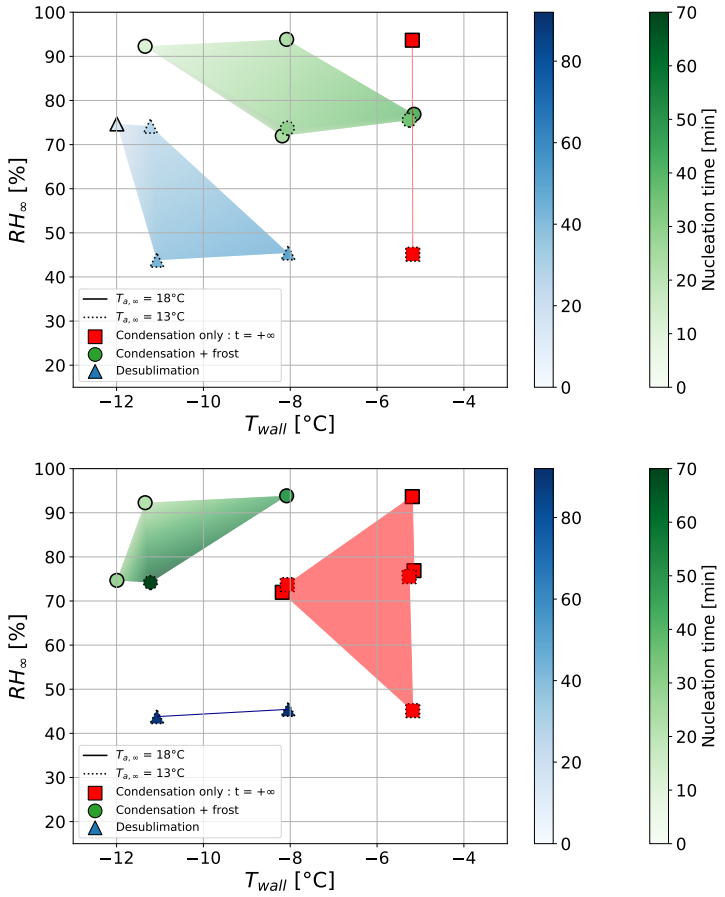

FIGURE 2.42: Experimental results of the campaign test on aluminum (top) and superhydrophobic coating (bottom). The discrete dots represent the actual experimental data while polygons are only interpolation.

Three different modes are observed. First, the water vapor may condensate and stay at liquid state during the complete test. It is reasonable to consider that it will never freeze in this situation, considering the duration of each test over two hours. Then, the humidity may condense in a first time to solidify then. Finally, the vapor may directly turns from vapor to ice nuclei through a desublimation process.

The two substrates show those mechanisms in the same map position but the size zones differ depending on the surface. Those phenomena can be classified as :

- Cold plate and dry air is favorable for desublimation ;
- Cold plate and humid air induces condensation followed by frost ;
- Warmer substrates will generate condensation and water droplets are likely to stay liquid.

Now, a differentiation between aluminum and superhydrophobic coating can be evaluated. Globally, it is clearly seen that superhydrophobic coating induces a longer nucleation phase (darker makers) and then a delay in the frost formation process compared to aluminum. Where the latter shows no frost (red squares) for plate temperatures around -5°C, for specific conditions, it is possible to decrease the temperature down to -8°C. Those temperature ranges are typical temperatures met in the evaporator of heat pumps. The present results then introduce a real interest of superhydrophobic coating for this application.

Moreover, a second type of test has been realized in forced convection mode. However, because of the characteristics of the thermoelectric cell, it was not possible to reach low temperatures when imposing an air speed which is not negligible. In this context only one test at -5°C is envisaged, in conditions as close as possible compared to the natural convection one. The air speed at the plate level was fluctuating between 1 and 1.3 m/s for a ambient temperature and humidity of 18°and 75%, respectively. It has been found that for the aluminum plate, relatively naturally, the nucleation phase was shorter (∼16 minutes) compared to natural convection (∼40 minutes). In these conditions, the superhydrophobic substrates stay liquid in both cases.

Those results will allow to establish and validates different surface models, described in the following chapter.

2.4 Summary and conclusions

This chapter aimed at describing two experimental facilities and at presenting the results of the corresponding experimental campaigns.

The first facility allowed to precisely measure experimental performance of a heat pump evaporator in either dry, wet or frost conditions. Innovative measuring techniques such as differential mass system or picture analysis were implemented to get a better understanding of frost behavior in such a device. Moreover, an infrared analysis of the different tubes allowed to underline an imbalance in the refrigerant distribution through the exchanger. The different tools implemented lead to a high quality experimental campaign determinant in the understanding of this evaporator in frost conditions.

The second facility was a simpler setup dedicated to the measurement of nucleation duration on different samples. The atmosphere and surface temperatures were controlled and a camera took snapshots every 20 seconds. The initial idea was to take fins of the evaporator as representative samples and apply them different hydrophobic coatings. However different issues were met, the main one being that no considerable difference in performance were measured between original fin showing a static contact angle of 92° and hydrophobic coatings having static contact angles around 115°. It has been decided to use a superhydrophobic coating (static contact angle of 162°) and smooth surface to considerably decrease the edge effects. In order to have a rational criterion to determine the end of nucleation phase, two numerical tools based on image treatments were implemented. The results of the campaign showed a net benefit for superhydrophobic coating with much larger nucleation period duration compared to the bare sample, especially for hotter surface (between -8°C and -5°C).

Chapter 3

Modeling Developments

3.1 Introduction

This third chapter focuses on the development of ad hoc modeling tools. As for the previous chapter, this one is built up from two main bricks, namely the model of the evaporator and the model of nucleation on hydrophobic surfaces.

Section 3.2 puts in equation the different physical phenomena observed in the previous chapter at the evaporator level. Those equations rely on well known thermophysical and hydraulic principles. The chosen approach is dynamic model, showing a tube-by-tube discretization, allowing to consider frost growth independently on each tube. The frost modeling developed at this point is a classical method for standard surfaces which does not account for the wettability of tubes and fins. A considerable add-on is the consideration of fin thermal conductivity in the model.

Section 3.3, second part of the chapter, is dedicated to surface phenomena in the nucleation period. First, basic principles of nucleation are recalled. Then the modeling method is detailed. It accounts for the wettability, the roughness, the inclination of the surface and for the nuclei temperature based on a heat balance at the droplet level. The ultimate objective of this modeling is to predict if the air humidity desublimates or condensates and in case of condensation event, to predict if the droplets stay at liquid state or if they freeze. In case of solid droplets accumulating on the surface, the model is able to determine how much time is necessary to cover a given surface. This duration corresponds to the nucleation phase.

In this chapter, the results provided by the different models are not compared to the experimental data, yet.

3.2 Evaporator modeling

3.2.1 A general approach

Geometrical definition

In a heat pump evaporator, in normal operation, the refrigerant shows an superheated zone. The system is tuned to reach that state and prevent damaging the compressor which generally cannot handle liquid. The well known ϵ-NTU method cannot be applied in its simplest shape in such conditions. Moreover, such a general approach implies that frost properties are constant throughout the exchanger. A more detailed technique is then implemented to increase the model accuracy.

When working with discretization, several levels of detail exist. Certainly, the most consistent is FEM/CFD modeling handling 3D finite-volumes, giving the best predictions but paying an expensive price in calculation resources and implementation. Besides, 1D control-volumes modeling also gives very satisfying results. It can be splitted in two approaches, namely constant energy control volumes and constant surface control volumes. The former considers that each element of discretization correspond to a constant heat transfer exchange between working fluids. It implies a exchange surface area varying from cell to cell [20]. The latter works in the other way around. The exchange surface area is fixed while the energy exchanged between fluids vary from cell to cell.

Another classification consists in specifying the way cells are defined. Safraz et al. [78] raised four usual techniques described in the literature.

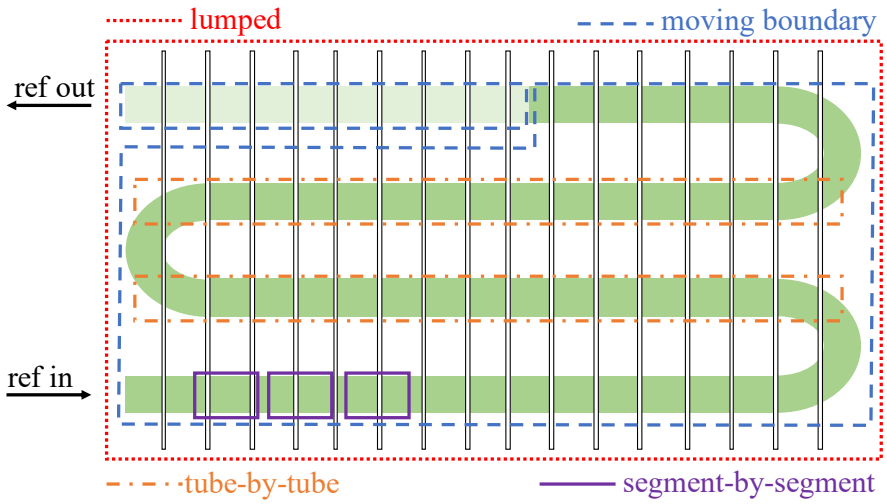

FIGURE 3.1: Different control volumes

From the most general to the most accurate, there are the lumped, the moving boundary, the tube-by-tube and the segment-by-segment methods, illustrated in Figure 3.1.

A fixed surface area control volume is picked in the frame of this thesis. From what has been observed in the experimental campaign, the choice made is a hybrid control volume definition. For the majority of the exchanger, it is split tube-by-tube. Indeed, what is observed on the air side is that frost appears on tubes in a sequential way. The level of discretization should then be at least tube-by-tube to be consistent. However, looking at a specific frosting tube, the frost grows in the same way on its whole length. Going in a segment-by-segment approach is therefore unnecessary. However, this is true if the considered tubes show the same state (two-phase or vapor) throughout the whole tube. If not, for the specific tube where the transition happens, a moving boundary is implemented to catch this specific case effects.

Even if the geometry can be chosen by the user, the specific geometry of the evaporator investigated in the experimental campaign is simulated. As a recall it is a 4-row tubes and fins heat exchanger. It has 12 tubes on its height split in 3 independent circuits. As mentioned previously, each cell of the model corresponds to one tube and its corresponding fins, except for the refrigerant transitional tube where a moving

boundary is imposed.

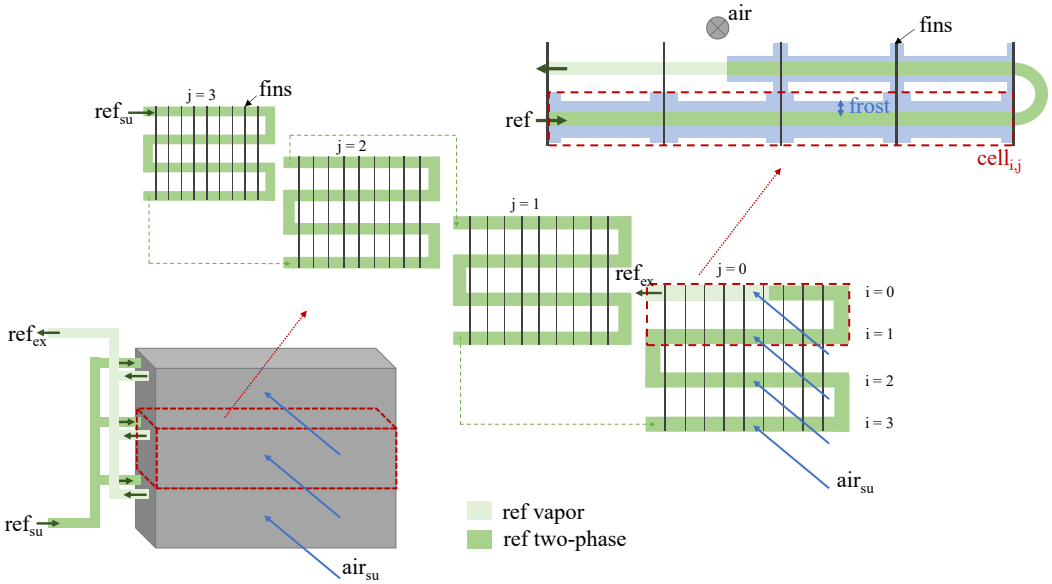

FIGURE 3.2: Geometry and control volume definition of the evaporator

General algorithm definition

The first idea was to develop a quasi-steady state model. Indeed, the working fluid input state is considered constant. Only frost impacts the conditions through time, but the rate of change is slow compared to the computation time-step. However, increasing the complexity of the model, robustness issues popped-out. The best solution found was to turn the model dynamic, with a wall thermal capacity.

The scheme of the general exchanger algorithm is graphically described in Figure 3.3.

The global idea is to have a heat transfer between the working fluids and the wall separating them (i.e. the tubes). At the beginning of the simulation, the exchanger is considered as *hot*, at the ambient temperature. The air and refrigerant flows are exchanging a certain amount of energy due to the temperature difference. Cross fin conductive heat transfer is also accounted in the model. A specific section is dedicated for this phenomenon due to its particular interest in the frame of this thesis. From the heat transfer algorithms, $\dot{Q}_{\text{air}}$, $\dot{Q}_{\text{ref}}$ and $\dot{Q}_{\text{x,fin}}$ are computed. Based on those quantities, the wall temperature for the cell i, j is updated, following the equation :

$$m \cdot C \cdot \frac{dT_{\text{wall,i,j}}}{dt} = \dot{Q}_{\text{ref,i,j}} - \dot{Q}_{\text{air,i,j}} - \dot{Q}_{\text{x,fin,i,j}} \tag{3.1}$$

For a given cell, the wall temperature is considered uniform for the complete cell.

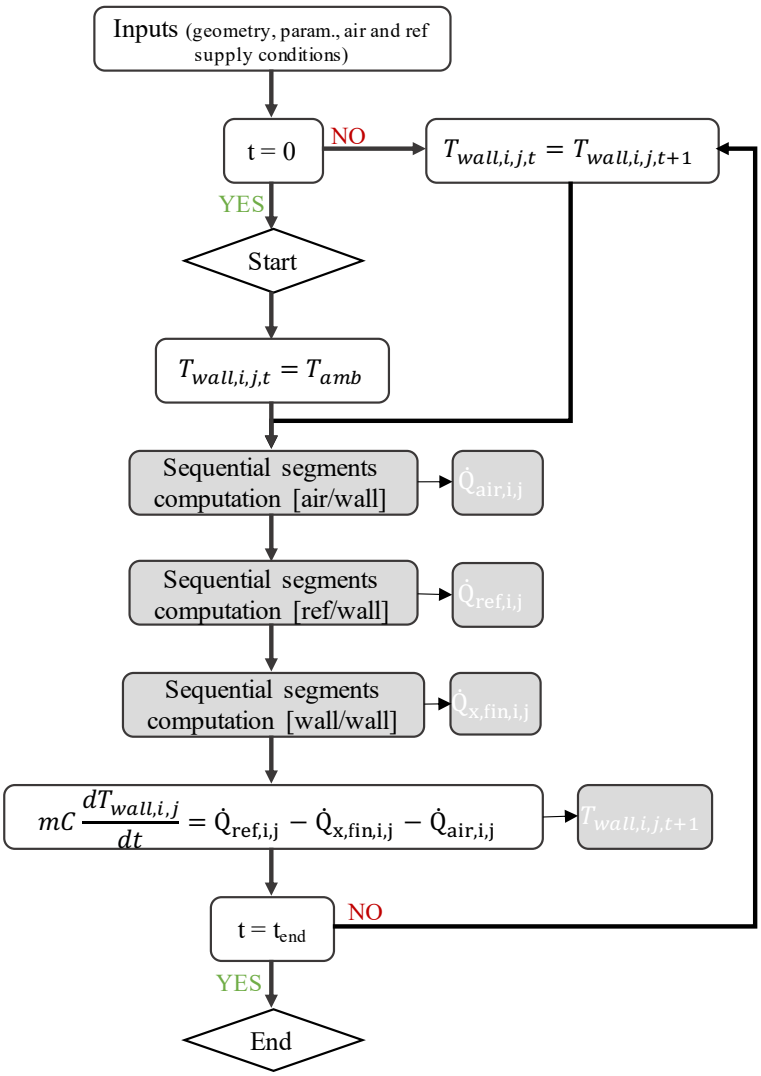

FIGURE 3.3: Exchanger algorithm flowchart

3.2.2 Segment heat transfer development : refrigerant side

The resolution of the heat transfer between wall and refrigerant is rather classical. The solver runs each cell sequentially, beginning from the refrigerant supply to finish at the exhaust. The supply conditions of the cell $n+1$ corresponds to the exhaust conditions of the cell n.

As evoked previously, each cell corresponds to a complete tube, except for the transition between two-phase and superheated phase. For each tube except one, the fluid is then either completely in two-phase or completely superheated.

Two-phase tube

While boiling, the refrigerant temperature is considered constant. It only depends on its pressure and considering a single tube, the pressure drops are small enough to neglect a temperature glide. This specific case corresponds to a heat transfer between

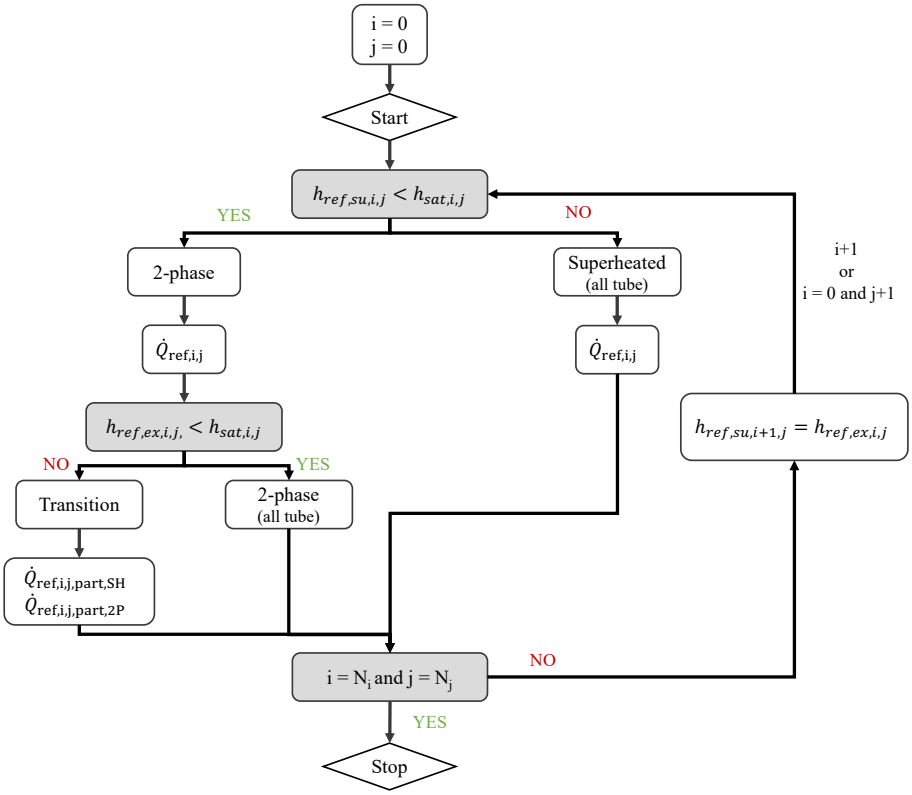

FIGURE 3.4: Refrigerant algorithm flowchart

two media at constant temperature. The classic heat transfer model is used.

$$\dot{Q}_{\text{ref,i,j}} = H_{\text{ref,i,j}} \cdot A_{\text{ref,i,j}} \cdot (T_{\text{wall,i,j}} - T_{\text{ref,su,i,j}}) \tag{3.2}$$

where $H_{\text{ref,i,j}}$ and $A_{\text{ref,i,j}}$ are the heat transfer coefficient and the exchange surface between wall and refrigerant, respectively.

Because of the exchanger geometry and more specifically the refrigerant split, the mass flux is relatively low, going from about 80 to 40 kg/m^2/s. Ma et al [56] conducted a study for smooth horizontal tubes for low mass fluxes. Different correlations from different authors are proposed and the one picked up for the model is the one from Kandlikar [41]. This choice is made because this model fits well, especially for very low mass fluxes. While refrigerant boiling, the correlation is based on two different contributions, namely the convective and nucleate boiling terms.

$$\frac{H_{\text{ref,2P}}}{H_{\text{ref,L}}} = C_1 \cdot Co^{C_2} \cdot (25 \cdot Fr_L)^{C_5} + C_3 \cdot Bo^{C_4} \cdot F_{fl} \tag{3.3}$$

where Co represents the convective number, Bo the boiling number, Fr the Froude number F_{fl} fluid dependent correction factor and C_i some constants. This correlation directly depends on the refrigerant quality, updated at the supply of each tube. Because it is not the main purpose of the thesis, a more detailed development is available in Appendix B.

Superheated tube

In the superheated zone, the heat transfer between the refrigerant and the wall is a semi-isothermal heat transfer. The well-known ϵ-NTU methods is implemented to compute the heat exchange.

$$\dot{Q}_{\text{ref,i,j}} = \epsilon \cdot \dot{C}_{\text{ref}} \cdot (T_{\text{wall,i,j}} - T_{\text{ref,su,i,j}}) \tag{3.4}$$

with

$$\epsilon = 1 - \exp(-NTU_{\text{ref}}) \tag{3.5}$$

$$NTU_{\text{ref}} = \frac{AU_{\text{ref}}}{\dot{C}_{\text{ref}}} \tag{3.6}$$

$\dot{C}_{\text{ref}}$ being the refrigerant capacity flowrate in [W/K] and AU_{ref} the refrigerant heat transfer conductance.

To determine AU_{ref}, the heat transfer coefficient $H_{\text{ref,SH}}$ is needed. It can be deduced from the well known equation linking this coefficient to the Nusselt number:

$$H_{\text{ref,SH}} = \frac{Nu \cdot k}{D_h} \tag{3.7}$$

Nu is determined with the Dittus-Boelter equation from Incropera and Dewitt reference book [9]:
if Re >1e4,

$$Nu = 0.023 \cdot Re^{4/5} \cdot Pr^{0.4} \tag{3.8}$$

if $Re < 2300$,

$$Nu = 4.36 \tag{3.9}$$

and a weighted average of Eq.(3.8) and Eq.(3.9) if Re is in between those values.

Transition

Transition tube is found while the refrigerant exhaust specific enthalpy is greater than the vapor saturation specific enthalpy. When transition occurs, none of the method described before can be applied on its own. The objective is to find the proportion of the tube in two-phase state. The amount of energy needed is easily deduced, knowing the saturation specific enthalpy:

$$\dot{Q}_{\text{ref,i,j,part,2P}} = \dot{M}_{\text{ref}} \cdot (h_{\text{ref,sat}} - h_{\text{ref,i,j,su}}) \tag{3.10}$$

Knowing $\dot{Q}_{\text{ref,i,j,part,2P}}$, the corresponding exchange surface (i.e. the proportion of the tube) can be deduced, rearranging Eq.(3.2).

3.2.3 Segment heat transfer development : air side generalities

The air side shows higher complexity in the modeling. Indeed, depending on its supply conditions and wall temperature, the moisture naturally present in the air may stay at a vapor state, can condensate in a liquid form or can frost on the wall, involving specific heat transfer considerations.

For sake of simplicity, without losing considerable accuracy, a given tube is considered entirely dry, wet or frosted. This assumption is confirmed by the experimental

observations. In a first step, the regime definition is only based on the wall temperature and not on its nature (wettability)

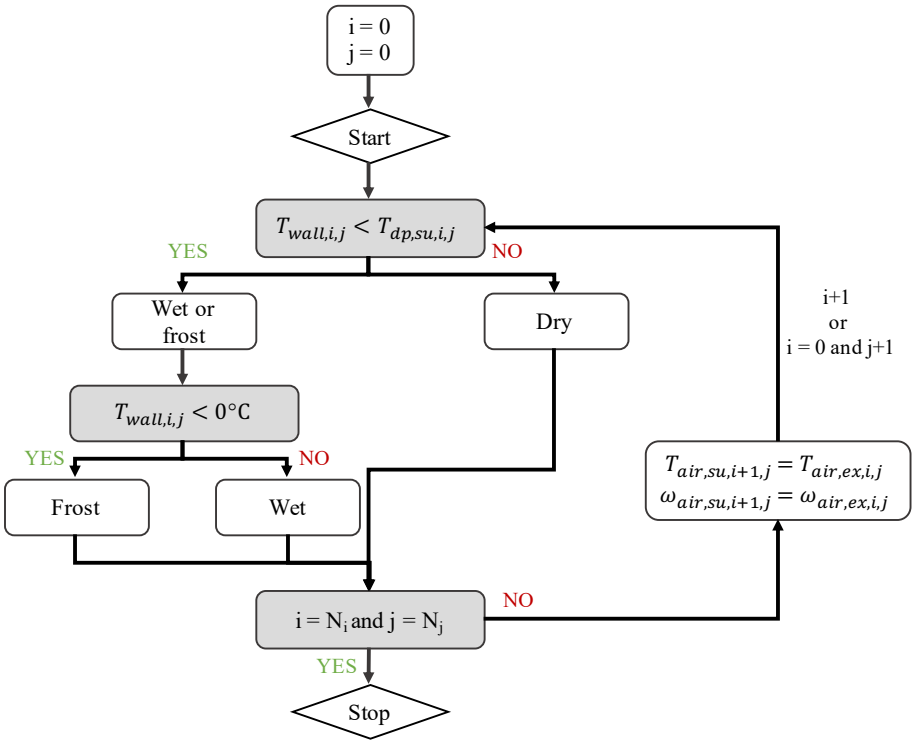

FIGURE 3.5: Air algorithm flowchart

3.2.4 Segment heat transfer development : air side in dry regime

The dry regime is the simplest to model. The objective is to describe the heat exchange between the air and the surface without any moisture condensation. The exchange surface corresponds to the outer surface of tubes and the fins. The surface temperature is considered as constant. However, if the assumption is good for the tubes, it may not be the case for the fins where a temperature gradient takes place. The trick put in place is to use a fin efficiency, to decrease the overall heat transfer coefficient.

As there is no condensation on the air side, as for the refrigerant, a classical ϵ-NTU method is implemented. The wall is also considered as isothermal, so same equations as in Section 3.2.2 can be used. The only difference, as evoked before, is the presence of fins, which was not the case on refrigerant side. It is expressed in the definition of the global heat transfer coefficient AU.

$$AU_{\text{air}} = (A_{\text{tube}} + A_{\text{fins}}) \cdot \eta_{\text{surf}} \cdot H_{\text{air}} \tag{3.11}$$

with η_{surf} being the surface efficiency. It penalizes the heat transfer coefficient to account for the fact that the complete surface is not at the wall temperature. Accordingly to VDI Heat Atlas [89], the surface efficiency is expressed as:

$$\eta_{\text{surf}} = 1 - \frac{A_{\text{fin}}}{A_{\text{tot}}} \cdot (1 - \eta_{\text{fin}}) \tag{3.12}$$

where η_{fin} is the fin efficiency, dependent on the fin and exchanger geometry. Still from the VDI Heat Atlas, η_{fin} can be defined like:

$$\eta_{\text{fin}} = \frac{\tanh(X)}{X} \tag{3.13}$$

In dry conditions, Xi and Jacobi [98] expressed X in the following way:

$$X = \kappa \cdot \frac{L_{\text{fin,height}}}{2} \tag{3.14}$$

$L_{\text{fin,height}}$ being the fin height and κ

$$\kappa = \sqrt{\frac{H_{\text{air}} \cdot (\beta/c_p)}{k_{\text{fin}} \cdot L_{\text{fin,thick}}/2}} \tag{3.15}$$

β being a linearization parameter. The ratio β/c_p is chosen to be taken equal to 1.3. In [98] this value is taken for air between -20°C and 0°C and relative humidity between 0% and 80%. In those conditions, condensation or frost often occurs. However, as seen later on, this value shows still good results for dry conditions with positive temperatures.

The heat transfer coefficient H_{air} is determined with the Youn and Kim researches [106] on airside performance of exchangers having staggered fins. The Eq.(3.7) is still valid on the air side. However the Nusselt number is expressed as :

$$Nu = j \cdot Re \cdot Pr^{1/3} \tag{3.16}$$

with j being an empirical coefficient dependent of the geometry of the exchanger.

3.2.5 Segment heat transfer development : air side in wet regime

As seen upward, dry regime is rather simple to model, having only sensible transfer heat. However, in evaporators, the wall surface may have a surface temperature below the air dew-point. In that situation, moisture present in the air would go liquid, releasing some latent energy that can be recovered. This latent energy must be well predicted to have a consistent model.

As the model is already descretized in many cells, no dedication is brought to determine if a given cell is partially or completely wet. The cell is either completely dry or completely wet. At the level of a complete exchanger (i.e. without descretization), Braun [10] showed that considering the maximum of completely dry or completely wet coil would lead to a maximum power prediction of 5%. With such an error on a single tube, it is easy to guess that this error at the exchanger scale will be even less than 5%

The method chosen to model a completely wet tube is the one proposed by Lebrun et al. [47]. This method is relatively simple to drive quick calculations but still accurate enough to provide good predictions. The method is a generalized form of Braun model [10], based on a capital simplification:

"*linearization of the relationship between saturated air enthalpy and corresponding temperatures*"[47].

The generalization comes from the use of wet-bulb temperatures as driving potential instead of enthalpies. Further details can be found in the demonstration recalled in Appendix C. The total exchanged power between air and wall in wet regime for a tube i, j is expressed as:

$$\dot{Q}_{\text{air,i,j}} = \dot{C}_{\text{fict}} \cdot (T_{\text{wb,su,i,j}} - T_{\text{wb,ex,i,j}}) \tag{3.17}$$

$$\dot{Q}_{\text{air,i,j}} = \epsilon \cdot \dot{C}_{\text{fict}} \cdot (T_{\text{wb,su,i,j}} - T_{\text{wall,i,j}}) \tag{3.18}$$

where $\dot{C}_{\text{fict}}$ is a fictitious air capacity flowrate $\dot{M}_{\text{air}} \cdot cp_{\text{fict}}$, with cp_{fict} a fictitious air specific heat capacity. The idea behind this equation is to replace the moist air by a fictitious perfect gas whose enthalpy is fully defined by the air wet-bulb temperature. It is possible only by applying the simplification aforementioned. To respect the first principle of thermodynamic, the fictitious air specific heat is defined as:

$$cp_{\text{fict}} = \frac{h_{\text{a,su}} - h_{\text{a,ex}}}{T_{\text{wb,su,i,j}} - T_{\text{wb,ex,i,j}}} \tag{3.19}$$

The ϵ of Eq.(3.18) is the one of the ϵ-NTU method described above. The convective coefficient H_{air} is considered as the same as in the dry regime, neglecting a potential water film on fins.

3.2.6 Segment heat transfer development : air side in frost regime

As recalled in the introduction (Chapter 1), frost growth occurs in different stages, namely the nucleation and frost growth for the simplified case. As Hermes et al. [33] showed, apparent contact angles of 123° or less does not show significant impact on frost delay (i.e. on nucleation phase time increase). It means that a majority (to the author's knowledge, *all*) the models present in the literature at the exchanger scale simply neglect the nucleation phase. This simplification is made because of the time scale of nucleation (very short) compared to tests duration in refrigeration fields (from tens minutes to hours). If the substrate is getting more hydrophobic, the nucleation process may last longer, getting more impact on the modeling. This literature gap needs to be filled, which is the purpose of the present thesis.

For this current section, only the frost growth method in the evaporator is detailed. A specific modeling section is dedicated to nucleation on coated surfaces later on, to be ultimately merged to the exchanger model, leading to a global and versatile model.

Assumptions

The proposed model of frost growth regime is mainly based on different publications [14, 17, 29, 34, 48, 50, 64]. The experimental data released by Hermes et al. [34] is used to validate the presented model. However the data corresponds to a frost growth on a flat horizontal place. Later, the need of tuning some parameters is shown for the model prediction to meet the experimental data, at the exchanger level. The model relies on different assumptions, widely found in the literature:

- Heat and mass transfers are supposed to be steady state and 1D
- The air pressure is constant (101 235 Pa) in the air stream and frost layer

- The frost density is averaged in the frost thickness
- For a given cell (tube), the frost thickness is constant, and the same on fins and tubes
- The Lewis analogy (i.e. analogy between heat and mass transfers) is applicable
- The frost thermal conductivity only depends on its density

As illustrated in Figure 3.6, the majority of the models split the mass flux $\dot{m}$ into two different parts, namely the growth $\dot{m}_g$ and the densification $\dot{m}_d$. The first contributes to the increase of the frost thickness x_{frost}, while the second one increases the density of the frost layer.

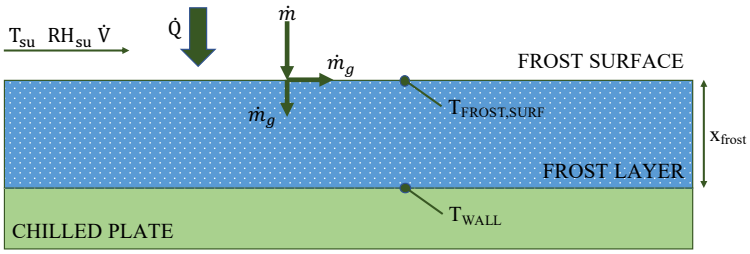

FIGURE 3.6: Air - frost interface

Empirical correlations

The model is based on different empirical correlations for the following quantities:

Vapor diffusivity in air :
The vapor diffusivity D [m^2/s] is considered as function of the temperature and pressure. The Ashrae Handbook [5] gives an empirical equation for the diffusivity of water vapor in air up to 1000°C:

$$D_v = \frac{0.000146}{P_{\text{atm}}/101325} \cdot \frac{\left(T \cdot \frac{9}{5}\right)^{2.5}}{\left(T \cdot \frac{9}{5}\right) + 441} \cdot \frac{929.0304}{3600} \tag{3.20}$$

expressed in cm^2/s with T in K and P_{atm} in Pa.

Frost density :
Different authors proposed correlations to predict frost density. For instance, Hayashi [29] linked it to frost surface temperature. On another hand, Hermes et al. [34] add the wall temperature effect whith the following equation:

$$\rho_{\text{frost}} = a \cdot \exp(b \cdot T_{\text{frost,surf}} + c \cdot T_{\text{wall}}) \tag{3.21}$$

The a, b and c coefficients taking the value of 207.3 kg/m^3, 0.266 $°C^{-1}$ and -0.0615$°C^{-1}$, respectively. It will be seen later that this correlation fits very well experimental results on a flat plate. However, for frost accretion in heat exchanger better results are found, using correlation from Da Silva et al. [17] correlating the density to the surface and air dew-point temperatures :

$$\rho_{\text{frost}} = a \cdot \exp(b \cdot T_{\text{frost,surf}} + c \cdot T_{\text{dp}}) \tag{3.22}$$

Da Silva found coefficients a, b and c of 494 kg/m^3, 0.11 °C^{-1} and -0.06°C^{-1}. Those were found minimizing the RMSD between measured and calculated pressure drops.

Frost thermal conductivity :
Different correlations of frost thermal conductivity can be found in literature, all depending on frost density [48, 68, 104]. The picked one is the most recent one from the three cited, from Lee et al. [48]:

$$k_{\text{frost}} = 0.132 + 4.13 \cdot 10^{-4} \cdot \rho_{\text{frost}} + 1.6 \cdot 10^{-7} \cdot \rho_{\text{frost}}^2 \tag{3.23}$$

Heat and mass transfers

First, it is important to note that the convective heat transfer coefficient differs if a single smooth plate is involved or a complete exchanger. For the frost growth validation on a simple plate, this coefficient is deduced from the Nusselt number proposed by Yamakawa et al. [101] as suggested by Hermes et al. [34] :

$$Nu = 0.034 \cdot Re^{0.8} \tag{3.24}$$

The convective heat transfer coefficient can be found using Eq.(3.7).

Now, for the exchanger case, the same correlations as for the heat transfer in dry or wet case is implemented with Eq.(3.16). The coefficient j and the Reynolds number needed in this equation is, as previously said, dependent on the geometry. However, frost growth will have a significant impact on the geometry.

The evolving quantity that will impact all the others (air speed, Reynolds number,...) is the air cross-section area. Considering a frost thickness at time t for a given cell and the nomenclature of Figure 3.7, the air cross-section area can be expressed as :

$$A_{\text{CS}} = (L_h - D_{\text{ext}} - 2 \cdot x_{\text{frost}}) \cdot (L_{\text{tube}} - N_{\text{fins}} \cdot (L_{\text{fin,thick}} + 2 \cdot x_{\text{frost}})) \tag{3.25}$$

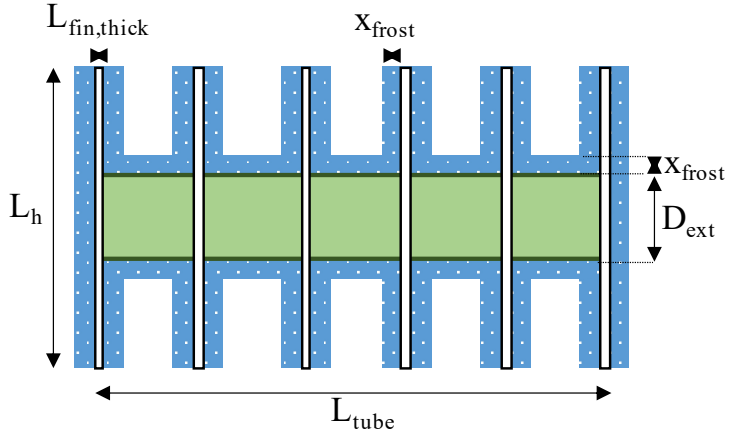

FIGURE 3.7: Nomenclature for air cross section computation

Another modeling difference between the frost regime and dry or wet ones is the way to express the fin efficiency. Indeed, as frost accumulates, this efficiency tends to decrease. Xia et al. [98], as for the dry conditions, investigate the fin efficiency in frosting conditions. Based on a logarithmic-mean difference method, they formulate

fin and surface efficiency for those composite materials (metal+frost).

$$\eta_{\text{surf}} = \frac{A_{\text{fin}}}{A_{\text{tot}}} \cdot \eta_{\text{fin}} + \left(\frac{k_{\text{frost}}/x_{\text{frost}}}{H_{\text{air}} \cdot (\beta/cp_{\text{air}}) + k_{\text{frost}}/x_{\text{frost}}} \right) \cdot \frac{A_{\text{tot}} - A_{\text{fin}}}{A_{\text{tot}}} \tag{3.26}$$

β being a linearization coefficient and ratio (β/cp_{air}) being set to 1.3. Neglecting the conduction heat transfer in the frost layer parallel to the length of the fin, the fin efficiency is formulated as :

$$\eta_{\text{fin}} = \frac{2 \cdot \lambda}{H_{\text{air}} \cdot (\beta/cp_{\text{air}}) \cdot L_h \cdot x_{\text{frost}}} \cdot \tanh\left(\frac{\lambda \cdot L_h}{2 \cdot x_{\text{frost}}} \right) \cdot k_{\text{fin}} \cdot L_{\text{fin,thick}}/2 \tag{3.27}$$

$$\lambda = x_{\text{frost}} \cdot \left[\frac{H_{\text{air}} \cdot (\beta/cp_{\text{air}})}{k_{\text{fin}} \cdot L_{\text{fin,thick}}/2 + x_{\text{frost}} \cdot [k_{\text{fin}} \cdot H_{\text{air}} \cdot (\beta/cp_{\text{air}}) \cdot L_{\text{fin,thick}}/2/k_{\text{frost}}]} \right]^{0.5} \tag{3.28}$$

In case of frost event, beside the heat transfer there is obviously a mass transfer phenomenon. Making an analogy to the convective heating transfer coefficient a mass transfer coefficient H_m can be defined, applying the Lewis boundary layer analogy :

$$H_m = \frac{H_{\text{air}}}{cp_{\text{air}} \cdot Le^{2/3}} \tag{3.29}$$

Le being the Lewis number and defined as:

$$Le = \frac{\alpha}{D_{\text{eff}}} \tag{3.30}$$

with D_{eff} being the effective diffusivity, defined as $D_{\text{eff}} = \epsilon/\tau \cdot D_v$. α, τ and ϵ are respectively the thermal diffusivity, the tortuosity and the porosity of the frost layer. The tortuosity is a representation of the water vapor molecular diffusion in the frost layer. It is deduced from the model of Na [64]:

$$\tau = \frac{\epsilon}{1 - \sqrt{1 - \epsilon}} \tag{3.31}$$

The porosity of the frost layer is defined as:

$$\epsilon = \frac{\rho_{\text{frost}} - \rho_{\text{ice}}}{\rho_{\text{vap}} - \rho_{\text{ice}}} \tag{3.32}$$

with ρ_{ice} set to 917 kg/m^3.

Sensible and latent heat transfers occur simultaneously, because of temperature and humidity difference between air and surface of the frost layer. The total, sensible and latent heat flux per unit of surface are respectively given by :

$$\dot{q}_{\text{tot}} = \dot{q}_{\text{sens}} + \dot{q}_{\text{lat}} \tag{3.33}$$

$$\dot{q}_{\text{sens}} = H_{\text{air}} \cdot (T_{\text{air,su}} - T_{\text{frost,surf}}) \tag{3.34}$$

$$\dot{q}_{\text{lat}} = H_m \cdot (\omega_{\text{air,su}} - \omega_{\text{frost,surf}}) \cdot L_s \tag{3.35}$$

with L_s the latent heat of sublimation, set to 2838 kJ/kg.

Looking at the mass transfer rate of frost per unit of surface, the following general equations can be written :

$$\dot{m}_{\text{frost}} = H_m \cdot (\omega_{\text{air,su}} - \omega_{\text{frost,surf}}) \tag{3.36}$$

$$\dot{m}_{\text{frost}} = \frac{\mathrm{d}\left(x_{\text{frost}} \cdot \rho_{\text{frost}}\right)}{\mathrm{d}t} = x_{\text{frost}} \cdot \frac{\mathrm{d}\rho_{\text{frost}}}{\mathrm{d}t} + \rho_{\text{frost}} \cdot \frac{\mathrm{d}x_{\text{frost}}}{\mathrm{d}t} = \dot{m}_{\text{d}} + \dot{m}_{\text{g}} \tag{3.37}$$

with $\dot{m}_d$ and $\dot{m}_g$ corresponding to the densification and growth terms illustrated in Figure 3.6. To determine the ratio of each term, mass and energy balances must be expressed. For a given control volume, the governing equations are the following:

$$D_{\text{eff}} \cdot \frac{\mathrm{d}^2\omega}{\mathrm{d}x^2} = \alpha_{\text{frost}} \cdot \omega \tag{3.38}$$

$$k_{\text{frost}} \cdot \frac{\mathrm{d}^2 T}{\mathrm{d}x^2} = \alpha_{\text{frost}} \cdot \rho_{\text{air}} \cdot L_s \cdot \omega \tag{3.39}$$

with α_{frost} a coefficient of absorption to be determined. Eq.(3.38) and Eq.(3.39) correspond respectively to the diffusion and heat equations, considering latent heat from a phase change of the water vapor in the frost layer and the vapor diffusion in the normal direction only. To solve those equations, boundary conditions are determined and detailed by Wang et al. [93].

Solving Eq.(3.38) and Eq.(3.39) using the proper boundary conditions, Chung et al. [16] determined the humidity ratio of the water vapor within the frost layer, and the frost surface temperature:

$$\omega(x) = \omega_{\text{wall}} \cdot \cosh\left(Ha \cdot \frac{x}{x_{\text{frost,surf}}}\right) \tag{3.40}$$

$$T_{\text{frost,surf}} = T_{\text{wall}} + \frac{\dot{q}_{\text{tot}}}{k_{\text{frost}}} \cdot x_{\text{frost}} + \frac{L_s \cdot \rho_{\text{air}} \cdot \omega_{\text{wall}} \cdot D_{\text{eff}}}{k_{\text{frost}}} \cdot \left(1 - \frac{\omega_{\text{frost,surf}}}{\omega_{\text{wall}}}\right) \tag{3.41}$$

with Ha being the Hatta number, representing the ratio between the characteristic times of diffusion and of desublimation defined by :

$$Ha = \cosh^{-1}\left(\frac{\omega_{\text{frost,surf}}}{\omega_{\text{wall}}}\right) \tag{3.42}$$

Knowing those quantities, the different heat fluxes (sensible, latent, total) can be deduced.

As demonstrated by Hermes et al. [34], the mass flux of frost growth can be determined by:

$$\frac{L_s \cdot b \cdot x_{\text{frost}}}{k_{\text{frost}}} \cdot \dot{m}_g^2 + \left(1 + \frac{b \cdot x_{\text{frost}} \dot{q}_{\text{tot}}}{k_{\text{frost}}}\right) \cdot \dot{m}_g - \frac{\dot{q}_{\text{lat}}}{L_s} = 0 \tag{3.43}$$

where b is the parameter from Eq.(3.22). The growth rate being computed, the frost thickness through time can be easily computed through this 1$^{\text{st}}$ order equation:

$$x_{\text{frost}}(t + \Delta t) = x_{\text{frost}}(t) + \Delta t \cdot \left.\frac{\dot{m}_g}{\rho_{\text{frost}}}\right|_t \tag{3.44}$$

Finally, the mass of frost layer can be expressed as :

$$m(t) = \int \dot{m} \cdot \mathrm{d}\tau \tag{3.45}$$

3.2.7 Segment heat transfer development : fin thermal conduction impact

The fin thermal conduction impact is a phenomenon due to the temperature difference of two tubes, linked by metallic fins. The temperature difference creates a potential, leading to conduction heat transfer in the set of fins

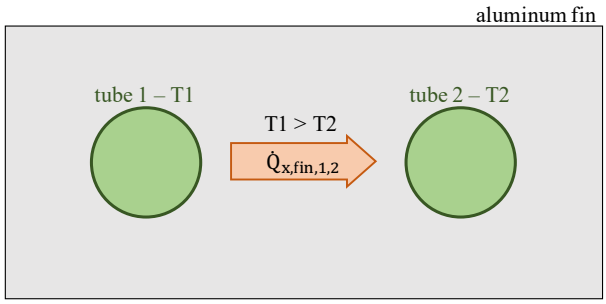

FIGURE 3.8: Cross fin thermal conduction illustration

Because it substantially increases the model complexity and computational cost [79], fin conductivity is not often taken into account, especially when frost events occur. However, in the frame of this thesis, the frost distribution is a key result and is tightly linked to the surface temperature. Fin thermal conductivity may have an impact on wall temperature when a tube with superheated refrigerant at around 15°C is very close by another tube where the refrigerant is at -7°C. A short preliminary study is conducted to quantify the actual impact of fin conductivity on the wall temperature distribution.

The idea is to implement a very simple code : fixed heat transfer coefficients, multiple rows but single tube in height, pressure drops not accounted, etc. The geometry of this simplefied exchanger is illustrated in Figure 3.9.

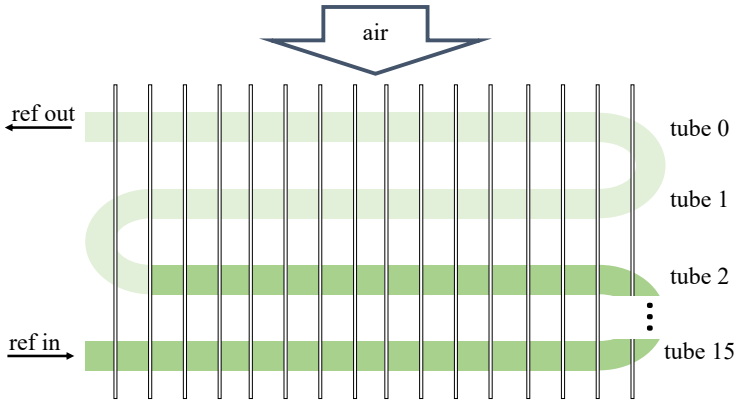

FIGURE 3.9: Schematic representation of the simplified heat exchanger

To this simple code, the heat conduction in fins is added and can be activated or not. This results in having approximate temperatures of both fluids (i.e. air and

refrigerant) and wall, if fin conduction is taken into account or not, as illustrated Figure 3.10.

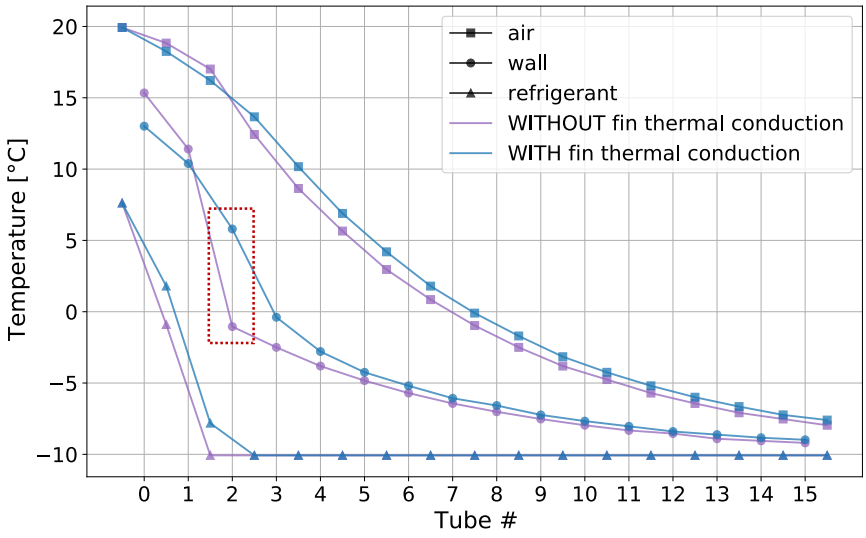

FIGURE 3.10: Air, wall and refrigerant temperatures with and without fin thermal conductivity, in a simplified heat exchanger

In Figure 3.10, the *Tube 0* corresponds to the air supply and refrigerant exhaust. The supply conditions are set for a classical heat pump evaporator situation, leading to a potential frost event.

Although fluids temperatures are very close, all the interest of the preliminary study is in the wall temperature. Indeed, at the *Tube 2*, if fin thermal conduction is not taken into account, the wall temperature is negative, leading to potential frost accumulation if the air dewpoint is above this temperature. On the opposite, if the fin thermal conductivity is accounted, the wall temperature at the same place is above 5°C, preventing any frost formation. Even though the predicted total thermal power transferred will be similar in both situations, it is now easily understandable that the frost distribution through the exchanger will differ.

Back in the actual evaporator, the implemented code to account for the fin thermal heat conduction is presented hereunder. First, it is worth recalling that the exchanger shows a staggered tube arrangement, as illustrated in Figure 3.11. A reasonable assumption made is to only consider thermal conduction from one tube to its direct neighbors. A tube in the pack has a maximum of six neighbors, and less if it is at the exchanger edge.

Based on the conduction equation, the heat transfer through fins between two tubes can be expressed as :

$$\dot{Q}_{\mathrm{x,fin,i,j}} = L_{\mathrm{fin,thick}} \cdot D_{\mathrm{ext}} \cdot N_{\mathrm{fin}} \cdot k_{\mathrm{fin}} \cdot \sum_{k=1}^{N} \frac{T_{\mathrm{wall,i,j}} - T_{\mathrm{wall,k}}}{d_k} \tag{3.46}$$

where N_{fin} is the number of fins, $T_{\mathrm{wall,k}}$ is the wall temperature of the k^{th} direct neighbor of the tube i, j and d_k the distance between those tubes.

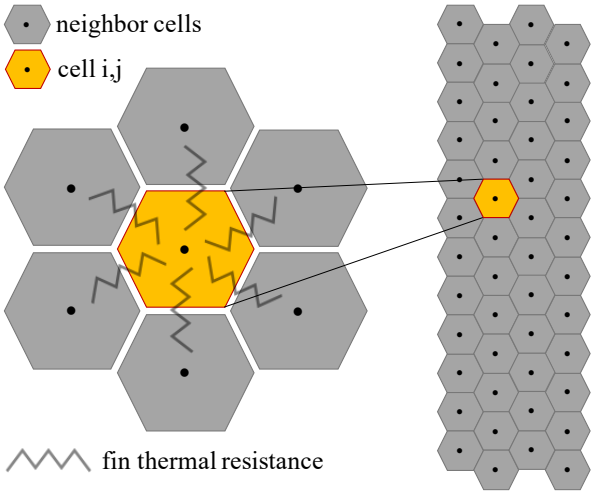

FIGURE 3.11: Exchanger staggered configuration (a black dot corresponds to a tube)

To solve those equations, all neighbors wall temperatures must be known in advance. Knowing that the resolution is sequential, considering a model in (quasi-)steady state would result in an additional set of $N-1$ additional iteration variables, leading to a poorly robust model. On the opposite, implementing a dynamic model with wall capacity allows to know the complete exchanger wall temperatures at a time t, without any additional iteration variable. This is possible because the forward Euler method is adopted, allowing to compute the temperatures of time $t+1$ at time t. From Eq.(3.1), the wall temperature of the cell i,j for the next time step is computed as:

$$T_{\text{wall,i,j,t+1}} = T_{\text{wall,i,j,t}} + \frac{dt}{m \cdot C} \cdot \left(\dot{Q}_{\text{ref,i,j,t}} - \dot{Q}_{\text{air,i,j,t}} - \dot{Q}_{\text{x,fin,i,j,t}} \right) \tag{3.47}$$

where dt corresponds to the time step.

3.2.8 Hydraulic performance

In this section, the hydraulic performance is investigated, and more especially the pressure drops and mass flowrates of refrigerant and air.

Refrigerant side

As described many time previously, the refrigerant total flowrate is split in three parallel circuits. Based on experimental observations Section 2.2.3, for the simulations, the flowrate ratio of each circuit is simply imposed to the model as an input.

For the pressure drops, to simplify the algorithm resolution, it has been decided to decouple the thermal and hydraulic performance. It allows to avoid an additional iteration loop on the complete algorithm, severely penalizing the computational speed.

The pressure drops should be tightly related to the heat transfer performance because they are related to the tube length and flow conditions [20]. It can be seen [84] that for horizontal tubes, the heat transfer coefficient and friction factor have the same trend, regarding the refrigerant quality. Based on this idea, the pressure at a

position i is expressed by:

$$P_{\text{ref,i}} = P_{\text{ref,su}} - \frac{h_{\text{ref,i}} - h_{\text{ref,su}}}{h_{\text{ref,ex}} - h_{\text{ref,su}}} \cdot \Delta P_{\text{ref,tot}} \tag{3.48}$$

This expression supposes that $h_{\text{ref,ex}}$ and $\Delta P_{\text{ref,tot}}$ are known. The total exchanger pressure drop is computed based on an empirical correlation, only dependent on the refrigerant mass flowrate:

$$\Delta P_{\text{ref,tot}} = P_{\text{ref,su}} - P_{\text{ref,ex}} = K \cdot \dot{M}_{\text{ref}}^{B} \tag{3.49}$$

where K and B are coefficient that are tuned, based on an optimization algorithm. In his algorithm, Dickes [20] iterates on the total heat transfer, allowing to deduce the exhaust specific enthalpy directly and explicitly, which is not the case here. However, a sensibility study has been realized to show the impact of the error of ΔP on the specific enthalpy and temperature at the exhaust, due to a bad approximation of the superheated degree. In normal conditions, a superheated zone must be met, with a superdegree between 0 and 30K.

The hypothetical superheat degree is set to 15 K (close to what is observed in experimental condition). Using Eq.(3.48) to the specific enthalpy can be computed. Then, the error on the specific enthalpy is computed, varying the superheat degree for the exhaust enthalpy approximation of Eq.(3.48). The error on the enthalpy is taken at the exhaust to get the worst case scenario, because errors through the exchanger accumulates. The same is made on the saturation temperature at the vapor saturation point.

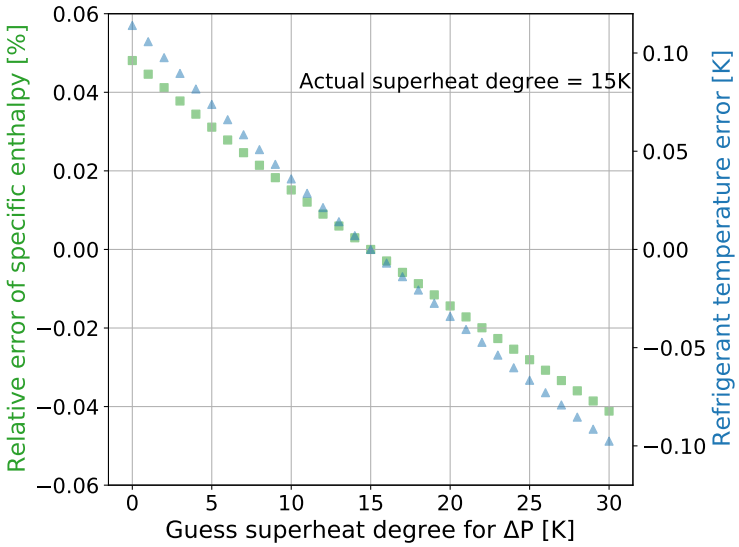

FIGURE 3.12: Error on specific enthalpy and saturation temperature regarding the error on the superheat degree deviation

Figure 3.12 shows that even if the superheat degree has an approximation error of 30K for the computation of the exhaust specific enthalpy for the pressure drop computation using Eq.(3.48), the impact is :

- under 0.1 % error in the exhaust specific enthalpy
- under 0.2 K error for the refrigerant saturation temperature.

Even though the method presented by Dickes is already based on a simplification and that an additional approximation is added, the balance between the good predicted results, the easiness of implementation, the algorithm efficiency and point of detail targeted on the refrigerant side, the method is kept and used in the model.

Air pressure drops

On the air side, the mass flowrate and pressure drops are computed for each tube individually. Initially, the mass flowrate is evenly distributed. However, if frost grows on some tubes and not on others and the mass flowrate distribution is kept constant, the local pressure drops will differ. Therefore, the mass flowrate is proportionally adjusted in a way to obtain the same pressure drops at each tube on the exchanger height for a given row. Dynamic effects certainly occur within the exchanger with inter-row impact on mass flow-rate in the depth of the exchanger (i.e. frost on the exhaust tube impacts flowrate on previous tubes). To account for this, CFD study should be carried on, but would be out of scope in the frame of this thesis. Based on measurement Section 2.2.2 showing that the air speeds up and downstream are different, the choice of computing the mass flowrate independently for each row in depth is kept, imposing the total mass conservation constraint.

The local pressure drops are computed using Mastrullo et al. [58] equation :

$$\Delta P_{\text{air,i,j}} = \frac{G^2_{\text{air,i,j}}}{2 \cdot \rho_{\text{air}}} \cdot f \cdot \frac{A_{\text{air,i,j}}}{A_{\text{CS,i,j}}} \tag{3.50}$$

where G is the mass flux, f is the friction factor, $A_{\text{air,i,j}}$ the exchange surface and $A_{\text{CS,i,j}}$ the cross section area. The friction factor is evaluated with Wang et al. [91] correlation :

$$f = 0.0267 \cdot Re^{\psi_1} \cdot \left(\frac{P_t}{P_r}\right)^{\psi_2} \cdot \left(\frac{P_{\text{fin}}}{D_{\text{col}}}\right)^{\psi_3} \tag{3.51}$$

with P_t, P_r and P_{fin} being respectively the tube, the row and the fin pinch, D_{col} the collar diameter and ψ_i some coefficient defined by :

$$\psi_1 = -0.764 + 0.739 \cdot \frac{P_t}{P_r} + 0.177 \cdot \frac{P_{\text{fin}}}{D_{\text{col}}} - \frac{0.00758}{N_{\text{row}}} \tag{3.52}$$

$$\psi_2 = -15.689 + \frac{64.021}{\log(Re)} \tag{3.53}$$

$$\psi_3 = 1.696 - \frac{15.695}{\log(Re)} \tag{3.54}$$

Based on this, the exchanger pressure drop on the air side is simply expressed as :

$$\Delta P_{\text{air,HEX}} = \sum_{j=1}^{N_{\text{row}}} \Delta P_{\text{air,0,j}} \tag{3.55}$$

The index i is arbitrarily set to 0 because the pressure drop is the same on the height of the exchanger.

3.3 Frost surface modeling

The goal of the present thesis is to build a bridge between the macroscopic world of the heat exchangers and the surface level. The physical phenomena involved in the heat exchanger have been described in the previous section. This section aims at describing the physics at the lower scale and how it is implemented in a numeric scheme. Then, in the next chapter, both scales will be merged.

The frost growth period has already been described. This process does not depend (or at least depends much less) on the surface physics, as the interactions between the air and the surface are decreased because of a nuclei layer grown during the nucleation phase. This section focuses on the early stage of frost formation, namely on nucleation process.

3.3.1 Thermodynamics of nucleation

It is widely known that every system tends to minimize its energy. A vapor bulk is considered as the parent phase (i.e. liquid is the daughter phase), being at a given pressure and temperature (P,T). Now, if this bulk is cooled down in an isobaric way at a temperature T^v, under the vapor saturation temperature $T_{\text{sat,v}}$, it has a chemical potential $\mu^v(P, T^v)$. However, the potential of the liquid phase in the same conditions $\mu^l(P, T^v)$ is smaller [40], such as:

$$\Delta\mu = \mu^v(P, T^v) - \mu^l(P, T^v) > 0 \tag{3.56}$$

The situation is then thermodynamically favorable for a transformation with $\Delta\mu$ as the driving force. However, the vapor system can be in a metastable state, corresponding to a local minimum of free energy[1] as illustrated in Figure 3.13.

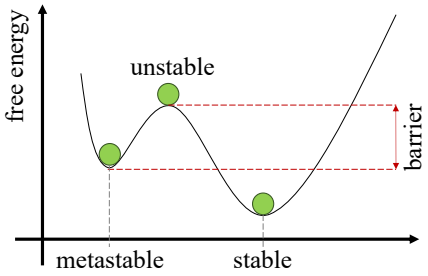

FIGURE 3.13: Illustration of metastable state

By definition, the saturation pressure of vapor (at a given temperature) corresponds to the thermodynamic equilibrium between the vapor and the condensates/frost. However, condensation or desublimation processes often need vapor pressures exceeding the saturation pressure because the nucleation process corresponds to a new interface creation, implying an energy cost [65]. The driving force (here supersaturation) needs to overcome a minimum energy, consumed in forming the new interface. Once this point is reached, an embryo can grow.

This phenomenon can be represented in a psychrometric diagram (Figure 3.14).

[1]Free energy : state function corresponding to the maximum work a thermodynamic system can perform at constant temperature. It indicates if the process is thermodynamically favorable or forbidden [96]

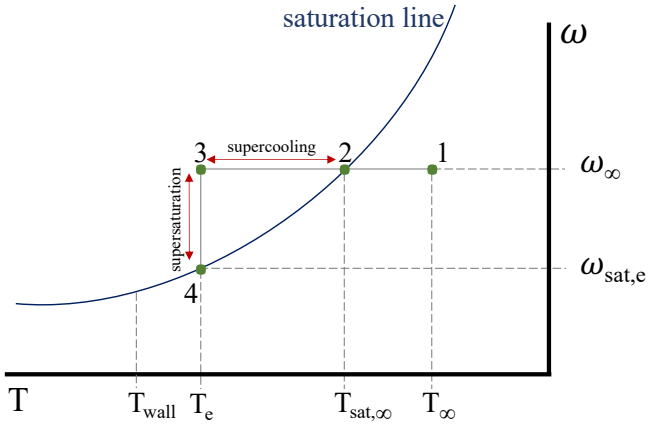

FIGURE 3.14: Psychrometric diagram of nucleation process in metastable state

The different steps are presented by Piuccio et al. [69] and recalled here:

1. Point 1 corresponds to the humid air (not saturated) of the flux;
2. The air flux is submitted to a cold plate at T_{wall}. In the thermal boundary layer, this air is cooled down up to the water vapor saturation at point 2, corresponding to the dew-point;
3. Because of the free energy barrier necessary to create the new droplet interface, an additional cool down to the point 3 is necessary. The energy barrier quantification is detailed later in this chapter. The temperature T_{e} corresponding to this point is the temperature of the liquid/frost embryo.
4. When this point is reached, nucleation is launched. The phase change is represented by the transition from point 3 to 4.

Nucleation can either be qualified as homogeneous or heterogeneous. The first one corresponds to a situation where the probability of nucleation is homogeneous through the system. It means that there is no other phase in the system, suche as a surface, dust, etc. The second one corresponds to a case where the probability of nucleation is much higher in a given zone (e.g. because of a foreign body) [53]. The present study mainly focuses on the heterogeneous, the plate or the exchanger surface being the foreign body.

3.3.2 Homogeneous nucleation

Homogeneous nucleation corresponds to the spontaneous formation of a droplet, without any nucleating site, such as a surface or a dust particle (oppositely to heterogeneous nucleation, detailed later). When a water drop forms from air humidity, two sources contribute to energy variation of the system : a negative term, because supersaturated vapor transforms into liquid or ice [65] ; a positive term, related to the creation of new interfaces (liquid/vapor and/or liquid/solid) [26]. The change of the total Gibbs energy for a droplet creation is therefore expressed as [51]:

$$\Delta G = \frac{4\pi \cdot r^3}{3} \cdot \Delta g_v + 4\pi \cdot r^2 \cdot \sigma_{LV} \tag{3.57}$$

where Δg_v is the change of volume energy per unit volume of the water drop caused by its phase change (negative) and σ the surface energy. The index L is used for the following developments and stands for *liquid*. However, the droplet may be liquid or frozen water depending if vapor condensates or desublimates. The radius r corresponds to the droplet radius.

The term corresponding to the volume is proportional to r^3 while the surface contribution is proportional to r^2. It means that considering very small r, the positive surface term will dominate the negative volume term, leading to a positive ΔG. As the system always tends to minimize its free energy, this situation is not favorable to droplet creation (i.e. nucleation). Increasing the droplet radius will lead to an increase of ΔG, until reaching a maximum. Indeed, for sufficiently large radius, the cubic term will overpass the square one. After this maximum, increasing r will lead to a decrease of ΔG. Then, increasing the radius is here translated in a decrease of ΔG. In this situation, droplet creation tends to decrease the system free energy. Nucleation is then likely to happen. The evolution of the Gibbs free energy as well as the volume and surface contributions are represented in Figure 3.15.

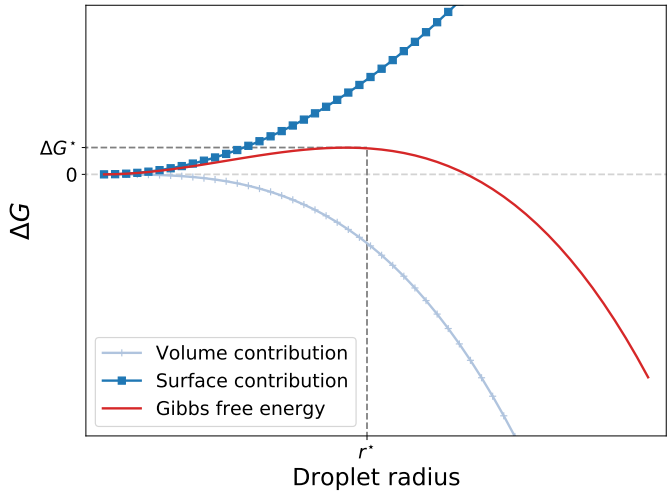

FIGURE 3.15: Evolution of energy barrier, regarding the droplet radius

It is possible to find the droplet radius corresponding to the maximum of ΔG, by differentiating Eq.(3.57) in respect to r:

$$r^\star = \frac{-2 \cdot \sigma_{LV}}{\Delta g_v} \tag{3.58}$$

$r^\star$ is called the critical radius. If the droplet radius is smaller than $r^\star$ ($r < r^\star$), the system can lower its energy by dissolving the nucleus. The droplet will disappear and the nucleation process will not occur. Now, if the droplet radius is larger than $r^\star$ ($r > r^\star$) , the system free energy decreases if the droplet grows. The system is then in a state inclined to enter in a nucleation process [51].

Going back to the psychrometric chart in Figure 3.14, it means that the more supersaturated the air, the more prone the system to produce large droplets. In other words, if the air is sufficiently saturated, it can overcome the critical energy barrier

and launch nucleation. This critical energy barrier $\Delta G^{\star}$ can be deduced substituting Eq.(3.58) into Eq.(3.57):

$$\Delta G^{\star} = \frac{16\pi}{3} \cdot \frac{\sigma_{LV}^3}{\Delta g_v^2} \tag{3.59}$$

Using some thermodynamic relations, Δg_v can be determined. From the definition of the Gibbs free energy, its differentiation can be written :

$$\mathrm{d}G = \mathrm{d}U + P \cdot \mathrm{d}V + V \cdot \mathrm{d}P - T \cdot \mathrm{d}S - S \cdot \mathrm{d}T \tag{3.60}$$

As the process of condensation or desublimation is isothermal and by definition of internal energy U ($\mathrm{d}U = T \cdot \mathrm{d}S - P \cdot \mathrm{d}V$), Eq.(3.60) can be simplified as:

$$\mathrm{d}G = V \cdot \mathrm{d}P \tag{3.61}$$

Using the perfect gas law and integrating this expression between the ambient partial pressure of vapor p_{∞} and the saturation vapor at the embryo temperature $p_{\mathrm{sat,e}}$, the following equation can be written as:

$$\Delta g_v = \frac{\rho_e \cdot R \cdot T_e}{MM_w} \int_{p_{\infty}}^{p_{\mathrm{sat,e}}} \frac{\mathrm{d}P}{P} = -\frac{\rho_e \cdot R \cdot T_e}{MM_w} \cdot \ln\left(\frac{p_{\infty}}{p_{\mathrm{sat,e}}}\right) \tag{3.62}$$

where ρ_e and T_e are the density and temperature of the embryo while R and MM_w are the ideal gas constant and molar mass of water, respectively. Combining Eq.(3.59) and Eq.(3.62), the critical Gibbs energy barrier can be written as:

$$\Delta G_{\mathrm{hom}}^{\star} = \frac{16\pi}{3} \cdot \frac{\sigma_{LV}^3}{\left[\frac{\rho_e \cdot R \cdot T_e}{MM_w} \cdot \ln\left(\frac{p_{\infty}}{p_{\mathrm{sat,e}}}\right)\right]^2} \tag{3.63}$$

3.3.3 Heterogeneous nucleation

Heterogeneous nucleation corresponds to the nucleation on a foreign substrate brought to the system. In the present description, this body is a cold plane surface.

The description of this type of nucleation is based on the homogeneous description. However, the nucleation process will depend on the surface characteristics such as wettability and roughness.

In a first stage, the surface is considered as perfectly smooth (i.e. no roughness). It allows to study the impact on the chemistry of the surface and thus, its affinity with water.

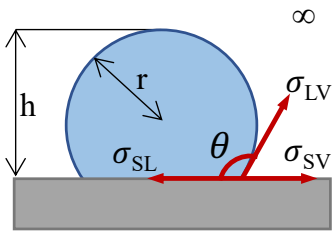

FIGURE 3.16: Nomenclature of embryo geometry

The energy needed to nucleate on a flat surface is the sum of a negative contribution due to the droplet condensation or desublimation and a positive one due to the creation of interface between the nuclei and the surface and the nuclei and the surroundings [26] :

$$\Delta G = V \cdot \Delta g_v + A_{\mathrm{LV}} \cdot \sigma_{\mathrm{LV}} + A_{\mathrm{SL}} \cdot (\sigma_{\mathrm{SL}} - \sigma_{\mathrm{SV}}) \tag{3.64}$$

where V is the nuclei volume and $A_{i,j}$ the surfaces of the different interfaces. Remembering geometry rules and based on the nomenclature of Figure 3.16, those quantities can be expressed as:

$$V = \frac{\pi \cdot h^2 \cdot (3r - h)}{3} \tag{3.65}$$

$$A_{\mathrm{LV}} = 2\pi \cdot r \cdot h \tag{3.66}$$

$$A_{\mathrm{SL}} = \pi \cdot r^2 \cdot \sin^2(\theta) \tag{3.67}$$

$$h = r \cdot (1 - \cos(\theta)) \tag{3.68}$$

Then, Eq.(3.64) becomes :

$$\Delta G = \frac{\pi \cdot r^3}{3} \cdot (1-\cos\theta)^2 \cdot (2+\cos\theta) \cdot \Delta g_v + 2\pi \cdot r^2 \cdot (1-\cos\theta) \cdot \sigma_{\mathrm{LV}} + \pi \cdot r^2 \cdot \sin^2(\theta) \cdot (\sigma_{\mathrm{SL}} - \sigma_{\mathrm{SV}}) \tag{3.69}$$

After different trigonometrical manipulations and remembering Young equilibrium relation Eq.(1.1), this relation is reduced to:

$$\Delta G = \left[\frac{\pi \cdot r^3}{3} \cdot \Delta g_v + \sigma_{\mathrm{LV}} \cdot \pi \cdot r^2 \right] \cdot (1 - \cos\theta)^2 \cdot (2 + \cos\theta) \tag{3.70}$$

The same procedure as for homogeneous nucleation is followed to find the critical radius and thus the critical energy barrier by solving $\partial \Delta G / \partial r = 0$:

$$r^\star = \frac{-2 \cdot \sigma_{LV}}{\Delta g_v} \tag{3.71}$$

Then, using the definition of Δg_v Eq.(3.62), the critical energy barrier for heterogeneous nucleation is written as:

$$\Delta G^\star_{\mathrm{het}} = \frac{16\pi}{3} \cdot \frac{\sigma_{LV}^3}{\left[\frac{\rho_e \cdot R \cdot T_e}{M M_w} \cdot \ln\left(\frac{p_\infty}{p_{\mathrm{sat,e}}} \right) \right]^2} \cdot \frac{(1 - \cos\theta)^2 \cdot (2 + \cos\theta)}{4} \tag{3.72}$$

Defining the function $\Omega(\theta)$:

$$\Omega(\theta) = \frac{(1 - \cos\theta)^2 \cdot (2 + \cos\theta)}{4} \tag{3.73}$$

it is worth noting that $\Delta G^\star_{\mathrm{het}}$ can be expressed as:

$$\Delta G^\star_{\mathrm{het}} = \Delta G^\star_{\mathrm{hom}} \cdot \Omega(\theta) \tag{3.74}$$

The shape of $\Omega(\theta)$ is plotted in Figure 3.17.

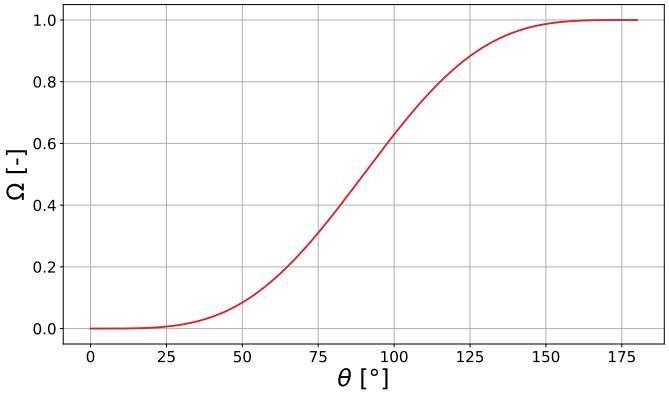

FIGURE 3.17: Plot of $\Omega(\theta)$

This curve shows the impact of the surface contact angle on the nucleation. If the surface is hydrophilic (small θ), Ω is small. It means that the energy barrier to initiate the nucleation will be low. The supersaturation degree does not need to be very important before observing the first liquid or ice embryo on the surface. Oppositely, higher contact angles will imply high energy barrier to reach to nucleate. The necessary supersaturation level is then higher and odds of nucleation are smaller.

Beker and Döring [7] proposed a law to determine the nucleation rate :

$$I = I_0 \cdot \exp\left(\frac{-\Delta G}{k \cdot T_{\text{wall}}}\right) \tag{3.75}$$

where k is the Boltzmann constant and I_0 the kinetic constant of the process. Sanders [76] set this value to $10^{29}\text{m}^{-2}\text{s}^{-1}$. However, Nath and Boreyko [65] stipulate that this value may be uncertain. In the present situation, the impact of the value of this constant is studied.

Volmer [90] empirically determined that for homogeneous nucleation, a minimum $I^\star$ of $\ln(10)$ embryos/m^2/s (≈ 2.2 embryos/cm^2/s) is necessary. It is widely considered [22, 38, 64, 65, 69] that this order of magnitude can be kept for heterogeneous nucleation. Therefore, the following relation is written:

$$I^\star = I_0 \cdot \exp\left(\frac{-\Delta G^\star}{k \cdot T_{\text{wall}}}\right) = 2.2 \cdot 10^4 [\text{embryos/m}^2\text{/s}] \tag{3.76}$$

Very practically, combining Eq.(3.72) and Eq.(3.76) allows to determine the minimal partial vapor pressure necessary in the air to launch nucleation. With the combination of those equations, it is possible, for given conditions, to determine the supersaturation degree (SSD) and the level of supercooling (ΔT_{SC}) at the critical point. They are both defined as:

$$SSD = \frac{P_\infty - P_{\text{sat,e}}}{P_\infty} \tag{3.77}$$

$$\Delta T_{\text{SC}} = T_{\text{sat},\infty} - T_e \tag{3.78}$$

The variation of those indicators are studied, regarding the surface temperature, the nature of nuclei (liquid or frozen) and the impact of the constant I_0.

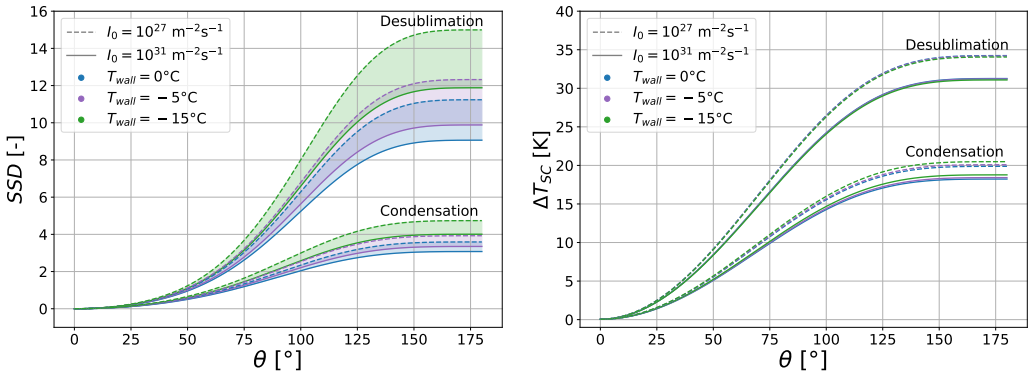

FIGURE 3.18: Variation of SSD and ΔT_{SC} regarding the contact angle θ, the wall temperature T_{wall} and the kinetic constant I_0

Many pieces of information can be extracted for Figure 3.18. First, as expected, SSD and ΔT_{SC} increase with the contact angle because of the impact of Ω. Indeed, the more hydrophobic, the harder to condensate/desublimate. Then, it is clear that less energy is required to condensate compared to desublimation. So, it will be more likely to meet conditions driving to condensation followed by potential freezing of the droplets rather than desublimation. Another conclusion extracted from those figures is the impact of the kinetic constant I_0. For very hydrophilic surfaces (i.e. $\theta < 75°$), its impact is minimal. However, for hydrophobic surfaces it is not the case anymore. Large variations are observed with difference up to 20% for the SSD and supercooling of 3K for a change of 4 orders of magnitude of I_0 (magnitude variation found in the literature). As this constant value is not clearly fixed and represents a source of uncertainty, in the present thesis, it has been decided to consider it as a tuning parameter of the model.

3.3.4 Roughness influence

Looking to Figure 3.18, a regular neutral surface showing a contact angle of about 90° needs a minimum supercooling above 10 K to launch condensation. However, this is not what is observed in practice. The assumption considered up to here is that the surface is perfectly smooth (i.e. no roughness). However, in reality, this is not the case. Roughness can bring nucleation sites, enhancing condensation or frost. The impact of this parameter is detailed here.

The assumption made for the following developments is that the roughness has a spherical shape of radius R_r. This roughness shape can either be convex or concave as illustrated in Figure 3.19 left and right, respectively.

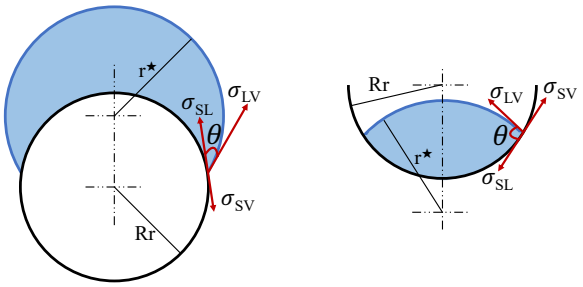

FIGURE 3.19: Schematic representation of roughness : convex (left) and concave (right)

A convenient way to account for the roughness in the modeling, is to increase complexity of the Ω. It does not only depend on the apparent contact angle θ anymore but also on the critical droplet radius $r^\star$ and on the roughness characteristic radius R_r [51]. Fletcher [25] developed an expression of the Ω function for the roughness of convex shape. Defining :

$$x = \frac{R_r}{r^\star} \tag{3.79}$$

$$m = \cos\theta \tag{3.80}$$

$$g_{cx} = \sqrt{1 + x^2 - 2m \cdot x} \tag{3.81}$$

$$g_{cv} = \sqrt{1 + x^2 + 2m \cdot x} \tag{3.82}$$

the function Ω is now expressed as:

$$\Omega_{cx}(\theta, r^\star, R_r) = \frac{1}{2}\left[1 + \left(\frac{1 - m \cdot x}{g_{cx}}\right)^3 + x^3 \cdot \left(2 - 3 \cdot \frac{x - m}{g_{cx}} + \left(\frac{x - m}{g_{cx}}\right)^3\right) + 3m \cdot x^2 \cdot \left(\frac{x - m}{g_{cx}} - 1\right)\right] \tag{3.83}$$

In the same way, Mahata [57] derived the same kind of expression, for a concave type of roughness:

$$\Omega_{cv}(\theta, r^\star, R_r) = \frac{1}{2}\left[1 - \left(\frac{1 + m \cdot x}{g_{cv}}\right)^3 - x^3 \cdot \left(2 - 3 \cdot \frac{x + m}{g_{cv}} + \left(\frac{x + m}{g_{cv}}\right)^3\right) + 3m \cdot x^2 \cdot \left(\frac{x + m}{g_{cv}} - 1\right)\right] \tag{3.84}$$

In both convex and concave situations, considering $\lim_{x \to +\infty}(\Omega)$, tends to the plane configuration (i.e. perfectly smooth surface), which is an expected result. On the other side, a convex roughness radius tending to 0 would correspond to the homogeneous situation (i.e. nucleating on an infinitely small particle). Those trends are sucessfully illustrated in Figure 3.20. It is to note that a concave roughness radius tending to 0 is physically inconsistent.

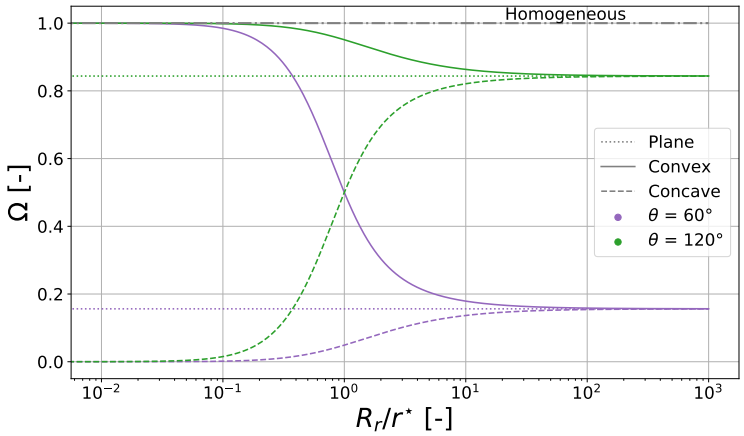

FIGURE 3.20: Variation of $\Omega(\theta, r^\star, R_r)$ regarding the roughness, the roughness type and the contact angle

The Ω function being redefined, it is possible to analyze its impact on the SSD and ΔT_{SC} in Figure 3.21.

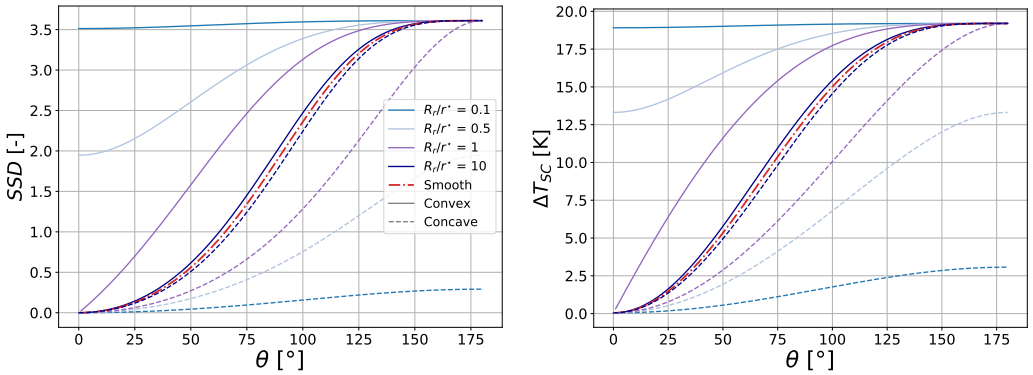

FIGURE 3.21: Variation of SSD and ΔT_{SC} regarding the contact angle and relative roughness. $I_0 = 10^{29}$ $\mathrm{m}^{-2}\mathrm{s}^{-1}$ and $T_{\mathrm{wall}} = -5°\mathrm{C}$

Figure 3.21 explicitly shows the impact of the roughness on the nucleation process. A spherically convex roughness tends to increase the energy barrier to launch nucleation process and then give hydrophobic properties to the surface, even for small static contact angles. Oppositely, a concave roughness shape ease the nucleation process. For standard surfaces, it explains why the SSD and ΔT_{SC} are not so important before showing the first nuclei.

Another aspect shown is the importance of the relative roughness size. Indeed, for a given critical nuclei size, the smaller the roughness characteristic radius, the more pronounced the effect. Being able to control the roughness on a surface can give to it very specific properties.

Because of the random nature of the surfaces considered, this radius ratio is also taken as an empirical tuning parameter in the present model.

3.3.5 Nuclei temperature

Another phenomenon experimentally observed in the test campaigns is that for given conditions, nucleation may occur, but the droplets freeze or stay liquid depending on the type of surface. This difference is explained because of the inherent shape of the droplet, function of the wettability of the substrate.

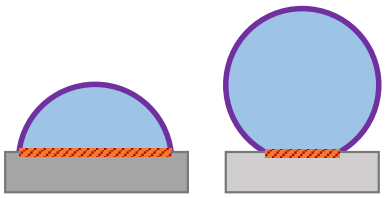

FIGURE 3.22: Exchange surface between the nuclei and the ambiant air (purple) and between the nuclei and the cold surface (red/orange) for different contact angles

In the light of Figure 3.22, it is obvious that for the same conditions, the two different droplets will not be at the same temperature. Indeed, it is much easier for

a droplet to exchange heat with the surface when lying on hydrophilic surface (left). Furthermore, in the case of hydrophilic surface, the surface area of the droplet shell is smaller, decreasing the heat transfer rate with the ambient air. The exact opposite conclusion may be drown for hydrophobic surface (right). So, a droplet on a hydrophilic substrate is more likely to freeze compared to the same droplet on hydrophobic surface.

Many authors (list not exhaustive) developed complex numerical model to deduce the droplet temperature and freezing scheme [3, 24, 59, 88]. However, it is not relevant in the frame of this thesis to develop complex model for this prediction, to keep a descent computational time. What is decided is then to apply a heat balance over the given droplet, depending on the conditions and apparent contact angle.

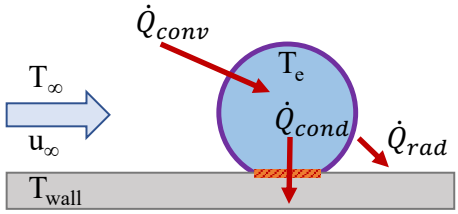

FIGURE 3.23: Schematic representation of the different heat transfer process on a given droplet

An important assumption made is that the droplet is at a uniform temperature. It is justified because the Biot dimensionless number ($Bi = \frac{h \cdot L}{k}$) is much smaller than 0.1. The transient energy balance on the droplet can be written as :

$$m_e \cdot c_e \cdot \frac{\mathrm{d}T_e}{\mathrm{d}t} = \dot{Q}_{\mathrm{conv}} - \dot{Q}_{\mathrm{cond}} - \dot{Q}_{\mathrm{rad}} \tag{3.85}$$

where m_e and c_e are the mass and the specific heat capacity of the embryo, respectively. The subscripts *conv*, *cond* and *rad* stand for convection, conduction and radiation, respectively. The transient approach is envisaged here only for numerical robustness reasons. The dynamic is not accounted in the physics in this model. Only the temperature of the droplet when the thermal equilibrium is reached ($T_{e,eq}$) matters here.

It can be shown that the contribution of the radiation heat transfer is negligible compared to convection and conduction. Only the latter are considered here. Remembering Eq.(3.65) and Eq.(3.68) there is:

$$\dot{Q}_{\mathrm{conv}} = A_{\mathrm{LV}} \cdot h_{\mathrm{conv}} \cdot (T_\infty - T_e) \tag{3.86}$$

with $h_{\mathrm{conv}} = \mathrm{f}(Nu)$ and Nu expressed as [9] :

$$Nu = 2 + 0.6 \cdot Re^{1/2} \cdot Pr^{1/3} \tag{3.87}$$

The heat transfer rate in conduction is defined as:

$$\dot{Q}_{\mathrm{cond}} = \frac{A_{\mathrm{SL}} \cdot k_w}{L_{\mathrm{cond}}} \cdot (T_e - T_{\mathrm{wall}}) \tag{3.88}$$

where k_w is the thermal conductivity of water and L_{cond} is the average distance between the surface and the droplet.

Because A_{LV} and A_{SL} depends on the contact angle, these quantities depends on the shape of the droplet. Numerically solving Eq.(3.85) allows to determine the temperature of the droplet. If the conditions to launch nucleation are met and assuming that this process is fast, the criteria to determine if the droplet freezes or stays liquid is very simple. If, at the equilibrium, $T_{e,eq}$ is above 0°C it will be liquid. Otherwise, it is ice nucleation. This is illustrated in the example of Figure 3.24.

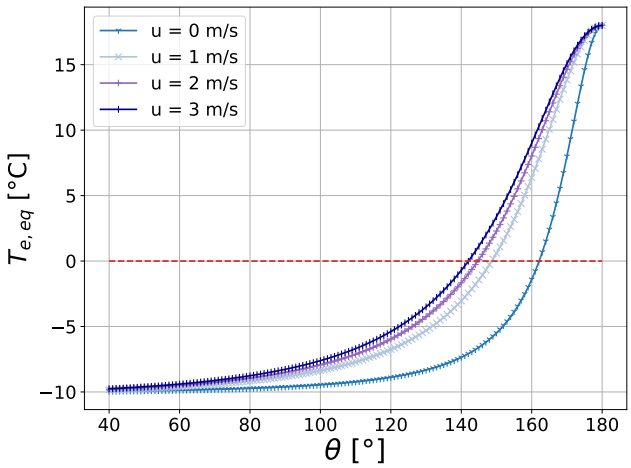

FIGURE 3.24: Temperature of a droplet with a characteristic diameter of 1 mm on a -10°C plate submitted to a air flux at 18°C for different air speeds and surface contact angles

It can be seen that if the surface is sufficiently hydrophobic, even on a plate showing temperatures below 0°C, the droplet may not freeze. Obviously, this phenomenon is accentuated for higher air speeds.

3.3.6 Droplet sliding

From what has been developed previously, one implicit assumption may be challenged. It is supposed that the droplet has the time to reach the thermal equilibrium. On an horizontal plate, even if at high air speeds the drop may be unpinned before freezing, it is not a big issue. However, on a tilted plate (HEX fins are vertical), if the time needed for the droplet to freeze is too long, the droplet may roll before cooling down. Xie et al. [100] proposed a theoretical development to obtain an explicit criterion allowing to determine if a droplet of a given radius will stick, slide or roll, depending on the type of surface and its tilt angle. It is based on three dimensionless numbers, namely the Bond number (Bn), Weber number (We) and Ohnesorge number (Oh) .

The Bond number represents the importance of gravitational forces compared to surface tension forces:

$$Bn = \frac{(\rho_{\mathrm{w}} - \rho_{\mathrm{air}}) \cdot g \cdot r^2}{\sigma_{\mathrm{LV}}} \tag{3.89}$$

The Weber number expresses relative importance of the fluid's inertia compared to its surface tension:

$$We = \frac{\rho_{\mathrm{air}} \cdot r \cdot \bar{u}_e^2}{\sigma_{\mathrm{LV}}} \tag{3.90}$$

where $\bar{u}_e$ is the average speed of the droplet. Finally, the Ohnesorge number relates the viscous forces to inertial and surface tension forces:

$$Oh = \frac{\mu_{\text{air}}}{\sqrt{\rho_{\text{air}} \cdot \sigma_{\text{LV}} \cdot r}} = \frac{\sqrt{We}}{Re} \tag{3.91}$$

where μ_a is the air dynamic viscosity. Remembering that θ, θ_a and θ_r are the static, advancing and receding contact angles, respectively, they obtain the following size of critical radius before sliding or rolling, respectively [21, 23, 100]

$$r_{\text{max,sliding}} = \sqrt{\frac{12}{\pi^2} \cdot \frac{\sin\theta \cdot (\cos\theta_r - \cos\theta_a)}{2 - 3\cos\theta + \cos^3\theta} \cdot \frac{\sigma_{\text{LV}}}{(\rho_{\text{w}} - \rho_{\text{air}}) \cdot g \cdot \sin\alpha}} \tag{3.92}$$

$$r_{\text{max,rolling}} = \sqrt{\frac{24}{\pi} \cdot \frac{(1 + \cos\theta) \cdot (\cos\theta_r - \cos\theta_a)}{3 - 5\cos\theta + \cos^2\theta + \cos^3\theta} \cdot \frac{\sigma_{\text{LV}}}{(\rho_{\text{w}} - \rho_{\text{air}}) \cdot g \cdot \sin\alpha}} \tag{3.93}$$

It is worth noting that in the frame of this thesis, the difference between the rolling and sliding movements has no capital interest. The ultimate goal is to predict if the liquid droplet will stay (and possibly freeze) or leave.

The critical radius regarding the tilt angle ($\alpha = 0° =$ horizontal and $\alpha = 90° =$ vertical) is represented in Figure 3.25 for three different surfaces : the aluminum reference surface, the commercial superydrophobic coating tested (HIREC) and fictitious superhydrophobic coating ($\theta = 170°$).

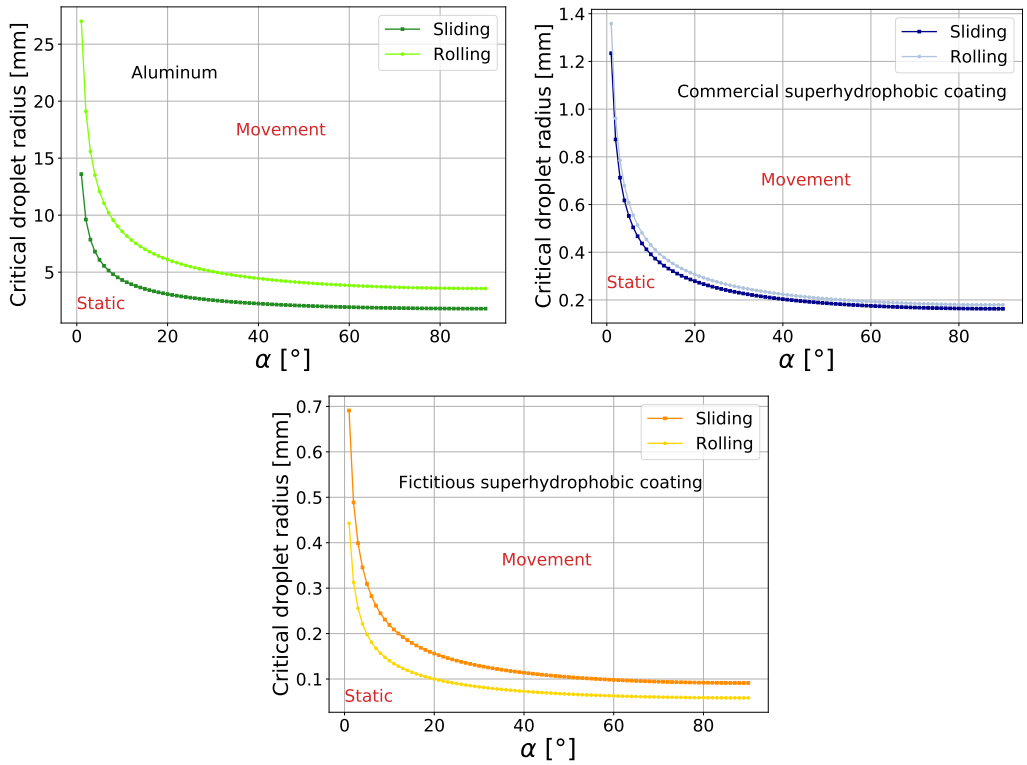

FIGURE 3.25: Critical droplet size before movement initiation for different tilt angles and surfaces

The first detail to note in Figure 3.25 is the y-scale of the different graphs which are very different. Then, obviously, the more the tilt angle increases, the smaller the critical radius for movement initiation. Both rolling and sliding types of movement are represented. However, for the aluminum and the commercial superhydrophobic coating, the sliding movement needs smaller droplet radius for movement launch. Consequently, no rolling movement will be observed for those materials. This is why a third graph is plotted, representing behavior for a fictitious material even more hydrophobic. It is seen that in that case, the movement will be rolling and not sliding. In practice, for a vertical plate ($\alpha = 90°$), gravitational effect predominates the viscous and surface tension forces for droplet with a radius above 1.7 mm fir a classical aluminum plate while 0.15 mm for the superhydrophobic material.

A phenomenon in nucleation theory is the droplet coalescence [15]. However, it is not accounted in this thesis, for the sake of simplicity. This assumption is translated in an overestimation of frost formation. Indeed, if different droplets join to each other, their size will increase and the probability to slide or roll increases too, decreasing the odds to frost. Nevertheless, as the ultimate goal is to describe frost formation in a complete exchanger, the description of this phenomena would bring too much complexity to nucleation models.

3.3.7 Nucleation simulation scheme

For the simulation of nucleation on the different surfaces showing negative temperatures, the numerical decisional scheme is the one illustrated in Figure 3.26.

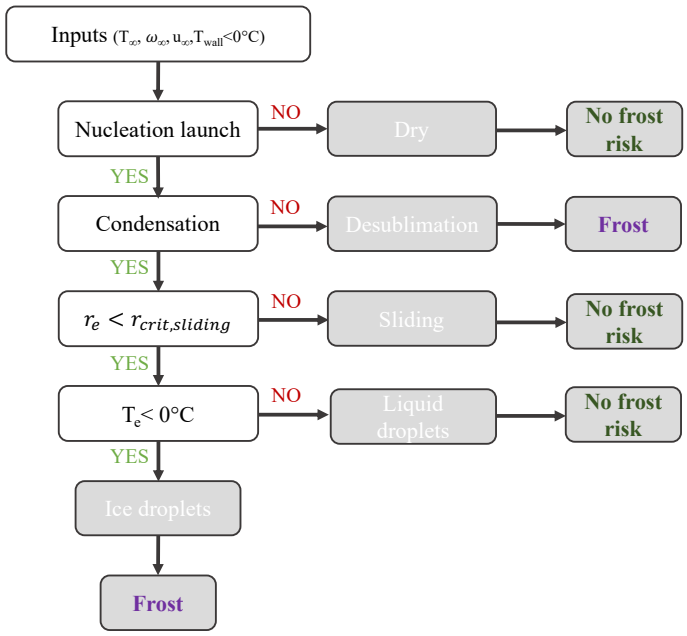

FIGURE 3.26: Numerical decisional tree for nucleation simulation

3.4 Summary and conclusions

The aim of this chapter was to present the modeling tools developed either for the global heat exchanger or for the nucleation process on specific surfaces.

The model envisaged for the evaporator was a dynamic tube-by-tube model. The dynamic character of the tool allowed to decouple the refrigerant and air side phenomena by the means of the exclusive interaction of the fluids with the separating wall. On the refrigerant side, for one given tube, the fluid could either be in two-phase, in pure vapor or showing a variable boundary of the two states. Pressure drops were accounted in the model. On the other hand, the air could either show dry, wet or frost regime, depending on atmospheric conditions and wall temperature. The air pressure drop was also accounted for. Finally, the wall (tubes + fins) was considered as a thermal capacity, exchanging heat with both fluids and other surrounding fins and tubes, by the means of thermal fin conductivity.

The second part of this chapter explained different phenomena involved in the nucleation process on (super-)hydrophobic surfaces. The described model obviously accounted for the surface contact angles but also for its roughness and tilt. Based on the different surface and atmospheric conditions, the numerical tool presented here allows to determine the nucleation time period. The latter can be infinite if the water droplet never freezes.

Ultimately, the objective is to merge both models to obtain a global heat exchanger model, accounting for the surface wettability. This task is undertaken in Chapter 5. However, at this stage, those models were not challenged yet and the results were not compared yet to the available experimental data. This is the topic of the very next chapter.

Chapter 4

Experimental Validation

4.1 Introduction

The previous chapters presented the data gathered in experimental campaigns and different numerical tools. The present chapter aims at establishing a comparison between the simulation results and the experimental data. As for previous ones, the different levels, namely the heat exchanger and the surface levels are split in two distinct sections, the Sections 4.2 and 4.3, respectively.

For the evaporator, the first step is to identify relevant tuning parameters in the model, allowing the best fit between the different results. Then the principal numerical outputs are compared to the experimental data via different parity plots and/or temporal evolution. The experimental validation is conducted in dry and wet conditions first, corresponding to steady state regime. Then, the frost conditions are tackled. Beside the heat transfer rate, the mass accumulated and the pressure drops, the impact of the thermal fin conductivity is quantified and illustrated.

For the surface facility, the followed procedure is identical to the heat exchanger one. However, this section is shorter, as only the nucleation period is the only relevant measurement. Nevertheless, additionally, the illustration of the effect of heat balance on droplets described previously concludes this chapter.

4.2 Evaporator validation

The experimental validation is the comparison of the experimental campaign described in Section 2.2.4 and the numerical results from the simulation models presented in Section 3.2. However, even if the implemented models mainly rely on physical equations, empirical correlations are also needed. The latter are generally developed in similar configurations but some adjustments may be necessary to obtain a good fit. This is called the model tuning. It consists in highlighting relevant tuning parameters and adjust them to get the best possible fit between experimental data and simulation results.

4.2.1 Identification of tuning parameters

First, convective heat transfer coefficients, on the air and refrigerant sides must be tuned. It mainly allows to correct the exchanged heat powers between the different fluids. Here, only a general correction factor is envisaged:

$$H_{\text{air,cal}} = \xi_{\text{air,H}} \cdot H_{\text{air}} \tag{4.1}$$

$$H_{\text{ref,2P,cal}} = \xi_{\text{ref,2P}} \cdot H_{\text{ref,2P}} \tag{4.2}$$

$$H_{\text{ref,SH,cal}} = \xi_{\text{ref,SH}} \cdot H_{\text{ref,SH}} \tag{4.3}$$

Other parameters considered are the mass flowrate proportion of the refrigerant in each circuit of the evaporator. Only the total mass flowrate is measured. Therefore, based on the infrared pictures and the model, the fractions are recovered through this tuning:

$$\dot{M}_{\text{ref,up}} = \xi_{\text{ref,flow,up}} \cdot \dot{M}_{\text{ref,tot}} \tag{4.4}$$

$$\dot{M}_{\text{ref,mid}} = \xi_{\text{ref,flow,mid}} \cdot \dot{M}_{\text{ref,tot}} \tag{4.5}$$

$$\dot{M}_{\text{ref,down}} = \xi_{\text{ref,flow,down}} \cdot \dot{M}_{\text{ref,tot}} \tag{4.6}$$

On the hydraulic side, pressure drops also need to be tuned. On the refrigerant side, it has already been discussed in Section 3.2.8 and two parameters, K and B need to be determined:

$$\Delta P_{\text{ref,tot}} = P_{\text{ref,su}} - P_{\text{ref,ex}} = K \cdot \dot{M}_{\text{ref}}^{B} \tag{4.7}$$

.

On the air side, pressure drop can be considered in two stages. First when the exchanger is still dry, it only depends on the geometry as well as the air flux conditions. Then, if frost grows in the evaporator, the apparent geometry evolves, increasing the pressure drop. Based on the comparison between the model and the experimental data in dry conditions, it has been decided to tune the friction factor f as :

$$f = \xi_{\text{air,1}} \cdot 0.0267 \cdot Re^{\xi_{\text{air,2}} \cdot \psi_1} \cdot \left(\frac{P_t}{P_r}\right)^{\psi_2} \cdot \left(\frac{P_{\text{fin}}}{D_{\text{col}}}\right)^{\psi_3} \tag{4.8}$$

where $\xi_{\text{air,1}}$ and $\xi_{\text{air,2}}$ are the tuning parameters. As suggested by Da Silva et al. [17], the frost density Eq.(3.22) is tuned via coefficients a, b and c to obtain the best fit possible for air pressure drop.

Finally, as evoked before and illustrated later, the effect of fin thermal conductivity has a major impact on the frost distribution through the heat exchanger. To obtain the best distribution, Eq.(3.46) is tuned. This equation considers the external tube diameter as the height of the fin, in its cross-section computation. However, physically, this can be discussed as the fin is continuous between the tubes and a larger height could be solicited to transfer heat. An empirical parameter ξ_{fin} multiply Eq.(3.46) to obtain the best results.

All tuning parameters and their final values are summed up in Table 4.1

TABLE 4.1: Summary of the tuning parameters and their value

Parameter	Quantity tuned	Value
$\xi_{\text{air,H}}$	Heat transfer coef. (air side)	1
$\xi_{\text{ref,2P}}$	Heat transfer coef. (ref side, two-phase)	0.753
$\xi_{\text{ref,SH}}$	Heat transfer coef. (ref side, superheated)	2.15
$\xi_{\text{ref,flow,up}}$	Ref mass flowrate distribution (up)	0.36
$\xi_{\text{ref,flow,mid}}$	Ref mass flowrate distribution (mid)	0.323
$\xi_{\text{ref,flow,down}}$	Ref mass flowrate distribution (down)	0.317
K	Ref pressure drop	134909
B	Ref pressure drop	0.549
$\xi_{\text{air,1}}$	friction factor (air side)	2.73
$\xi_{\text{air,2}}$	friction factor (air side)	0.53
a	Frost density	308
b	Frost density	0.15
c	Frost density	0
ξ_{fin}	Fin thermal conductivity	1.51

Because of the model complexity and interactions between phenomena, it was very complex to implement a global optimization problem to determine the optimal value of each parameters. A more sequential procedure is then carried out.

1. In a very first stage, all coefficients are set to 1.
2. Thanks to infrared picture of the evaporator in dry regime, the experimental proportion of two-phase and superheated zones are determined, for each circuit.

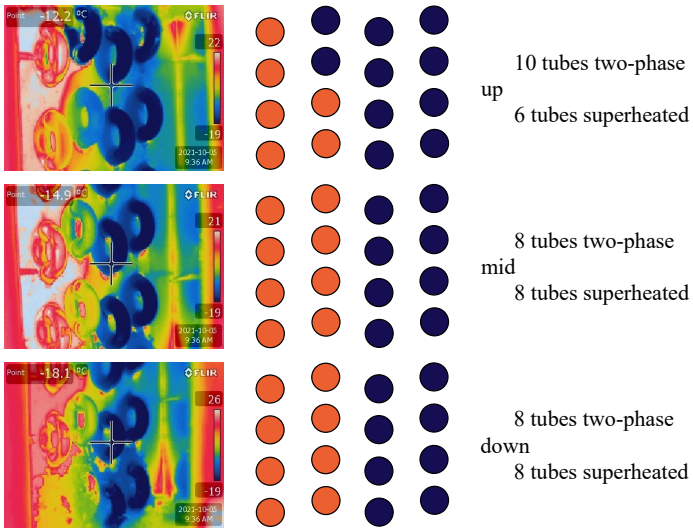

FIGURE 4.1: Experimental proportion of two-phase and superheated zone for each circuit

Only the dark blue tubes from Figure 4.1 are considered as two-phase. What is observed here is that between the mid and down circuits, even if the same number of tubes is considered as in two-phase state, a color difference is observed for the superheated tubes. Unfortunately, the absolute temperatures measured by the means of the IR camera cannot be exploited, as the material emissivity is not known.

3. From observations of bullet [2], $\xi_{\text{ref,flow,up}}$, $\xi_{\text{ref,flow,mid}}$ and $\xi_{\text{ref,flow,down}}$ are tuned to get the same as in the experimental case.

4. As previously said, the sizes of the superheated/two-phase zones are highly dependent on the refrigerant heat transfer coefficients. $\xi_{\text{ref,2P}}$ and $\xi_{\text{ref,SH}}$ are then tuned in parallel to obtain the good distribution.

5. Then, the heat transfer rate balance on the evaporator is checked, in dry regime. If needed, $\xi_{\text{ref,2P}}$, $\xi_{\text{ref,SH}}$ and $\xi_{\text{air,H}}$ are tuned to get the smallest RMSE possible between experimental and simulation results.

6. Then, an iterative process of bullets [3], [4] and [5] is put in place, to converge to the best possible solution.

7. Pressure drops in refrigerant and air fluxes are decoupled from the thermal problem, as said before. They can be tuned independently, minimizing RMSE between experimental and numerical results.

8. Parameters in dry/wet regimes being set, the remaining parameters are associated to the frost regime. First, the fin thermal conductivity ξ_{fin} is set, in order to get the best frost distribution within the exchanger (deeply analyzed later in this chapter).

9. Finally, the density parameters a, b and c are set to obtain the best pressure drop predictions in frost regime.

4.2.2 Experimental validation in steady state

A first check consists in validating the refrigerant and air heat transfer rate models developed in Sections 3.2.2, 3.2.4 and 3.2.5. To do so, from experimental data set, only the dry and wet conditions (no frost) are extracted, to get perfectly steady state conditions. In such a way, experimental data is averaged for periods of more than 10 minutes to prevent any noise disturbance in measurement.

First, the heat transfer rate in dry conditions is analyzed. Here, only the total heat transfer rate is represented on the air side, as there is no latent load.

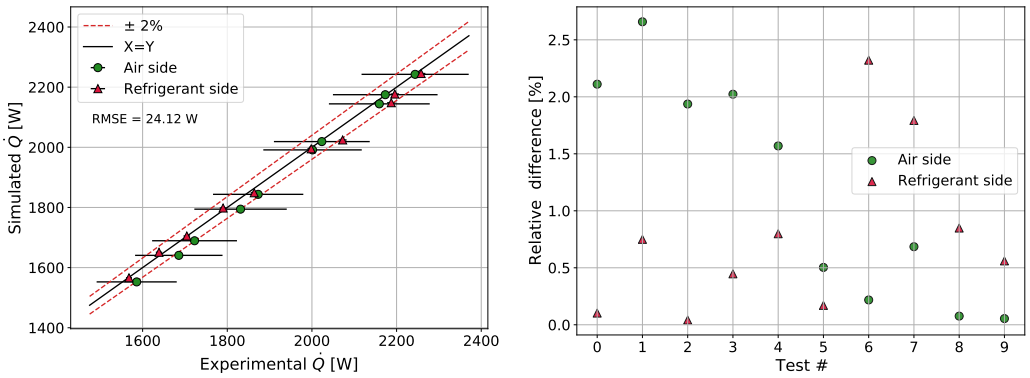

FIGURE 4.2: Experimental vs simulated heat transfer rate for the refrigerant and air side in dry conditions

With a RMSE (Root Mean Square Deviation) of 24 W, translated in a deviation of less than 2.5% (excluding one point), the prediction is satisfying and this sub-part

of the model is successfully validated.

The same exercise is driven for the air in wet regime. Here, the total heat transfer rate is split in the sensible and latent parts.

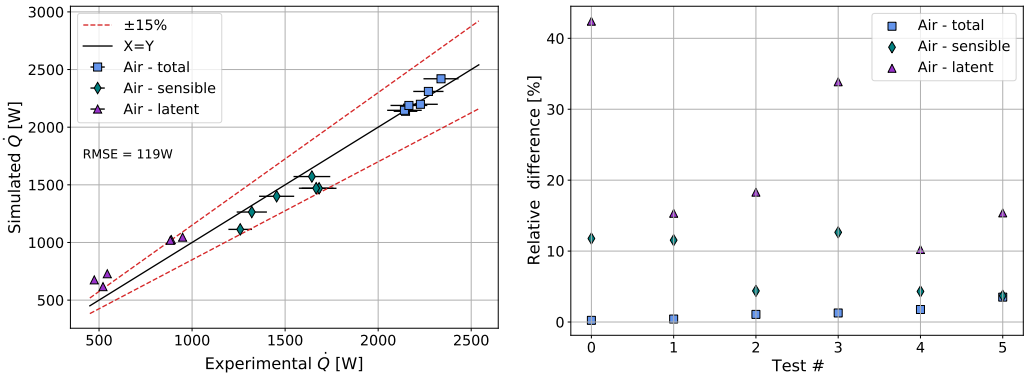

FIGURE 4.3: Experimental vs simulated heat transfer rate for the air side in wet conditions

Even if predictions are not as good as in dry conditions because of the complexity of involved phenomena, a RMSE of 119 W is considered as acceptable. The total heat transfer rate is under the 5% while the sensible and latent load are under and overestimated, respectively.

Now, the pressure drops validation on both sides are checked, still in steady-state.

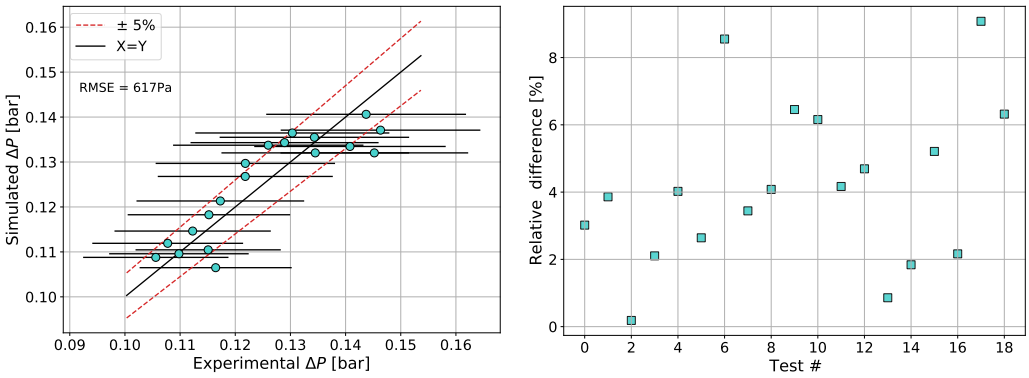

FIGURE 4.4: Experimental vs simulated pressure drops for the refrigerant side

The difference between the modeling and the experimental measurements is under 10% with a RMSE of 617 Pa. Looking at the errorbars corresponding to uncertainties, this difference is clearly acceptable.

Looking at the air side, the scale is very different with, without frost, a maximum ΔP of around 20 Pa.

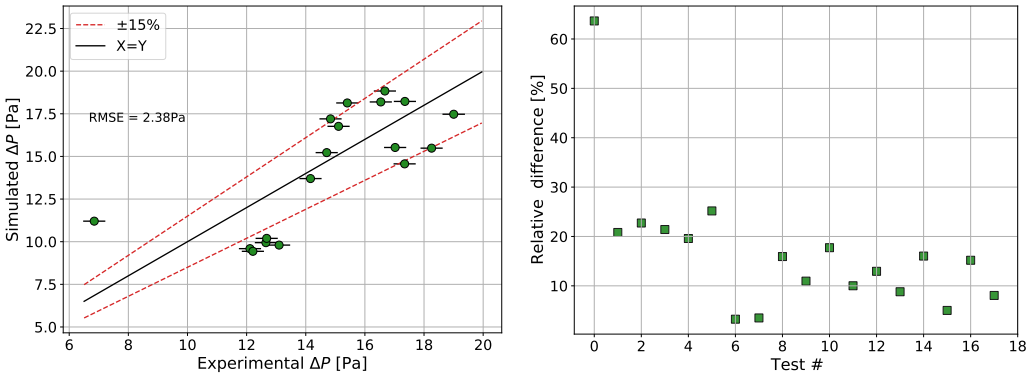

FIGURE 4.5: Experimental vs simulated pressure drops for the air side (without frost)

Even though the results do not seem very good (around 15% prediction accuracy), the RMSE of 2.4 Pa is encouraging. It must be recalled that those pressure drops are in dry conditions and therefore low. The differential sensor has a range of 0 to 125 Pa. This range is compulsory as when frost accumulates, the pressure drops can rise up to 50 Pa. To sum-up, a prediction deviation of 2 Pa in this context is acceptable.

4.2.3 Air side : frost regime

Higher attention is dedicated to the frost regime. The characterization of this phase change, impacts not only the heating transfer process but also an important hydraulic disruption because of the additional pressure drop. Furthermore, as evoked previously, the fin thermal conductivity has an important role in the frost distribution within the exchanger. Based on the experimental records, all these points are tackled in the present section.

Compared to the previous regimes, the temporal evolution is not steady state, for a given test. The different quantities cannot be averaged on the test duration. The approach is then slightly modified. Different parity plots are first exposed. To do so, the average on the complete test is not computed. Three key moments (beginning, mid-test and end of the test) are picked. Beside the parity plots, useful to get the global trend, four representative tests are analyzed in a temporal and spacial way.

The refrigerant side has already been successfully validated previously. As nothing differs from the previous regimes, the focus is put on the air side. First, the total, sensible and latent powers are plotted (air side) in Figure 4.6.

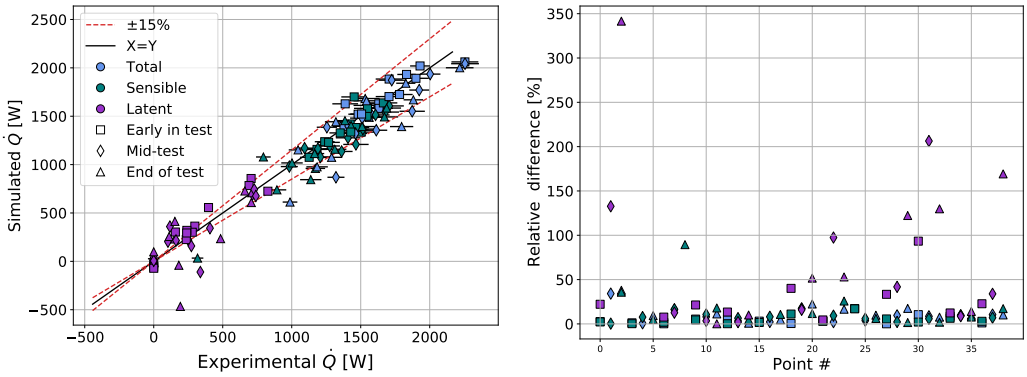

FIGURE 4.6: Experimental vs simulated heat transfer rate for the air side in frost conditions

Globally, the majority of the numerical results are within the 15% error compared to the experimental values. No particular difference can be seen regarding the temporality of the tests, meaning that, with time running, no degradation of the prediction is to declare. Higher differences can be spotted, especially for the latent loads. They mainly correspond to end of test and disturbances that can occur at this time (e.g. valve hunting effects or compressor shut down). This kind of deviation can be observed in Figure 4.7 (N.B. : figure on two pages). It is a temporal representation of the different heat transfer rates plotted for four different tests (Test # 1 to Test # 4 described in Table 2.4).

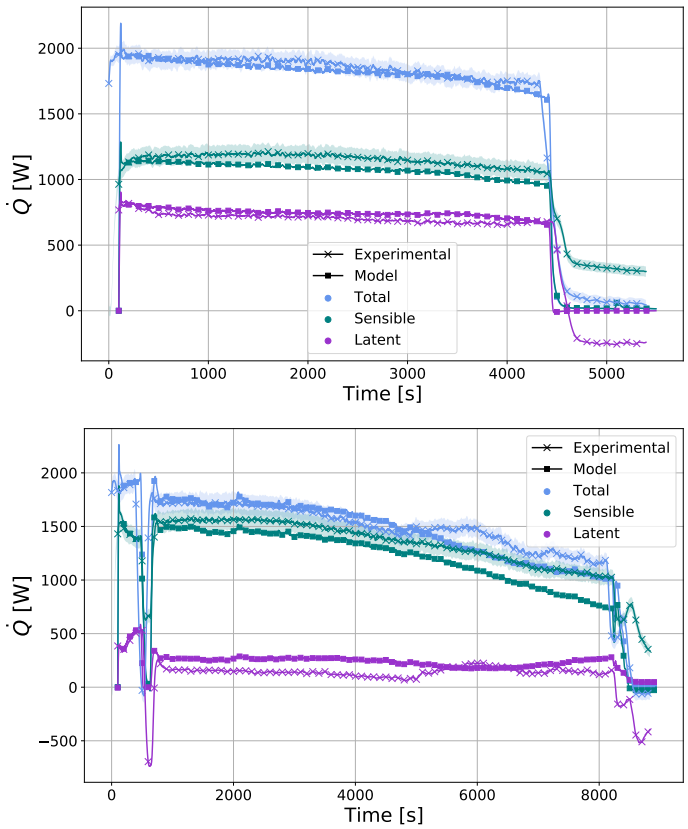

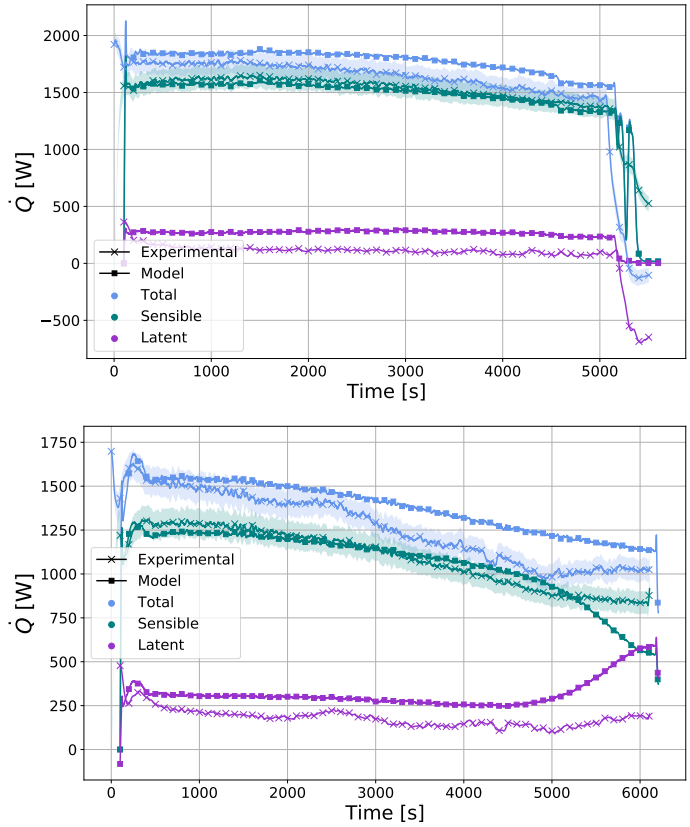

FIGURE 4.7: Temporal evolution of the experimental and simulated heat transfer rates (total, sensible, latent) for the air side in frost conditions

Representative tests are taken here. The lighter strips correspond to the measurement uncertainty. Globally, the different trends are well respected, either for total, sensible or latent heat transfer rates. The test # 4 (bottom) sees an irregular increase of the latent and decrease of the sensible heat transfer rates after about 5000 seconds. This is due to, for this specific test, a bad prediction of frost distribution leading to this inconsistency. It will be highlighted in the pressure drop analysis.

The same exercise is realized for the mass of water accumulated in the evaporator. First a parity plot is showed in Figure 4.8. High disparities are spotted, for very low

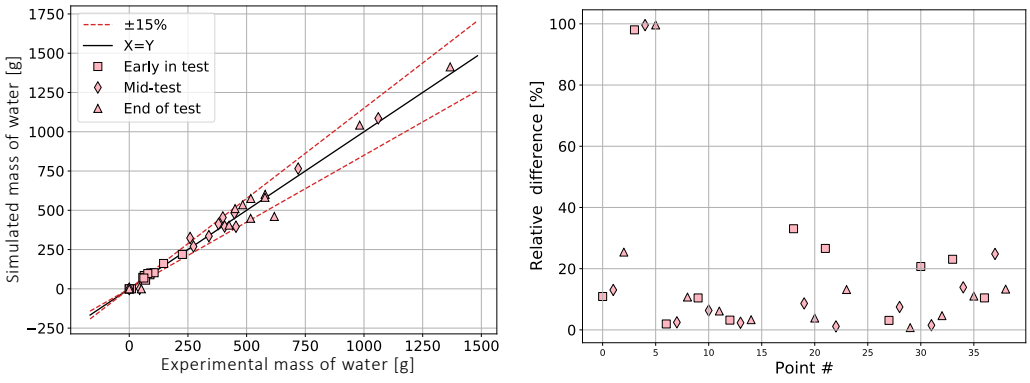

FIGURE 4.8: Experimental vs simulated mass accumulated in the HEX

values. It corresponds to nearly dry tests and at low values, a small absolute variation implies a large relative difference. Apart from those details, the trend is good. Once again, values late in the tests stay satisfying. Based on this result, the mass indicator is considered as sufficiently well predicted by the model, compared to the experimental values. The trend for the same four tests are displayed in Figure 4.9.

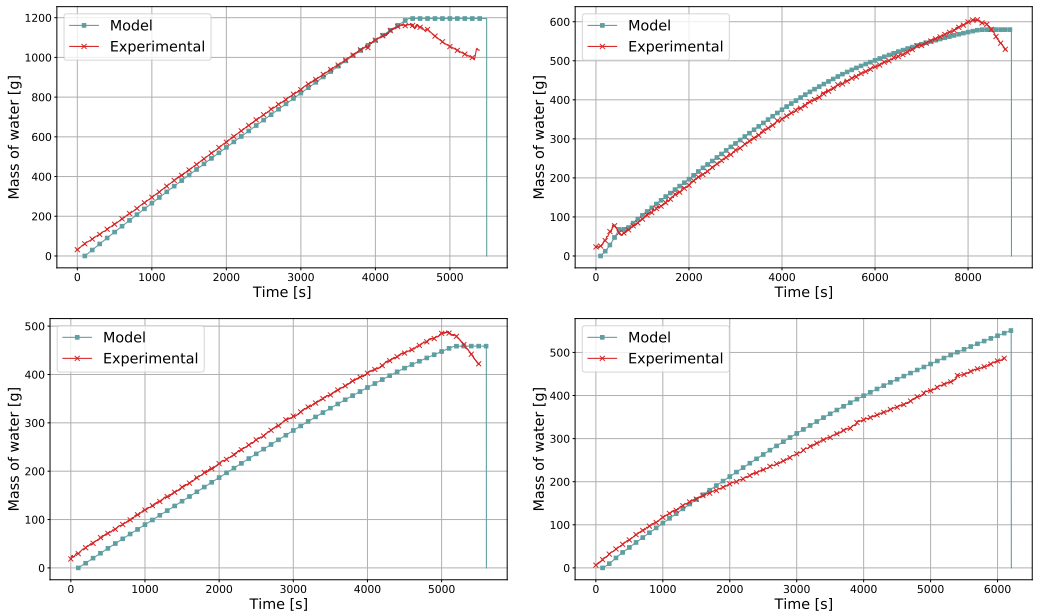

FIGURE 4.9: Temporal evolution of the experimental and simulated accumulated mass in frost conditions

The first comment is that the uncertainty light strip is not visible, compared to the Figure 4.7. This is explained by the good accuracy of the force sensor. Then, no defrost phase is simulated, explaining the constant value after the experimental maximum. No dedication is brought to this phase, because of the very short characteristic time compared to the frost phase (see pressure drop evolution). However, this should be considered if a complete cycle is studied. Even if slight offsets may be observed, it confirms the results of Figure 4.8, the predictions of the simulation model fit very well the empirical observations.

Then, comparison between simulation results and experimental data is applied to the air pressure drop, in Figure 4.10. Very high discrepancies are noticed, especially for the points corresponding to the end of the tests. As the model has successfully been validated in dry regime, it is expected to find a good match for the beginning of the tests (as nearly no frost is present). However, as the tests go, the prediction can stay either sufficiently good, or they are largely overestimated. The mismatch between predictions and experimentation is after more than one hour of test. The most important factor explaining this phenomenon is the extremely high dependence on many different parameters. Basically, it depends on the frost thickness and distribution within the exchanger. Despite the frost density directly impacting the frost thickness, the fin conductivity and refrigerant split in the exchanger has a tremendous influence on the distribution and then on the pressure drop. The fin conductivity impact is deeply studied later on. Regarding the refrigerant, a small distribution variation implies more or less frost formation in the top or bottom of the exchanger. If this is not properly set, a blockage effect may be computed while it is not the case in reality. Imposing a constant refrigerant distribution throughout a complete test

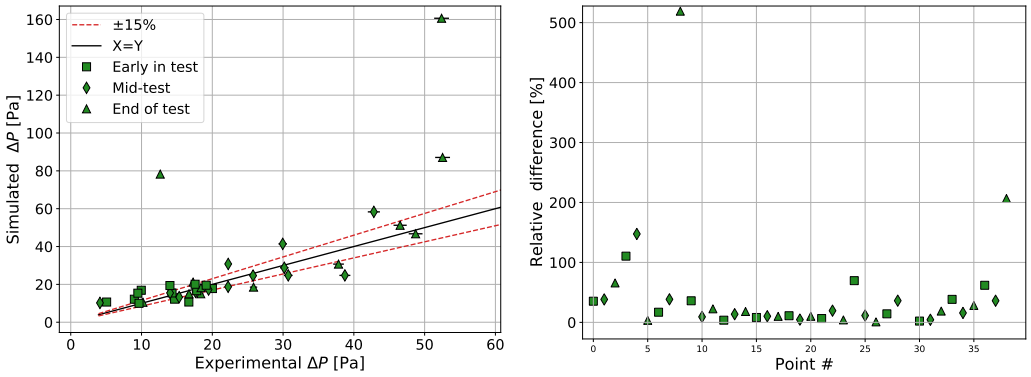

FIGURE 4.10: Experimental vs simulated pressure drops for the air side (with frost)

duration and between the different test is an assumption having a deep impact on air pressure drop predictions. However, because of the available resources, this distribution is not furtherly refined. Those results should be put in perspective with the temporal evolution of the four different tests in Figure 4.11.

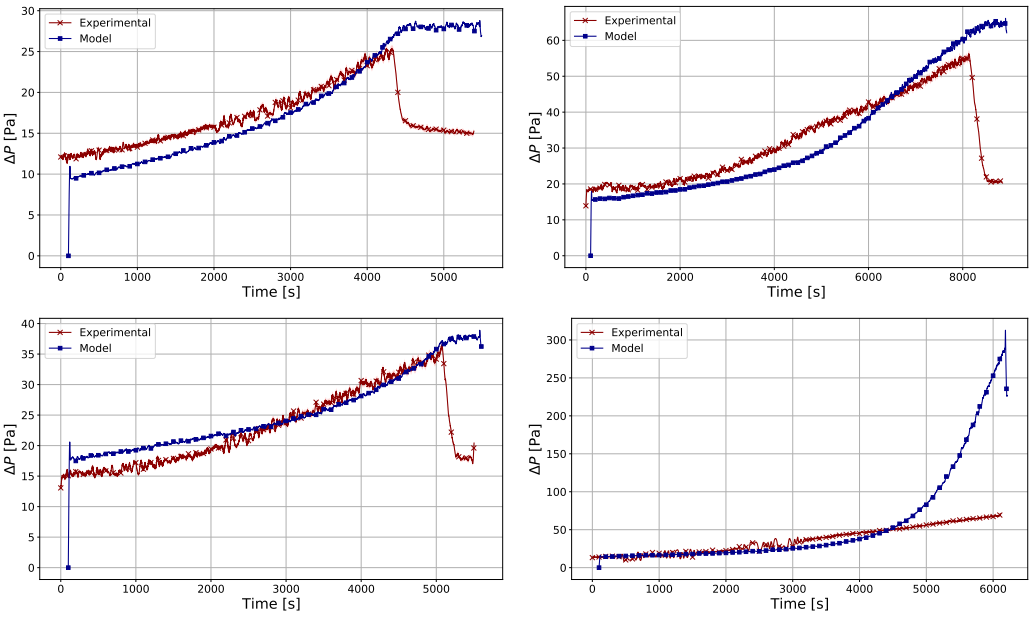

FIGURE 4.11: Temporal evolution of the experimental and simulated pressure drops for the air side in frost conditions

Once again, the temporal trends confirm the conclusion drawn in the parity plot previously analyzed. For the first three tests, the trend is satisfying during the complete test duration with only small offsets. As evoked previously, the defrost phase is not implemented here, explaining the constant value of simulations at the end of the tests. The defrost phase corresponds to about 5% of the cycle time (frost+defrost). No emphasis is put on this, even if this should be compulsory for the study of a complete system. The last test shows a large deviation after 5000 seconds (cf. Figure 4.7). This is because of the sensitivity of pressure drops to frost distribution and density. In this specific case, the model predicts a blockage of one part of the exchanger.

After the study of these conventional quantities, an add-on of this thesis is to study the frost distribution, regarding the impact of the fin thermal conductivity (FTC). The corresponding modeling description can be found in Section 3.2.7.

To do so, the relevant available experimental data is the frost thickness extracted from pictures of the different top tubes (and fins) during the test duration. First, to illustrate the FTC effect, pictures of a representative test is taken after 10, 60 and 90 minutes. These pictures are faced with a representation of the predicted frost thickness on each tube of the evaporator. The model is, at first, ignoring FTC effect, as it is the case in all previous works examined by the author. Then, the exact same simulation is executed considering this effect. Those representations are found in Figure 4.13.

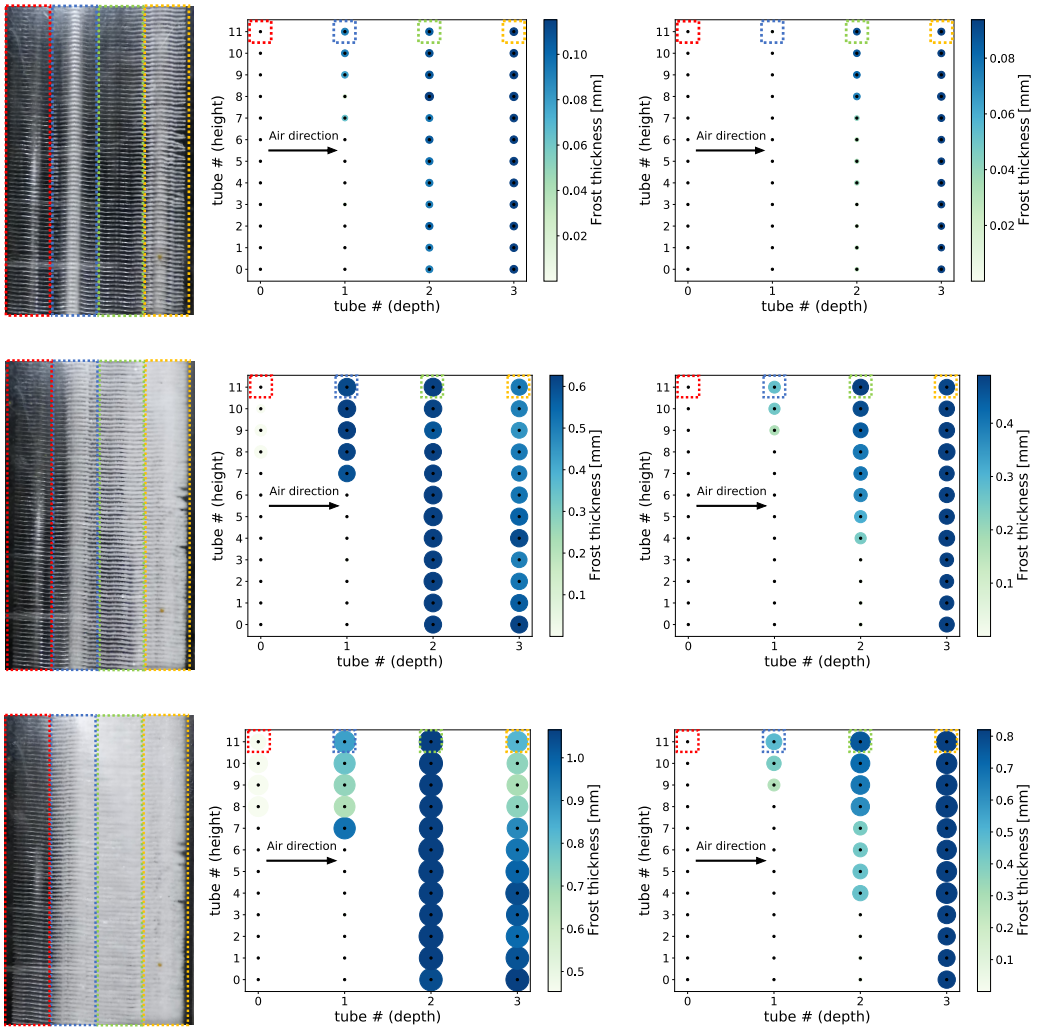

FIGURE 4.12: Frost distribution in the different tubes of the heat exchanger. From top to bottom, figures corresponds to 10, 60, 90 minutes, respectively. The left corresponds to the actual picture of the test, the **center** and *right*, to the model result **without** and *with* FTC, respectively

Figure 4.13 explicitly reveals the impact of this phenomenon. The first general comment is that there is an uneven distribution of frost on the exchanger height because of the unbalanced refrigerant split. Then, the size of the circles is only qualitative and is not proportional compared to the exchanger geometry. This size is a

good indicator to get a general view on the frost distribution while the colors bring more accuracy to the actual thickness. Finally, all the tubes of the exchanger are represented. However, the visual access is only available on the top of the exchanger. Those are highlighted with colored boxes.

Minute 10. Even if the difference is not dramatic, the picture explicitly shows frost on the yellow tube. At this stage, without thermal conductivity, frost already appears on three out of four tubes. This effect is reduced thanks to the FTC.

Minute 60. The experimental data shows a more important quantity of frost at the yellow tube level. Then going backwards, this quantity decreases. Without FTC, the predictions differs with a larger quantity on the green and blue tubes. As no thermal transfer is accounted between tubes from different temperatures (over-heated and twh-phase tubes), humidity from air frosts as it hits the first sub-zero tube (if dew-point conditions are met). The air being dryer for the next tubes, the quantity of frost accumulated is smaller. Now, accounting for FTC, the superheated tube heats-up the next tubes. It increases the surface temperature of neighbor tubes, delaying the frost formation on the further tubes.

Minute 90. The analysis made for minute 60 is the same, or even emphasized. Small amount of frost is predicted on the red tube without FTC, which is not observed on the experimental data.

The previous analysis focuses on three specific moments of the test and no quantitative comparison between the model predictions and the measurements is provided. To complete the analysis, a temporal comparison is realized, again, with and without FTC effect.

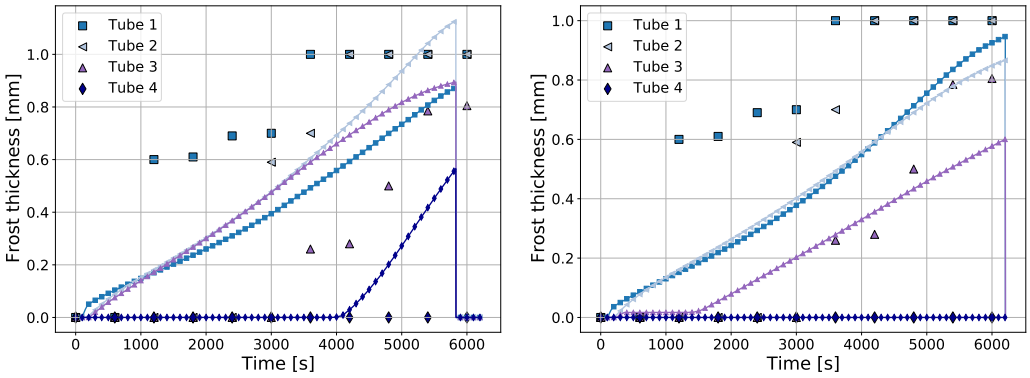

FIGURE 4.13: Experimental (discontinuous markers) and simulation (continuous lines) representations of temporal evolution of frost accretion on the four top tubes of the evaporator. Left figures does not account for FTC while the right does

The conclusions are the same as in the previous analysis. Tubes 2 and 3 dominate in terms of frost thickness over Tube 1 (yellow in Figure 4.13). Furthermore, a bad prediction of frost accretion on Tube 4 (red in Figure 4.13). Even if the fit is still not perfect, a substantial correction is brought thanks to the FTC consideration. Looking at the numerical values, even in the best case, the match is not perfect. However, it should be recalled that the thickness is in tenth of millimeters and the experimental data comes from a picture analysis (see Section 2.2.4). This technique is efficient but may present a lack of accuracy, explaining the difference between the simulations and

experiments.

To sum-up, this section shows that the novelty brought with the consideration of FTC is a real add-on in the frost formation simulation in heat exchangers. A bad frost distribution prediction due to the lack of FTC implies bad predictions in the pressure drop characterization and may have a serious impact on the design of heat exchangers.

4.3 Coated surfaces validation

The aim of this section is to compare the predicted time of nucleation phase (i.e. the time needed before getting a completely covered surface) compared to the experimental observations. As detailed in Section 3.3, three different parameters allow the tuning to fit the experimental data to the surface models:

- The roughness size R_r (see Figure 3.19) and this for the aluminum plate and for the superhydrophobic one (as each may present different roughness patterns).
- The kinetic constant I_0 involved in the nucleation rate described in Eq.(3.75).

The impact of I_0 has already been discussed in Section 3.3.3. As the authors in literature are not unanimous on its value, it is here a degree of freedom to tune the nucleation time. At first, unlike the roughness, I_0 is considered as common to both surfaces. Regarding the roughness, from the equations, the smaller, the more subject to nucleation the surface will be. It implies that roughness also allows to refine the prediction of the nucleation time.

As a recall, either the experimental data or the model shows three different cases:

- Desublimation : water vapor directly turns into frost, without going through liquid phase
- Condensation + solidification : water vapor turns into liquid, then the droplets freeze
- Condensation : water vapor condensates and the droplets stay in liquid state

In the experimental campaign no test showed perfectly dry conditions. This case is therefore not discussed in this chapter. In the present study, the last bullet corresponds to an "infinite" nucleation period. Indeed, the liquid droplets keep popping, but do not freeze for the duration of the test and are likely to stay liquid forever. Unlike this case, the first two items correspond to a finite nucleation period. As soon as the plate is completely covered with frost, this phase is over, leading to the frost growth period.

The model taken as described in Section 3.3 did not show satisfying results. After a first try with the tuning of parameters, large discrepancies are observed, and after a quick analysis, it reveals that the ambient conditions have a very large impact on predictions. Indeed, keeping the exact same conditions and changing the air temperature from 18°C to 13°C changes the predictions by several orders of magnitude, unlike the observations. This is true, for any parameter value of I_0 ranging between 10^{27} and 10^{31} $\mathrm{m^{-2}s^{-1}}$, as mentioned in the literature.

The ambient conditions only impact the nucleation rate I from Eq.(3.75) via the Gibbs energy barrier. A convenient method to decrease the impact of the Gibbs energy barrier (i.e. the impact of ambient conditions) is to decrease the value the parameter I_0. Decreasing this parameter, all other things being equal, increases the nucleation period. To keep it at acceptable values, the other available parameter, namely the roughness size, must be lowered. This results in a lower value of the $\Omega = f(\theta, R_r)$. As ΔG is directly proportional to Ω (see Eq.(3.74, 3.82), the Gibbs effect is minored so are the ambient conditions. To sum it up, considering a smaller kinetic constant I_0 (even lower than what is found in literature) allows to reduce the ambient temperature and humidity effect on the prediction of the nucleation time.

Furthermore, the tuning of the three parameters ended-up in the conclusion that they were not sufficient to deliver good predictions for both surfaces simultaneously. Consequently, a different kinetic constant I_0 is attributed to each surface, allowing a a quality enhancement of the model output.

Finally, the tuning parameters values are found in Table 4.2.

TABLE 4.2: Tuning parameters involved in the nucleation model

Parameter	**Aluminum**	**Superhydrophobic**
I_0 [$m^{-2}s^{-1}$]	10^{21}	10^{24}
R_r [nm]	0.41	0.26

The values of I_0 are already discussed here-above and are lower compared to the values found in the literature (between 10^{27} and 10^{31} $m^{-2}s^{-1}$). In the present case, it is a convenient solution to reduce the impact of ambient conditions. The lower value of the aluminum shows that temperature and humidity of surroundings has a smaller impact on the nucleation process, compared to the superhydrophobic coating.

Looking at the values of the roughness size, according to the literature [39, 61, 81], the values considered here are slightly smaller than what is observed. However, the order of magnitude for hydrophobic surfaces is from few nanometers to hundreds of nanometers, showing a coherence.

The comparison between experimentation and simulation are, for both aluminum and superhydrophobic, presented in Figure 4.14. For clarity reasons, when droplets stay at the liquid state, the nucleation time is set to $+\infty$.

The first comment is that no uncertainty bar are displayed in this figure. It is explained because the measured experimental time is based on the analysis of the pictures and, despite two different tools implemented, no uncertainty value is available. So, there is an uncertainty for the experimental data but it cannot be quantified. Even if it is as small as possible, the error margin may be relatively important and it should be kept in mind for the rest of the analysis.

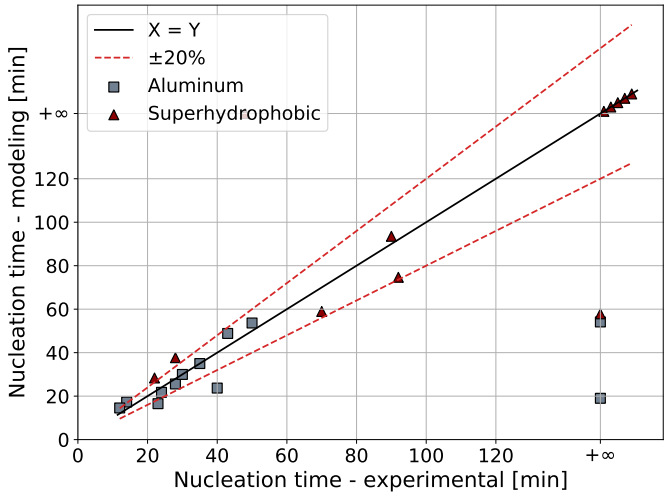

FIGURE 4.14: Experimental vs sumultated time needed before obtaining a uniform frost layer (i.e. nucleation period) for the aluminum and superhydrophobic samples

At the first sight, the trend for both materials is encouraging, even if some disparities are to be noticed. For the nucleation on the aluminum plate, the predictions are very good as soon as there is frost. The two tests where the droplets stay liquid, the prediction are underestimated. For the aluminum plate and its low contact angle, the model struggle to predict the liquid state. As explained previously, the model is very sensitive to the conditions. If one experimental measurement presents a slight offset, the impact on the model may be considerable.

Looking at the superhydrophobic results, the majority of the tests in liquid state are well predicted. The tests with a small time of nucleation have also a good trend. Two points in between are diverging, for the same reasons of sensitivity than exposed previously. The model and experimental techniques may certainly be improved on many points. However, the main expectation of this first surface model is to predict a general trend, which is successfully achieved here.

Beside the nucleation time, the energy balance on the droplet determining its temperature detailed in Figure 3.23 and 3.24 can be illustrated here, thanks to the comparison between the natural and forced convection recorded in Chapter 2. Indeed, Section 3.3.5 shows that for a fixed temperature plate, the higher the air speed, the hotter the droplet and the more likely it will stay liquid. The experimental chapter shows the evolution of the superhydrophobic surface at -5°C with very low and 1.2 m/s air speeds. In both cases, droplets stay mainly liquid. However, because of edge effects, the water droplets may freeze, being in contact with colder ones. Experimental tests show that at the end of the test, for the natural convection case, those edge effects (ignored previously) are perceptible (yellow zone in Figure 4.15, top). However, for the forced convection, because the stream helps to increase the temperature of the droplets, the edge effect are lightened. This is illustrated in Figure 4.15 (bottom).

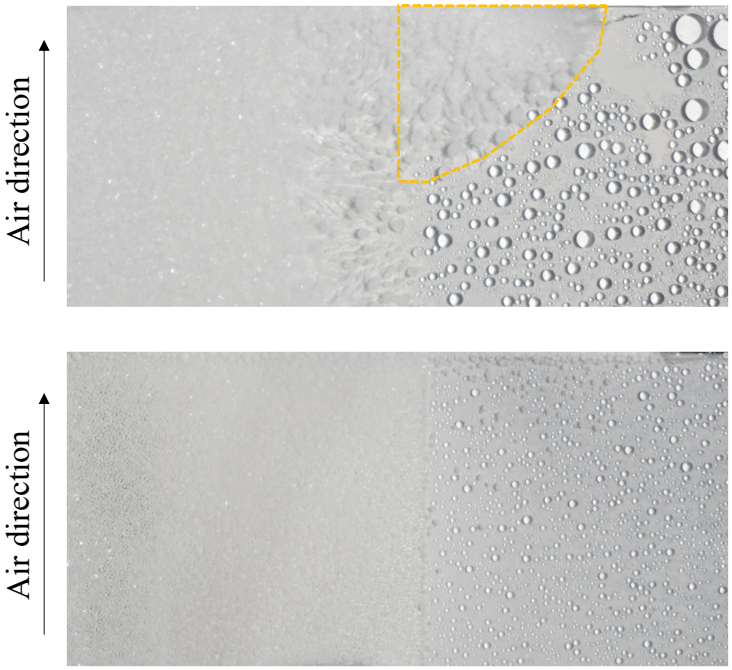

FIGURE 4.15: Visualization of a the edge effect in natural convection (top) and forced convection (air speed = 1.2 m/s) (bottom). The left part of the plates is the aluminum substrate while the right part is the superhydrophobic one. The air temperature and humidity are at 18°C and 75%, respectively. The plate is at -5°C.

From those results, the conclusion is that a good trend of the model is observed compared to the available data. Eventually, the numbers do not perfectly fit, and the sensitivity of the model may be the major reason. However, for a first study of this kind, it is considered as good enough to investigate the impact of hydrophobic surface in heat exchangers. This is precisely the topic of the following chapter.

4.4 Summary and conclusions

This chapter first aimed at developing a methodology to tune relevant parameters of the evaporator model. It then successively showed satisfying results between the experimental data and the numerical results. First, the steady state was tackled with dry and wet regimes. Then the frost regime was studied. Globally, every predictions matched closely with the experimental data, except for the air pressure drop for few tests showing high blockage ratio. This chapter was also the opportunity to demonstrate the benefits of taking into account the fin thermal conductivity for heat exchangers modeling in frosting conditions. If this effect was not considered, it was shown that the frost distribution within the device through time was badly predicted. Accounting for this effect allowed to get much closer to the empirical observations.

Beside the results regarding the heat exchanger, this chapter gave the opportunity to compare the predictions of simulations and experimental results for the nucleation duration time. Even if the surface models were relatively simple and relied on many assumptions, it has been found that the predictions were coherent for the majority of the tests. Furthermore, the comparison between natural and forced convection on

different samples at the experimental level allowed to illustrate the modeling considerations about the droplets temperature computation. Indeed, a sample in natural convection was more subject to edge effect because of its lower droplets temperature, compared to the same one in forced convection. This was what was expected from the modeling developments.

Models at both scales being experimentally validated, it is now possible to trustfully merge and exploit them, to predict performance of an evaporator with hydrophobic coatings.

Chapter 5

Multiscale Merge

5.1 Introduction

This ultimate chapter is the first one to merge both, heat exchanger and surface phenomena, in a single model.

After quickly showing how both models interact, the sensitivity of some parameters of the model is illustrated. Then, the heart of this chapter is to study the impact of the surface wettability on the evaporator. The main criterion analyzed is the time needed for the device to be blocked by the frost, in various conditions. The impact of ambient temperature and humidity as well as the fan speed are investigated.

Finally, a very first step of the impact of wettability in fins and tube heat exchanger is evoked and illustrated by the means of the available simulation tool.

5.2 New model application

As previously evoked, the ultimate objective of the present thesis is to merge the surface and exchanger model. To do so, the decision tree of the models to select the regime on the air side of the evaporator presented in Section 3.2 is upgraded.

For the initial exchanger model, depending on surface temperature and air conditions, a tube could stay dry, be wet or frosted, as illustrated in Figure 3.5. Now, an additional mode is added, namely the nucleation mode. The surface model described in Section 3.3 is called in a first time to determine if surface and atmospheric conditions are met to initiate nucleation. If so, the nucleation mode is launched, computing the time necessary to obtain a uniform frost layer. If no nucleation phase is to declare or if the considered tube shows a uniform frost layer (post-nucleation), the model switches back in the classical mode. The algorithm scheme is illustrated in Figure 5.1.

As both models (i.e. heat exchanger and surface) have sucessfully been validated, they are merged to get an analysis of the behavior of the evaporator, varying its surface characteristics. In a first step the roughness is investigated before the analysis of the effect of contact angle, more extensively studied.

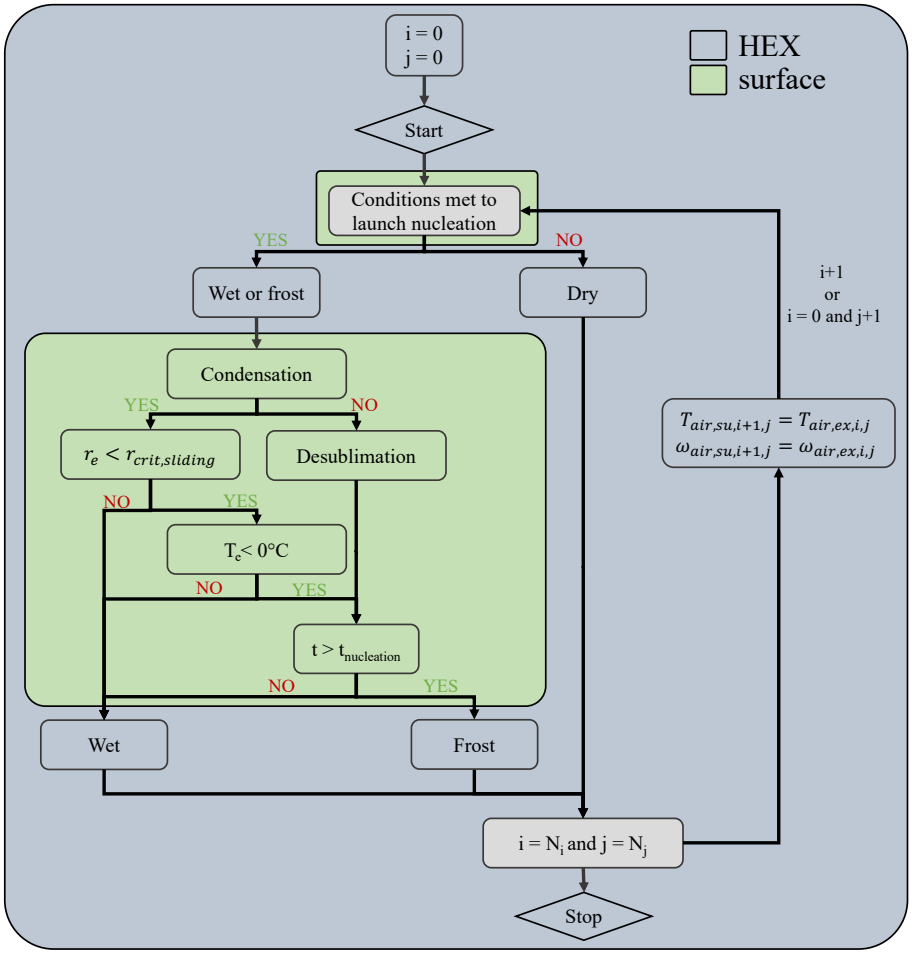

FIGURE 5.1: Model merge algorithm flowchart

5.3 Impact of surface roughness on the evaporator

To study the impact of the roughness effect on nucleation, basic examples of cold horizontal plates are still employed for sake of simplicity. Indeed, its impact is very sensitive and this small study is self-sufficient in the frame of this study. Three different figures are represented in Figure 5.2. In the first two, the contact angles are set, to 90° and 162°, respectively (i.e. to the contact angle of the aluminum and superhydrophobic coating). Then, for given atmospheric conditions (18°C and 75% RH), the nucleation time is plotted regarding the plate temperature T_{wall} and roughness radius R_r (cfr. Figure 3.19). The plate temperature is set to -10°C, and the nucleation time is represented as function of the contact angle θ and the roughness. A first comment is that the white part corresponds to cases where the nucleation time is infinite (i.e. no frost is to declare). Then, from the top two figures, taking a given roughness radius R_r, a small variation of the wall temperature induces a large nucleating time modification. This is physically coherent and aligned with observations. Indeed, a plate at -8°C may frost relatively quickly while no frost is observed after hours in the same conditions for a plate at -5°C.

Now, still on the top figures, considering a given plate temperature, a slight variation of the roughness size (i.e. tenths of nanometer) also implies a large variation of predicted nucleation time. This observation is especially highlighted for the smallest

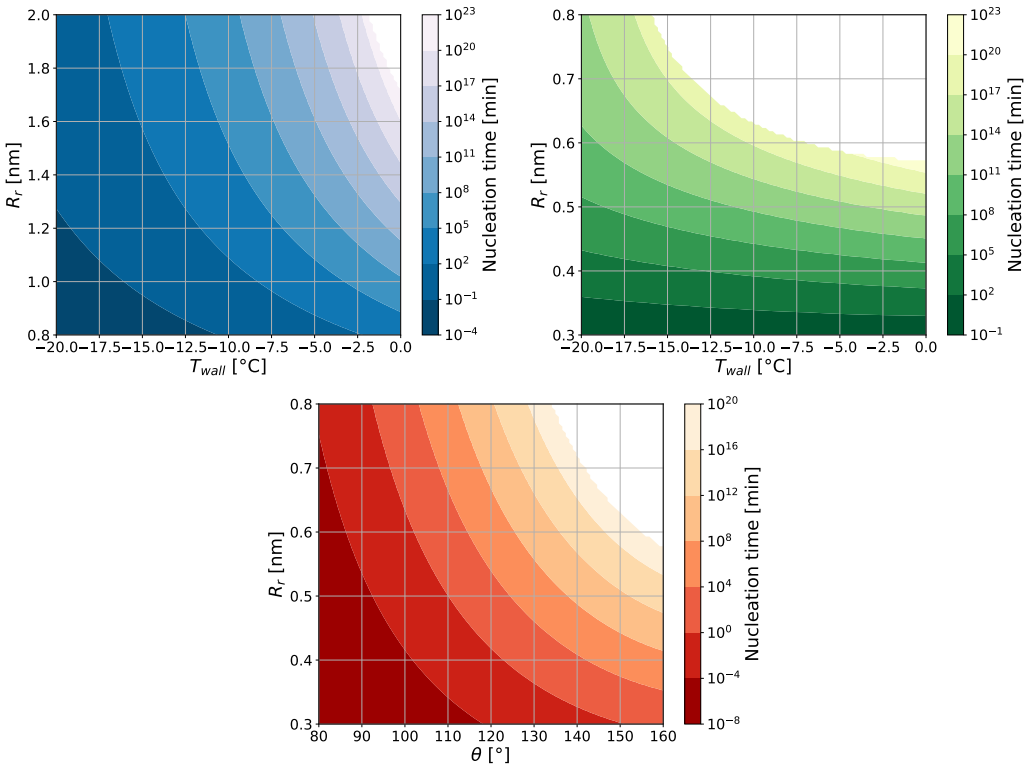

FIGURE 5.2: Nucleation time regarding the roughness size and the wall temperature for a contact angle of 90° (top left), the wall temperature for a contact angle of 150° (top right) and the contact angle for a wall temperature of -10°C (bottom)

contact angle. It means that, even a small accuracy deviation in the tuning of this parameter, induce dramatic prediction deviations. Furthermore, if the material shows an heterogeneous roughness distribution, the nucleation scheme may differ considerably.

Now, looking at the last figure (in red), the relation impact of contact angle and roughness is illustrated simultaneously. The main observation extracted from this figure is that to keep the same order of magnitude for the nucleation time, if the contact angle is increased, the roughness size should decrease. It is indeed what is observed in the tuning of the surface parameters for the experimental validation.

Based on those analyses, the model should be used very carefully. Indeed, even if the model is validated for a single smooth plate, the frost accretion in a heat exchanger is a whole different story. First, as previously said, a small error on the parameters has tremendous consequences. Then, a heat exchanger shows very complex geometries with numerous nucleation sites, fouling, etc. The high sensitivity of those parameters is then a weakness of the model.

However, trends can still be drawn, showing the impact of contact angle on the performance of the evaporator. To do so, a fixed roughness size is kept. The chosen roughness size is the one identified for the superhydrophobic coating. This value fits both the experimental results at the scale of the exchanger for the "classical" evaporator (i.e. very small nucleation duration time for a contact angle of 90°) and

decent values for superhydrophobic coatings applied to the heat exchanger application.

5.4 Impact of contact angle on the evaporator

In this section, a real case test is emulated. To do so, constant supply conditions are imposed on the air and refrigerant sides. The air temperature and humidity are supposed constant for a test duration time. However, the mass flowrate may vary because of the pressure drop increase due to frost. To account for this, a fan model has been implemented, to correlate the mass flowrate regarding the pressure drop of the system. Details of this model can be found in Appendix D. On the refrigerant side, constant supply conditions are considered. Obviously, this may not be the case, because of the system evolution with frost accumulation. However, it would be necessary to model the complete cycle to catch those supply variations. The choice here is to avoid this complete modeling because the focus is not set on the cycle in this thesis and the performance trends of the evaporator will stay the same.

Another parameter depending on the surface is the hysteresis contact angle. As both are known for aluminum and for the superhydrophobic coating, it has been decided to do a linear digression for those, between the neutral and superhydrophobic materials. It is consistent as in general, the higher the hydrophobic level, the smaller the hysteresis contact angle. It is to note that specific materials can be developed, showing other trends. Those are not considered here.

5.4.1 Impact of wettability on the state of water in the evaporator

The surface model, which is plugged to the model of the evaporator, can give the condition of each tube of the exchanger on the air side. The tubes (and corresponding fins) can be either dry, wet or frosted. But, going more in details, depending on conditions, for the wet conditions, two options are highlighted. The liquid droplet can either stick to the wall or, slide on it. It depends on the surface characteristics (static and hysteresis contact angles) and on the droplet size.

As the information is available, a quick study is undertaken to spot, for different rows, the state of water on the tubes, for different contact angles. Only four rows in the middle of the exchanger are displayed for the sake of clarity. On the height of the exchanger, the other tubes are likely to present similar conditions. As a reminder, the *Tube 1* corresponds to the refrigerant supply and air exhaust while the *Tube 4* is the opposite.

Different pieces of information can be extracted from Figure 5.3. At first sight, the contact angle does not seem to have any impact, excepting superhydrophobic surface for surface showing higher temperatures. Different factors explain this phenomenon. At the exhaust of the evaporator on the air side (*Tube 1*), the surface temperature is below zero. It has been seen previously that if the surface is under 0°C but still close to this value (between -8°C and 0°C), the odds for a droplet to freeze on superhydrophobic material are low, thanks to their higher interaction with the surroundings. However, even if the temperature of the air at the supply is 18°C, at exhaust, it is much colder. It results in a colder nucleus temperature leading to frost. This effect is emphasized because of a simplification of the surface model. Indeed, there is no model of droplet growth in this work. It results in smaller droplets, interacting less

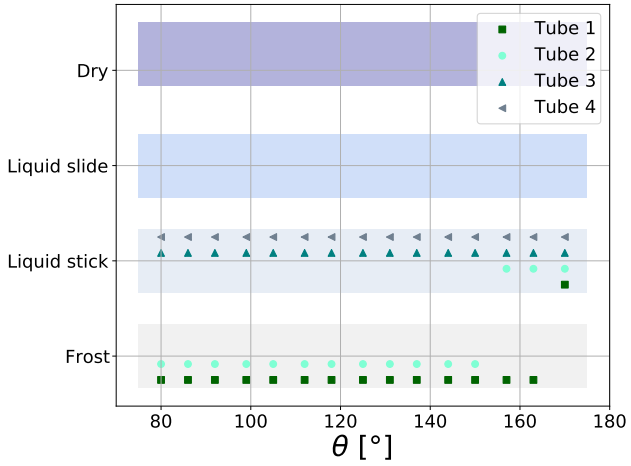

FIGURE 5.3: State of nuclei on the exchanger tubes for different contact angles.

with surroundings. This simplification also explains another observed phenomenon. Whatever the contact angle, the droplets stick to the fins (even if the latter are vertical). It means that the critical nucleus size (considered here) is still smaller than the minimum size to have a motion effect due to gravity, even for high contact angles. It shows here a limitation of the present model in the frame of heat exchangers.

Based on this, does it mean that the wettability of the surface will not have any impact on frost growth in heat exchanger? Beside the state of water, another capital quantity is the time needed to cover the surface (nucleation period). Even if the nuclei are frosted, there may be a delay before the frost growth period, depending on the type of surface. The figure 5.4 illustrates this evolution. It is worth noticing that those results are taken when the evaporator just reaches steady state. The situation can evolve looking at longer time (as seen in the experimental study of the evaporator in frost conditions).

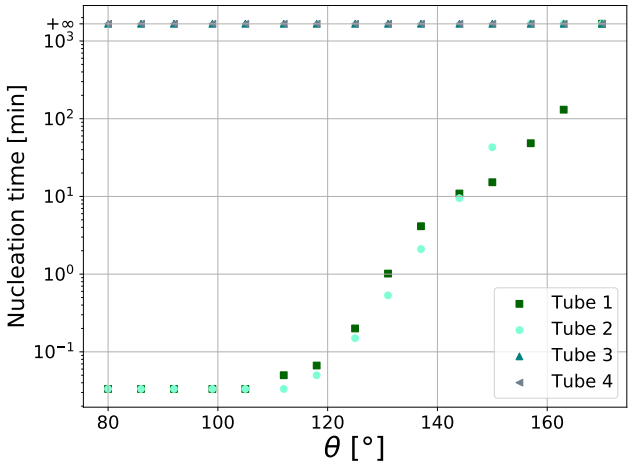

FIGURE 5.4: Nucleation time on the exchanger tubes for different contact angles

Paying attention to the logarithmic scale, no major effect is identified for contact angles smaller than 130°. This is in line with observations from Chapter 2. Keeping

the increase of the hydrophobic level, the delay increases exponentially. In other words, even if the state of nuclei is solid for superhydrophobic coatings, in practice, the delay before observing actual frost growth is so long that it can be considered as frost-free.

5.4.2 Impact of wettability on the blockage time

As previously evoked multiple times, one major issue of frost formation in heat exchanger is the increase of the air blockage leading to a pressure drop increase and flowrate decrease. In this frame, the first effect analyzed is the time required for the exchanger to be blocked. The evaporator is considered as blocked when the volumetric flowrate falls under 25% of the initial one. The impact of the contact angle is naturally the main studied parameter. In complement, the impacts of the supply temperature, supply humidity and fan speed are investigated. The reference conditions are a supply temperature of 18°C and 75%, respectively and a fan speed of 1850 RPM giving a volumetric flowrate of about 165 m^3/h. As a first step, the delay before the heat exchanger blockage is studied for three different supply temperatures of 10, 14 and 18°C.

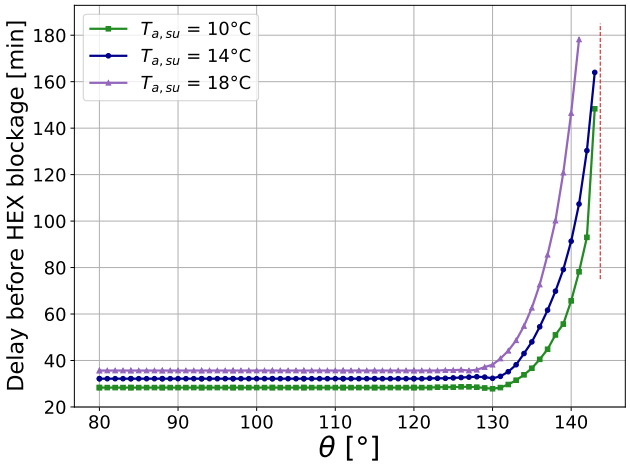

FIGURE 5.5: Time necessary for the air flowrate to fall under 25% of its nominal value, as a function of the surface contact angle

From Figure 5.5, different elements can be analyzed. The most sticking information is that the delay does not change regarding the hydrophobic level, from contact angles ranging from 80° to nearly 135°. It is in line with the conclusions from Section 2.3.3 and the work from Hermes et al. [32]. However, for higher hydrophobic level, the time necessary exponentially increases. At about 150°, for these conditions, the necessary time is about 2 hours (versus less than 40 minutes for neutral smaller contact angles). Then, an asymptotic behavior is observed suggesting that from a certain contact angle (>150°), no frost will accumulate in the device. Once again, this information is coherent with observations made on superhydrophobic samples (e.g. in Figure 2.39).

In classical cases of heat exchanger submitted to frost conditions, the surface temperature shows negative temperatures but may not be far from 0°C. However, as explained previously, if the frost quantity increases, the refrigerant evaporating pressure decreases, leading to a decrease of the surface temperature which eases the frost

formation. On another side, superdrophobic surfaces may frost for low surface temperatures. However, as seen in Figure 5.2, if the temperature is sufficiently high (even if below 0°C), no frost deposition is observed. In this case, the evaporation pressure as well as the surface temperature will remain constant. In other words, if the limit conditions of frost launch is not met thanks to superhydrophobic coating, the evaporator will not frost. This explains the asymptotic behavior shown in Figure 5.5.

The same exercise is realized, imposing the air supply to 18°C and varying either the relative humidity or the fan speed. The humidity variation ranges between 50% and 95% while the imposed speed of the fan ranges between 1800 and 2000 RPM corresponding to volumetric flowrate between 135 et 235 m^3/h.

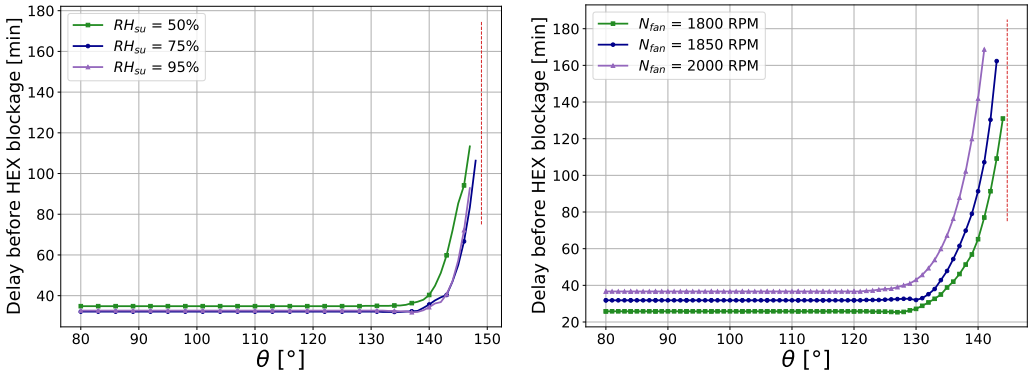

FIGURE 5.6: Time necessary for the air flowrate to fall under 25% of its nominal value, as a function of the surface contact angle

Globally, the conclusions are exactly the same as those from the analyze developed here-above. As expected, dryer air at 50% relative humidity allows to delay a few minutes the exchanger blocakge compared to the wetter streams. However, no clear difference is noticed between 75% and 95% humidities. It suggests that when a certain humidity level is reached, the frost formation process is evolving in a similar way, whatever the humidity.

Looking at the impact of the fan speed on the delay before frost blockage, it is clear that the faster the longer before blockage. First, it is explained because if the air speed is higher, the heat transfer on the air side is going to be enhanced inducing a hotter surface temperature. Then, the droplets temperature from hypothetical condensates are also going to be at a higher temperature compared to a weaker air speed.

5.4.3 Impact of wettability on the performance of the heat pump

In the present thesis, the effect of surface wettability on the heat pump performance (heating capacity, COP, etc.) is not investigated. It is justified by different reasons. As seen in Figure 5.5, the *transition zone* between frost quick accretion and frost prevention is very sharp. A few degrees of the contact angle has a major impact on frost formation, when switching from hydrophobic to superhydrophobic substrate. It is then nearly on/off depending on the surface. Below a threshold contact angle value, whatever the contact angle, the frost will evolve in a same way. The frost impact on the complete cycle is then the same as for classical and well known cases of system showing no specific hydrophobic behavior. On the other hand, if a superhydrophobic surface is met in the evaporator, it is likely to completely avoid frost. Then, if steady

state conditions are met, the performance of the machine does not evolve. It is the same as studying a classical heat pump in a no-frost regime. The performance gap is then the same as the one between a classical system with frost and a system in steady-state wet or dry regime. This gap is already investigated in the literature ,and highly depends on the applications. Examples and quantification of this performance gap for heat pumps, fridges or ventilation systems are illustrated in [28, 44], [6, 19] and [27], respectively.

5.4.4 Impact of wettability on the design of the evaporator

Now that the new model of heat exchanger accounting for wettability shows the interest of the technology (i.e. superhydrophobic coating), a tool is available for the design of such devices. Indeed, thanks to a (super-)hydrohpobic coating, the frost accretion drastically differs from standard heat exchangers. Furthermore, as the condensates shape is closer to a sphere, they have a deeper interaction with the air flux and a smaller influence from the surface temperature on which they are. In the light of this, it may be possible to, among others, take advantage of the air speed to heat up the droplets and avoid them to freeze.

The present thesis stops at showing the interest of superhydrophobic coatings in heat exchangers and aims at developing a simulation tool experimentally validated. No deep investigation in heat exchanger design is conducted here. However, the impact of the design on the performance of the device is illustrated with an example. The original evaporator studied is taken as the reference. Then, everything else being identical, the number of fins is modified, to increase or decrease the fin pitch. The idea here is to impose the same volumetric flowrate, whatever the number of fins. It means that the fan speed must be adjusted, its consumption will vary and the initial air pressure drop is going to change as well. Furthermore, playing with the number of fins obviously impacts the exchange surface on the air side. All these quantities are illustrated here.

The quantity of fins vary from 56 to 210, resulting in a fin pitch ranging between 5 and 1.3 mm, respectively.

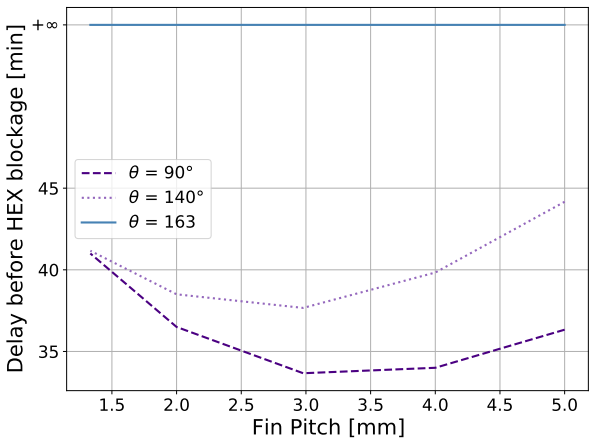

FIGURE 5.7: Time necessary needed for the air flowrate to fall under 25% of its nominal value, in function of the the fin pitch for different contact angles

Figure 5.7 shows that for superhydrophobic coating (i.e. the same one as experimentally tested on the simple surface), the evaporator will never frost, whatever the configuration. The design of the device will then be the same as frost-free heat exchanger. Then, two other contact angles are considered. The first one corresponds to neutral wettablility (90°) and the other one is intermediate with a 140° contact angle. Both curves show similar shapes with a minimum around a fin pitch of around 3 mm. For smaller fin pitch, the air speed is sufficiently high to heat droplets and delay frost formation. For larger ones, the space between fins is higher, also postponing air blockage (as the frost layer needs to be thicker). The minimum is however the same for both contact angles. It means that being neutral or hydrophobic does not impact significantly the design method. However, superhydrophobic coatings allow to prevent frost formation and may imply other designs.

Beside the time delay before blockage, other important quantities are to be considered, such as the air pressure drop, the consumption of the fan or the heat transfer rate, as illustrated in Figure 5.8.

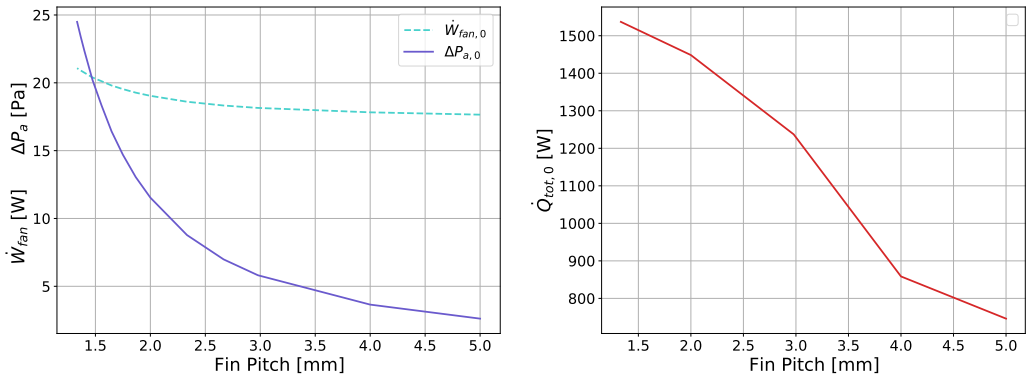

FIGURE 5.8: Air pressure drop and fan consumption (left) and heat transfer rate (right) as a function of the the fin pitch, before frost apparition

Here, to consider a consistent basis of comparison, only the values at the start of the simulations are considered (i.e. without frost). The results are relatively obvious with a decrease of all three quantities, namely the fan power, air pressure drop and heat transfer rate, with the fin pitch increase. This is explained because of an increase of the air cross section area and a decrease of the air exchange surface. As for every design process, the choice of the number of fins will eventually result in a trade-off.

5.5 Summary and conclusions

This chapter aimed at merging heat exchanger and surface models and use this new tool to quantify the performance of coated evaporators. First, the impact of the roughness on the nucleation time for different contact angles was studied. It has been observed that the model was extremely sensitive to this roughness. To set this sensitivity aside, the roughness was set constant for the rest of this chapter. The only parameter envisaged was the static contact angle. The hysteresis contact angle was considered linear between the two experimental values, which is physically meaningful. Even if different quantities were computed regarding the contact angle, the main one studied was the delay before getting the heat exchanger blocked. The general conclusion of all these results was that the hydrophobic coatings showing a

static contact angle between 90° and 130° had no significant impact on the results. In other words, a hydrophobic or a classical heat exchanger did not differ in terms of performance. However, at the threshold value of 130°, the frost delay increased exponentially while increasing the static contact angle. It means that considering superhydrophobic coatings in heat exchanger could completely prevent frost, in the considered conditions. In a next step, a first illustration of heat exchanger design was shown, changing the number of fins for different coatings. Eventually, it resulted in the fact that a superhydrophobic evaporator could be designed as a dry or wet one while the trends are similar for classical and hydrphobic exchangers.

Chapter 6

Conclusions and perspectives

The aim of this thesis was to quantify the impact of hydrophobic and superhydrophobic coatings on the surface of evaporator submitted to frost conditions. The general approach was to work in parallel on two different aspects and merge them in a last step. These aspects are namely the characterization of a standard evaporator from a heat pump and the characterization of specific surfaces showing simple geometries. For both of them, models were developed and successfully validated with data gathered through different experimental campaigns.

The different bricks building this thesis are briefly recalled here, highlighting the main outcomes of each one. Finally, different perspectives to enhance and continue the work achieved in this thesis are proposed.

6.1 Chapter 2 : Experimental investigations

This chapter aimed at describing two experimental test campaigns. The first one was related to the investigation of a fins and tubes evaporator of a heat pump while the objective of the second one was the characterization of frost formation on simple surfaces showing different wettabilities (i.e. different coatings).

First the description of the test bench built for the heat exchanger investigations was detailed. All the data monitoring system was detailed. Beside the classical sensors, the key elements to underline on this set up were linked to the specific study of frost. An innovative mass differential system has been installed. It allowed to weight the complete set up and then to get rid of potential mass variation of refrigerant within the evaporator. Meanwhile, it gave the possibility to use a 2 kg sensor to get an accurate mass measurement of the accumulated frost. This specific measurement system allowed to crosscheck the mass deduced via the humidity balance on the air flow stream. Furthermore, the uncertainty of this measurement was much lower compared to the humidity balance. However, the uncertainty on the heat transfer rate was of the same order of magnitude for both techniques.

The shell of evaporator has been modified to change the aluminum plated by transparent polymer. It allowed to obtain a visual access to the top and bottom tubes of the device and their corresponding fins. Pictures were taken at regular intervals during the complete duration of the tests. It highlighted a specific apparition scheme of the frost common to the complete set of tests. The frost appeared first on the tube corresponding to the air outlet. Then, other tubes frosted successively, from the air outlet to the air inlet. Those pictures were analyzed through a dedicated software to obtain the frost thickness of the different tests. This test campaign allowed to understand how the frost formation occurs in this system and provided a data set to

feed numerical models.

In parallel, the condensation on plane surfaces showing different coatings were experimentally investigated. The samples were installed in a conditioned atmosphere and were cooled down with a peltier thermoelectric cell. The objective was to take pictures every 20 seconds during the whole test duration to determine the time necessary to cover the complete sample with frost. In other words, the goal was to measure the nucleation phase duration. Numerical tools were implemented to measure, based on the picture analysis, this period. Those tools were based on pixels difference and pixels standard deviation.

The first main conclusion of this campaign was that no difference was spotted between neutral aluminum surface and and the ones with coatings showing static contact angles up to 115°. Such hydrophobic coatings did not show any interest for this application. To go a step further, superhydrophobic paint with a static contact angle of 162° was applied. A clear difference was then observed. For cold surface temperatures (between -8°C and -11°C), an additional delay was observed, compared to aluminum. For higher temperatures (between -5°C and -8°C), while frost was observed on the aluminum sample, the condensates appearing on the superhydrophobic coating stayed at the liquid state. It could be concluded that in the considered test conditions, the superhydrophobic coating prevents frost.

6.2 Chapter 3 : Modeling development

The very next step was to express the experimental observation through numerical models, based on physical equations. The method adopted was the same as for the test campaigns, namely tackle the task in differentiating the heat exchanger and surface phenomena.

Based on the observations of frost formation distribution in the evaporator, it was seen that frost did not appeared simultaneously on the different rows. However, for a given row, the frost distribution was rather uniform. The chosen discretization level was then tube-by-tube, to ensure the differentiation between each one of them and decrease the complexity compared to more detailed models. The model was semi-empirical, using equations from heat transfer, hydraulic and thermodynamic theories. On the refrigerant side, each tube could either be completely in two-phase, completely in vapor, or a mix between both, with a moving boundary. On the air side, each tube (and its corresponding fins) was either dry (i.e. no frost or condensation), wet (i.e. condensation on the whole tube) or frosted. For every condition, specific equations were implemented.

In this model, even if general quantities such as heat transfer rate, pressure drop predictions, etc. were correctly predicted, the frost distribution was not. To overcome this issue, an additional phenomenon, neglected in most of the models from the literature, was added to the modeling, in the name of fin thermal conductivity. Even if the concept is simple (i.e. heat conduction through aluminum plates, driven by a temperature difference), it added a lot of numerical complexity. It was then decided to use a dynamic model, to get rid of those issues. In such a way, it was possible to decouple the air from the refrigerant numerical scheme, with the wall as a capacitive interface. It was seen in the very next chapter that this new model, based on classical

equations with this add-on, gave very satisfying results.

The model previously described did not account for any hydrophobic specificity of the surface on the air side. Even if the ultimate objective was to obtain a simulation tool of heat exchanger showing hydrophobic characteristics, a model of simple surface was first implemented. This followed the same trend as for the experimental investigations. The main goal here was to describe nucleation of water from surrounding air on cold surfaces showing different features (i.e. different contact angles, roughness or inclination). The implemented equations were based on the Gibbs equations and on classical nucleation theory. All phenomena were not included in this model to keep it at a relatively low level of complexity, that would allow to merge it with the already complex heat exchanger model in a next step. The model predicted the rate of nucleation and the size of the nuclei (it allowed to predict how much time was necessary to cover a given surface). Furthermore, depending on atmospheric conditions, surface temperature and surface characteristics, the model predicted the temperature of the droplets. It showed that even for very cold surface temperature (-10°C), if the surface was sufficiently hydrophobic, it would lead to a spherical droplet shape and to higher droplet temperature, preventing the nucleus to frost. To sum up, the model allowed to compute if frost would appear on the surface or not, and if so, to predict the time necessary to completely cover the surface (i.e. nucleation time). In other words, it computed the nucleation phase duration, for given conditions and surface characteristics. Even if it was not the most detailed model at the surface level, it was built in a way that ease the merging with the macroscopic model of the heat exchanger.

Before merging those new models both of them were experimentally validated, independently. That was the topic of the next chapter.

6.3 Chapter 4 : Experimental validation

To give some credits to the newly developed models, a validation step has been conducted. The objective of this chapter was to challenge the numerical results with the collected data to certify their validity. As the built models were semi-empirical ones, some freedom degrees (i.e. tuning parameters) were available, to tune them and refine their predictions.

For the heat exchanger, the very first step was to determine a method for the model tuning. The different parameters had their specific role based on the physics but could have a global impact on the model. Because of the complexity an iterative method has been employed and described in the chapter. Then, a successive comparison between numerical and experimental results was exposed. Steady state regimes corresponding to dry or wet (no frost) states on the air side were first tackled. The heat transfer rates were well predicted within 5% and 15% for the total and sensible or latent ones, respectively. The same order of magnitude concerning the prediction accuracy was found for fluids pressure drops on refrigerant or air sides. Regarding the frost regime, the results were also satisfying, for a majority of the tests. Here, as it was not purely steady state, temporal approach was also added to the analysis. It has been observed that the few diverging results were encountered at the end of few tests, for heat exchangers heavily charged in frost presenting extremely low refrigerant flow rates and high air pressure drop. However, before reaching those critical conditions, the model was performing well. Regarding the condensates or frost mass accumulated

in the device, the simulation results were encouraging.

The ultimate check operated in this chapter for the heat exchanger was the frost distribution in the exchanger. It was the opportunity to illustrate the impact of fin thermal conductivity on predictions. When not considering this physical effect, it has been confirmed that the distribution was not well represented. The frost appeared and grew too close to the air supply, compared to observations. If the simulations were accounting for the fin thermal conductivity, this distribution issue was corrected, given far better results. It confirmed that this add-on had a considerable value in the new model. To sum up, globally, the model was successfully validated in dry, wet and frost conditions, for all different aspects.

The validation of the surface model was much more succinct because only one main output was measured, namely the duration of the nucleation phase. It is important to remember that the measurement technique was not as easy as for classical sensors, because it was based on numerical analysis of pictures. The accuracy of the experimental results is therefore lower and uncertainty unknown. On the numerical side, the model presented was a first version of this kind which can be easily plugged in the exchanger simulation tool. Nevertheless, the adequacy between numerical and experimental results was fairly satisfying, within a 20% deviation for the majority of the tests. The model was able to predict the absence of frost formation. In the opposite case, when frost is observed, the length of nucleation phase was relatively well computed too.

Based on those results, it is descent to conclude that both models were successfully validated and could be used with trust, in conditions similar to the experimental campaigns. In the next chapter, the objective was to merge and exploit those numerical tools.

6.4 Chapter 5 : Multiscale merge

This ultimate chapter, as previously recalled, aimed at merging the heat exchanger and the surface models. Even if the models were built to be merged as easily as possible, the first step was to show how those interact together.

As described in Chapter 3, the two main characteristics of the surface model were the contact angle and the roughness. Both were here studied independently. The model showed an extreme sensitivity to the roughness. Different performance maps were drawn varying the roughness, but for the rest of the chapter it was set to a value determined in Chapter 4. The most studied parameter was the static contact angle. It has been decided that the hysteresis contact angle was linearly dependent on the static one. In the present context, the most significant value to study was time before the heat exchanger was blocked because of frost, regarding the contact angle. To get closer to the actual application, a model of a fan has been implemented. The idea was to set a rotational speed constant, and observe the air flowrate decrease with the pressure drop increase. The criteria imposed to prevent any numerical issue was to consider the heat exchanger blocked when its flowrate felt under 25% of the initial one. The effect of ambient temperature, humidity or fan speed (and thus air mass flowrate) were investigated independently. But the capital information underlined in

this chapter is the following one. First, if hydrophobic coating presented a static contact angle under 130°, no visible effects was observed compared to the original one. However, at this threshold value, increasing the angle value resulted in an additional delay, growing exponentially. In practice, it meant that for superhydrophobic coatings which were well above this value, it was possible to considerably increase the frost delay or even prevent frost, for the tested conditions.

In the light of this information, a very first step in the design of heat exchangers accounting for their wettability was illustrated. The idea here was to vary the number of fins, everything else being kept constant. The main output was that for classical and hydrophobic evaporators, the conclusions were exactly the same. However, for devices with superhydrophobic coatings, the design should be considered as if the evaporator was always dry, whatever the conditions.

6.5 Perspectives

The present thesis was a first step in trying to merge two different scales, to underline the effect of hydrophobic coatings in refrigeration systems. It was, to the best author's knowledge, the first macroscopic model accounting for surface phenomena. Based on this latter, different conclusions could be successfully drawn. However, a lot of work is still to be achieved. The most obvious tasks to directly continue this thesis are listed here under:

- On the level of the classical heat exchanger (without accounting for wettability), the investigations were already deep and in alignment with the state of the art. However, this is not the case at the surface level. Further investigations should be conducted :
  - On the experimental side : the idea of studying simple surfaces was fruitful. However, investigations should continue to get deeper in the understanding of the complex phenomenon which is nucleation. Different conditions should be tackled and important tests that should be undertaken are tests with vertical samples. This would be closer to the final application;
  - On the modeling side : even if the numerical tool presented here gave already satisfying results, it should be considered as a preliminary model. Different physical phenomena were not included. The most striking ones that are not accounted for are are the statistical approach and the droplets growth model. Multiple other ones could be added, but with the two already aforementioned, better results should be reached;
- Another direct work that should be conducted is to realize the same experimental campaign as done with the classical heat exchanger, but with tubes and fins coated with superhydrpohobic paint. It would allow to validate the complete model presented in the Chapter 5. The difficulty here is to apply a uniform layer of coating on a complex geometry. One idea would be to coat it before assembling of the different elements;
- An additional improvement of this work would be to get a more efficient numerical scheme. Indeed, on a regular machine (processor 2,5 GHz Quad-Core Intel Core i7), a given point took between one and two seconds to converge. As frost appears after few minutes to few hours, one given geometry would take hours

to complete the simulation. Now, if design optimization is the ultimate goal, hundreds geometries could be tested, exploding the computation time.

- Finally, one huge improvement would be to develop a coating resistant to frost/defrost cycles. Indeed, this work showed that those could completely prevent evaporators from frost. However, the different surface samples showed a quick degradation of the superhydrophobic coating. It was replaced after three tests before going to the next ones. In real life machines it would be unthinkable to renew the coating periodically. Even if it is out of the scope of thermodynamics and more related to chemical engineering, it would represent a huge add-on in the refrigeration systems.

To conclude this work as it started, all in all, this thesis is just another brick in the wall.

Appendix A

Experimental frost thickness measurement

This appendix allows the reader to access the experimental data of the frost thickness recording. As a recall, here is the tube nomenclature.

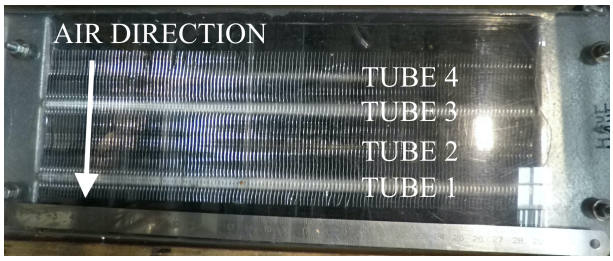

FIGURE A.1: Tubes nomenclature

.

TABLE A.1: Frost thickness on different tubes [mm]

Test #	**Tube** #	**10 min**	**20 min**	**30 min**	**40 min**	**50 min**	**60 min**	**70 min**	**80 min**	**90 min**	**100 min**	**110 min**	**120 min**	**130 min**
1	T1	0	0	0	0	0	0	0	0	0	0	0	0	0
	T2	0	0	0	0	0	0	0	0	0	0	0	0	0
	T3	0	0	0	0	0	0	0	0	0	0	0	0	0
	T4	0	0	0	0	0	0	0	0	0	0	0	0	0
2	T1	0	0	0	0	0.6	0.71	-	-	-	-	-	-	-
	T2	0	0	0	0	0	0	-	-	-	-	-	-	-
	T3	0	0	0	0	0	0	-	-	-	-	-	-	-
	T4	0	0	0	0	0	0	-	-	-	-	-	-	-
3	T1	0	0	0.45	0.6	0.63	1	1	1	1	1	1	1	1
	T2	0	0	0.32	0.47	0.57	0.72	1	1	1	1	1	1	1
	T3	0	0	0	0.2	0.29	0.33	0.54	0.72	0.8	0.86	1	1	1
	T4	0	0	0	0	0	0	0	0	0	0.1	0.31	0.33	0.35
4	T1	0	0	0	0	0	-	-	-	-	-	-	-	-
	T2	0	0	0	0	0	-	-	-	-	-	-	-	-
	T3	0	0	0	0	0	-	-	-	-	-	-	-	-
	T4	0	0	0	0	0	-	-	-	-	-	-	-	-
5	T1	0	0	0.45	0.5	0.56	0.73	0.8	0.96	-	-	-	-	-
	T2	0	0	0	0.27	0.48	0.52	0.55	0.62	-	-	-	-	-
	T3	0	0	0	0	0	0.15	0.205	0.27	-	-	-	-	-
	T4	0	0	0	0	0	0	0	0	-	-	-	-	-

Continued on next page

Table A.1 – continued from previous page

Test #	Tube #	10 min	20 min	30 min	40 min	50 min	60 min	70 min	80 min	90 min	100 min	110 min	120 min	130 min
6	T1	0	0	0.44	0.48	0.61	0.8	1	-	-	-	-	-	-
	T2	0	0	0	0	0	0.26	0.32	-	-	-	-	-	-
	T3	0	0	0	0	0	0	0	-	-	-	-	-	-
	T4	0	0	0	0	0	0	0	-	-	-	-	-	-
7	T1	0	0	0	0.3	0.62	0.66	0.98	1	1	-	-	-	-
	T2	0	0	0	0	0	0	0	0.23	0.51	-	-	-	-
	T3	0	0	0	0	0	0	0	0	0.2	-	-	-	-
	T4	0	0	0	0	0	0	0	0	0	-	-	-	-
8	T1	0	0	0	-	-	-	-	-	-	-	-	-	-
	T2	0	0	0	-	-	-	-	-	-	-	-	-	-
	T3	0	0	0	-	-	-	-	-	-	-	-	-	-
	T4	0	0	0	-	-	-	-	-	-	-	-	-	-
9	T1	0	0.44	0.5	0.56	0.67	0.94	0.96	1	-	-	-	-	-
	T2	0	0	0	0.2	0.47	0.65	0.7	0.71	-	-	-	-	-
	T3	0	0	0	0	0	0	0.18	0.24	-	-	-	-	-
	T4	0	0	0	0	0	0	0	0	-	-	-	-	-
10	T1	0	0	0.23	0.29	0.34	-	-	-	-	-	-	-	-
	T2	0	0	0	0	0	-	-	-	-	-	-	-	-
	T3	0	0	0	0	0	-	-	-	-	-	-	-	-
	T4	0	0	0	0	0	-	-	-	-	-	-	-	-
11	T1	0	0	0.47	0.54	0.59	0.73	0.8	0.95	1	1	1	1	1
	T2	0	0	0	0	0	0.175	0.36	0.46	0.52	0.6	0.83	1	1
	T3	0	0	0	0	0	0	0	0.14	0.27	0.28	0.3	0.41	0.47
	T4	0	0	0	0	0	0	0	0	0	0	0	0	0
12	T1	0	0	0	0.17	0.26	0.28	-	-	-	-	-	-	
	T2	0	0	0	0	0	0	0	-	-	-	-	-	-
	T3	0	0	0	0	0	0	0	-	-	-	-	-	-
	T4	0	0	0	0	0	0	0	-	-	-	-	-	-
13	T1	0	0	0	0	-	-	-	-	-	-	-	-	-
	T2	0	0	0	0	-	-	-	-	-	-	-	-	-
	T3	0	0	0	0	-	-	-	-	-	-	-	-	-
	T4	0	0	0	0	-	-	-	-	-	-	-	-	-
14	T1	0	0	-	-	-	-	-	-	-	-	-	-	-
	T2	0	0	-	-	-	-	-	-	-	-	-	-	-
	T3	0	0	-	-	-	-	-	-	-	-	-	-	-
	T4	0	0	-	-	-	-	-	-	-	-	-	-	-
15	T1	0.22	0.57	0.67	0.74	0.85	1	1	1	1	1	1	1	1
	T2	0	0	0.2	0.4	0.5	0.69	0.75	0.89	1	1	1	1	1
	T3	0	0	0	0	0	0.29	0.4	0.54	0.56	0.85	0.96	1	1
	T4	0	0	0	0	0	0	0	0	0	0	0.33	0.36	0.55
16	T1	0	0.48	0.66	0.79	0.92	1	1	1	-	-	-	-	-
	T2	0	0	0	0	0.1	0.4	0.5	0.6	-	-	-	-	-
	T3	0	0	0	0	0	0	0	0.21	-	-	-	-	-
	T4	0	0	0	0	0	0	0	0	-	-	-	-	-
17	T1	0	0	0.31	0.61	-	-	-	-	-	-	-	-	-
	T2	0	0	0	0	-	-	-	-	-	-	-	-	-
	T3	0	0	0	0	-	-	-	-	-	-	-	-	-
	T4	0	0	0	0	-	-	-	-	-	-	-	-	-

Continued on next page

Table A.1 – continued from previous page

Test #	**Tube** #	**10 min**	**20 min**	**30 min**	**40 min**	**50 min**	**60 min**	**70 min**	**80 min**	**90 min**	**100 min**	**110 min**	**120 min**	**130 min**
18	T1	0	0	0	0	-	-	-	-	-	-	-	-	-
	T2	0	0	0	0	-	-	-	-	-	-	-	-	-
	T3	0	0	0	0	-	-	-	-	-	-	-	-	-
	T4	0	0	0	0	-	-	-	-	-	-	-	-	-
19	T1	0	0	0	0	0	0	0	-	-	-	-	-	-
	T2	0	0	0	0	0	0	0	-	-	-	-	-	-
	T3	0	0	0	0	0	0	0	-	-	-	-	-	-
	T4	0	0	0	0	0	0	0	-	-	-	-	-	-
20	T1	0	0	0.6	0.61	0.7	1	1	1	1	1	-	-	-
	T2	0	0	0	0	0.59	0.7	1	1	1	1	-	-	-
	T3	0	0	0	0	0	0.26	0.28	0.5	0.79	0.81	-	-	-
	T4	0	0	0	0	0	0	0	0	0	0	-	-	-

Appendix B

Refrigerant heat transfer coefficient in boiling phase

This appendix details the Kandlikar [41] developments for deducing the heat transfer coefficient of boiling refrigerant in an horizontal tube for **low mass fluxes**.

$$\frac{H_{\text{ref,2P}}}{H_{\text{ref,L}}} = C_1 \cdot Co^{C_2} \cdot (25 \cdot Fr_{lo})^{C_5} + C_3 \cdot Bo^{C_4} \cdot F_{fl} \tag{B.1}$$

$H_{\text{ref,L}}$ represents the single phase (liquid) heat transfer coefficient.

$$H_{\text{ref,L}} = 0.023 \cdot Re_L^{0.8} \cdot Pr_L^{0.4} \cdot \frac{k_L}{D_{\text{in}}} \tag{B.2}$$

Co represents the convection number, defined by:

$$Co = \left(\frac{1-x}{x}\right)^{0.8} \cdot \left(\frac{\rho_G}{\rho_L}\right)^{0.5} \tag{B.3}$$

The different coefficient are empirical and summed up in Table B.1

Table B.1: Convective heat transfer coefficients

Constant	**Convective region**	**Nucleate boiling region**
C_1	1.1360	0.6683
C_2	-0.9	-0.2
C_3	667.2	1058
C_4	0.7	0.7
C_5	0.3	0.3

As seen in the Table B.1, to sets of coefficient are determined, depending on the regime. The trick used is to evaluate the heat transfer coefficient with both sets, whatever the conditions. Then, the maximum is taken, ensuring a continuity between both regions.

Different values of the fluid dependent correction factor F_{fl} are given in this research, but any corresponds to the R134a fluid. It is decided to be a tuning parameter of the correlation to fit the experimental data and is set to 0.75. In the paper this parameters vary between 1 for water and 4.70 for nitrogen. The order of magnitude is then considered consistent.

Appendix C

Description of the fictitious air specific heat capacity technique

This appendix presents the development developed by Lebrun et al. [47]. It allows to model a cooling coil in the situation where the air humidity condensates, in steady state.

Before this model proposition, Braun [10] proposed a similar model. It is based on two simplifications:

1. "*linearization of the relationship between saturated air enthalpy and corresponding temperatures;*"[47].

2. "*definition of two possible regimes : coil fully dry ot fully wet.*"[47].

The model of Lebrun is a generalization of the proposition of Braun, using wet-bulb air temperature T_{wb} as diving potential instead of the enthalpies. Looking at the equations for a dry case, considering an infinitesimal heat exchange between the air and the cold surface, it can be written :

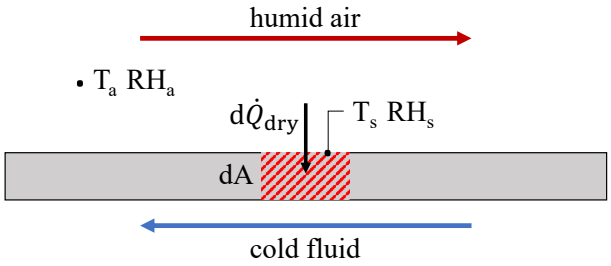

FIGURE C.1: Schematic of an infinitesimal heat transfer in dry regime

$$\mathrm{d}\dot{Q}_{\mathrm{dry}} = \mathrm{d}A \cdot \frac{1}{R_a} \cdot (T_a - T_s) \tag{C.1}$$

In wet regime, it is slightly more complex because of the simultaneous heat and mass transfer. To express the energy transfer between the air and the surface, the enthalpies are used, to account for simultaneous sensible and latent contributions.

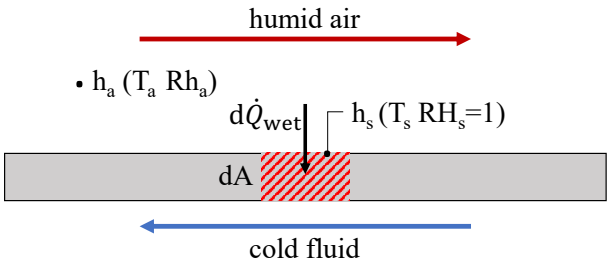

FIGURE C.2: Schematic of an infinitesimal heat transfer in wet regime

$$\mathrm{d}\dot{Q}_{\mathrm{wet}} = \mathrm{d}A \cdot \frac{1}{R_a \cdot cp_a} \cdot (h_a - h_s) \tag{C.2}$$

$$\mathrm{d}\dot{Q}_{\mathrm{wet}} = \mathrm{d}A \cdot \frac{1}{R_a \cdot cp_a} \cdot (h(T_a, RH_a) - h(T_s, RH_1)) \tag{C.3}$$

Looking at the psychrometric diagram in Figure C.3, it is seen that the air isenthalpy lines are parallel to the iso-wet bulb temperatures (i.e. yellow and red isolines are overlapped).

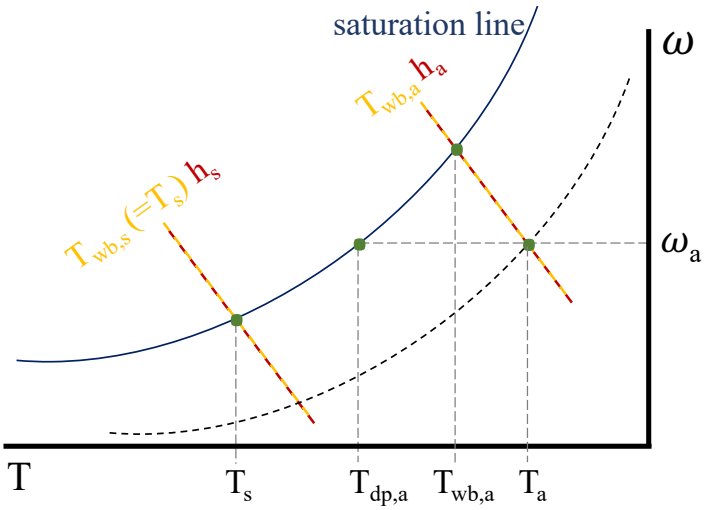

FIGURE C.3: Psychrometric diagram

From this observation, and noticing that $T_{wb,s} = T_s$, the previous equation can be written as :

$$\mathrm{d}\dot{Q}_{\mathrm{wet}} = \mathrm{d}A \cdot \frac{1}{R_a \cdot cp_a} \cdot (h(T_{wb,a}, RH_1) - h(T_s, RH_1)) \tag{C.4}$$

remembering the simplification 1., considering that the enthalpy is linearly proportional to the corresponding wet bulb temperature :

$$\mathrm{d}\dot{Q}_{\mathrm{wet}} = \mathrm{d}A \cdot \frac{1}{R_a} \cdot \frac{cp_{fict}}{cp_a} \cdot (T_{wb,a} - T_s) \tag{C.5}$$

where cp_{fict} is the proportional coefficient between air and wet-bulb temperature and has the dimension of a specific heat capacity. Defining a new heat transfer resistance

on the air side $R_{a,fict} = R_a \cdot \frac{cp_a}{cp_{fict}}$, the previous equation is written as:

$$\mathrm{d}\dot{Q}_{\mathrm{wet}} = \mathrm{d}A \cdot \frac{1}{R_{a,fict}} \cdot (T_{wb,a} - T_s) \tag{C.6}$$

This expression has the exact same form as its equivalent in dry regime Eq.(C.1). At this stage, cp_{fict} still needs to be defined. From what is explained previously, it is possible to write:

$$h_a - h_s = cp_{fict} \cdot (T_{wb,a} - T_s) \tag{C.7}$$

$$cp_{fict} = \frac{h_a - h_s}{T_{wb,a} - T_s} \tag{C.8}$$

If it is assumed that cp_{fict} is constant over the coil and that at the saturation the enthalpy varies linearly with the saturation temperature, it becomes:

$$cp_{fict} = \frac{h_{a,su} - h_{a,ex}}{T_{wb,su} - T_{wb,ex}} \tag{C.9}$$

cp_{fict} being defined, it is now possible to easily compute the heating power transfer in wet regime.

Appendix D

Fan model

The chosen fan is one efficient fan used in the frame of the present application. It is a centrifugal module from EBM-PAPST, the *K3G190-RC05-03*. From the datasheet, the curves have been interpolated, giving the following equations:

For the fan pressure drop :

$$\Delta P = \left(a_0 + a_1 \cdot \left(\dot{V} \cdot \frac{N_{ref}}{N \cdot \dot{V}_{max}} \right) + a_2 \cdot \left(\dot{V} \cdot \frac{N_{ref}}{N \cdot \dot{V}_{max}} \right)^2 + a_3 \cdot \left(\dot{V} \cdot \frac{N_{ref}}{N \cdot \dot{V}_{max}} \right)^3 \cdot \left(\frac{N}{N_{ref}} \right)^2 \right) \cdot \Delta P_{max,ref} \tag{D.1}$$

For the fan efficiency:

$$\eta = \left(b_0 + b_1 \cdot \left(\dot{V} \cdot \frac{N_{ref}}{N \cdot \dot{V}_{max}} \right) + b_2 \cdot \left(\dot{V} \cdot \frac{N_{ref}}{N \cdot \dot{V}_{max}} \right)^2 + b_3 \cdot \left(\dot{V} \cdot \frac{N_{ref}}{N \cdot \dot{V}_{max}} \right)^3 \right) \cdot \left(\frac{N}{N_{ref}} \right)^{0.5} \tag{D.2}$$

For the fan consumption power:

$$\dot{W} = \Delta P \cdot \frac{\dot{V}}{\eta \cdot 3600} \tag{D.3}$$

with the following values for the coefficients:

$a_0 = 0.9997$	$a_1 = -0.3576$	$a_2 = 0.623$	$a_3 = -1.2685$
$b_0 = 0.0009$	$b_1 = 0.7964$	$b_2 = 1.1755$	$b_3 = -1.9618$
$\dot{V}_{max} = 580$ m^3/h	$\Delta P_{max,ref} = 360$ Pa	$N_{ref} = 2800$ min^{-1}	

The fan speed is set by the model user. Then a function computes the correct air flowrate that equalizes the pressure drop of the fan and of the system. Beside the heat exchanger pressure drop, an additional pressure drop of the system (piping, compressor cooling, etc.) is imposed. It is generally between 100 and 150 Pa for the present application. A constant value of 125 Pa is added here.

Bibliography

[1] US Energy Information Administration. *Use of energy explained*. https://www.eia.gov/energyexplained/use-of-energy/homes.php. 2021.

[2] United States Environmental Protection Agency. *Sources of Greenhouse Gas Emissions*. https://www.epa.gov/ghgemissions/sources-greenhouse-gas-emissions. 2022.

[3] Saad Akhtar, Minghan Xu, and Agus P Sasmito. "Development and validation of a semi-analytical framework for droplet freezing with heterogeneous nucleation and non-linear interface kinetics". In: *International Journal of Heat and Mass Transfer* 166 (2021), p. 120734.

[4] Chris R Lawrence Andrew R Parker and. "Water capture by a desert beetle". In: *Nature* 414.1 (2001), pp. 33–34.

[5] *Ashrae Handbook of Fundamentals*. American Society of Heating, Regrigerating and Air-Conditioning Engineers, Inc, 1977.

[6] Pradeep Bansal, David Fothergill, and Ryan Fernandes. "Thermal analysis of the defrost cycle in a domestic freezer". In: *International Journal of Refrigeration* 33.3 (2010), pp. 589–599.

[7] Richard Becker and Werner Döring. "Kinetische behandlung der keimbildung in übersättigten dämpfen". In: *Annalen der Physik* 416.8 (1935), pp. 719–752.

[8] Clémentine Belaud et al. "Development of nanostructured icephobic aluminium oxide surfaces for aeronautic applications". In: *Surface and Coatings Technology* (2020), p. 126652.

[9] T.L. Bergman et al. *Introduction to Heat Transfer*. Wiley, 2011, p. 516. ISBN: 9780470501962. URL: https://books.google.be/books?id=YBaNaLurTD4C.

[10] James Braun. "Methodologies for the design and control of central cooling plants". PhD thesis. University of Winsconsin-Madison, 1988.

[11] Florent Breque. "Étude et Amélioration dune Pompe à Chaleur pour Véhicule Électrique en Conditions de Givrage". PhD thesis. MINES ParisTech, 2017.

[12] P Carroll, M Chesser, and P Lyons. "Air Source Heat Pumps field studies: A systematic literature review". In: *Renewable and Sustainable Energy Reviews* 134 (2020), p. 110275.

[13] Hong Chen, Leena Thomas, and Robert W Besant. "Fan supplied heat exchanger fin performance under frosting conditions". In: *International Journal of Refrigeration* 26.1 (2003), pp. 140–149.

[14] Chin-Hsiang Cheng and Yu-Chieh Cheng. "Predictions of frost growth on a cold plate in atmospheric air". In: *International Communications in Heat and Mass Transfer* 28.7 (2001), pp. 953–962.

[15] Fuqiang Chu et al. "Relationship between condensed droplet coalescence and surface wettability". In: *International Journal of Heat and Mass Transfer* 111 (2017), pp. 836–841.

[16] Yoong Chung et al. "Prediction of the frost growth and performance change of air source heat pump system under various frosting conditions". In: *Applied Thermal Engineering* 147 (2019), pp. 410–420.

[17] Diogo L Da Silva, Christian JL Hermes, and Claudio Melo. "Experimental study of frost accumulation on fan-supplied tube-fin evaporators". In: *Applied Thermal Engineering* 31.6-7 (2011), pp. 1013–1020.

[18] Diogo L Da Silva, Christian JL Hermes, and Claudio Melo. "First-principles modeling of frost accumulation on fan-supplied tube-fin evaporators". In: *Applied Thermal Engineering* 31.14-15 (2011), pp. 2616–2621.

[19] Dong-quan Deng, Lie Xu, and Shi-qiong Xu. "Experimental investigation on the performance of air cooler under frosting conditions". In: *Applied thermal engineering* 23.7 (2003), pp. 905–912.

[20] Remi Dickes. "Charge-sensitive methods for the off-design performance characterization of organic Rankine cycle (ORC) power systems". PhD thesis. University of Liège, 2019.

[21] P Dimitrakopoulos and JJL Higdon. "On the gravitational displacement of three-dimensional fluid droplets from inclined solid surfaces". In: *Journal of Fluid Mechanics* 395 (1999), pp. 181–209.

[22] Xuzhi Du et al. "A theoretical and experimental study of typical heterogeneous ice nucleation process on auto windshield under nocturnal radiative cooling and subfreezing conditions". In: *International Journal of Heat and Mass Transfer* 136 (2019), pp. 610–626.

[23] Bachir El Fil, Girish Kini, and Srinivas Garimella. "A review of dropwise condensation: Theory, modeling, experiments, and applications". In: *International Journal of Heat and Mass Transfer* 160 (2020), p. 120172.

[24] François Feuillebois et al. "Freezing of a subcooled liquid droplet". In: *Journal of colloid and interface science* 169.1 (1995), pp. 90–102.

[25] Neville H Fletcher. "Size effect in heterogeneous nucleation". In: *The Journal of chemical physics* 29.3 (1958), pp. 572–576.

[26] Neville Horner Fletcher. "The chemical physics of ice". In: *The Chemical Physics of Ice* (2009).

[27] Samuel Gendebien, Antoine Parthoens, and Vincent Lemort. "Investigation of a single room ventilation heat recovery exchanger under frosting conditions: Modeling, experimental validation and operating strategies evaluation". In: *Energy and Buildings* 186 (2019), pp. 1–16.

[28] Xian-Min Guo et al. "Experimental study on frost growth and dynamic performance of air source heat pump system". In: *Applied Thermal Engineering* 28.17-18 (2008), pp. 2267–2278.

[29] Y Hayashi et al. "Study of frost properties correlating with frost formation types". In: (1977).

[30] Heliotherm. *A heat pump's principle function*. https://www.heliotherm.com/en/the-heat-pump/a-heat-pumps-principle-function/. 2021.

[31] Arif Hepbasli et al. "A key review of wastewater source heat pump (WWSHP) systems". In: *Energy Conversion and Management* 88 (2014), pp. 700–722.

[32] Christian JL Hermes et al. "A semi-empirical model for predicting frost accretion on hydrophilic and hydrophobic surfaces". In: *International Journal of Refrigeration* 87 (2018), pp. 164–171.

[33] Christian JL Hermes et al. "A study of frost build-up on hydrophilic and hydrophobic surfaces under forced convection conditions". In: *Experimental Thermal and Fluid Science* 100 (2019), pp. 76–88.

[34] Christian JL Hermes et al. "A study of frost growth and densification on flat surfaces". In: *Experimental Thermal and Fluid Science* 33.2 (2009), pp. 371–379.

[35] IEA. *Heat Pumps*. https://www.iea.org/reports/heat-pumps. 2021.

[36] Haobo Jiang, Vikrant Aute, and Reinhard Radermacher. "CoilDesigner: a general-purpose simulation and design tool for air-to-refrigerant heat exchangers". In: *International Journal of Refrigeration* 29.4 (2006), pp. 601–610.

[37] Jie Ju et al. "A multi-structural and multi-functional integrated fog collection system in cactus". In: *Nature communications* 3.1 (2012), pp. 1–6.

[38] Stefan Jung, Manish K Tiwari, and Dimos Poulikakos. "Frost halos from supercooled water droplets". In: *Proceedings of the National Academy of Sciences* 109.40 (2012), pp. 16073–16078.

[39] Stefan Jung et al. "Mechanism of supercooled droplet freezing on surfaces". In: *Nature communications* 3.1 (2012), pp. 1–8.

[40] Vitaly I Kalikmanov. "Classical nucleation theory". In: *Nucleation theory*. Springer, 2013, pp. 17–41.

[41] Satish G Kandlikar. "A general correlation for saturated two-phase flow boiling heat transfer inside horizontal and vertical tubes". In: (1990).

[42] Donghee Kim et al. "Experimental investigation of frost retardation for superhydrophobic surface using a luminance meter". In: *International Journal of Heat and Mass Transfer* 87 (2015), pp. 491–496.

[43] Donghun Kim, James E Braun, and Sugirdhalakshmi Ramaraj. "Computationally efficient modeling strategy for evaporator performance under frost conditions". In: *International Journal of Refrigeration* 96 (2018), pp. 88–99.

[44] Elias Kinab et al. "Reversible heat pump model for seasonal performance optimization". In: *Energy and Buildings* 42.12 (2010), pp. 2269–2280.

[45] SA Kulinich et al. "Superhydrophobic surfaces: are they really ice-repellent?" In: *Langmuir* 27.1 (2011), pp. 25–29.

[46] Alexandre Laroche et al. "Silicone nanofilaments grown on aircraft alloys for low ice adhesion". In: *Surface and Coatings Technology* 410 (2021), p. 126971.

[47] J Lebrun et al. "Cooling Coil Models to be used in Transient and/or Wet Regimes. Theoretical Analysis and Experimental Validation". In: *Proceedings of SSB*. 1990.

[48] Kwan-Soo Lee, Woo-Seung Kim, and Tae-Hee Lee. "A one-dimensional model for frost formation on a cold flat surface". In: *International Journal of Heat and Mass Transfer* 40.18 (1997), pp. 4359–4365.

[49] Won-Jong Lee, Kyung Jin Bae, and Oh Kyung Kwon. "Effect of hydrophobic surfaces on frost retardation in fin-tube heat exchangers with various fin pitches". In: *Applied Thermal Engineering* 176 (2020), p. 115424.

[50] Aurélia Léoni et al. "State-of-the-art review of frost deposition on flat surfaces". In: *international journal of refrigeration* 68 (2016), pp. 198–217.

[51] Liyan Li et al. "The theoretical analysis and experimental study on anti-frosting performance of surface characteristics". In: *International Journal of Thermal Sciences* 137 (2019), pp. 343–351.

[52] Jian Liu et al. "A general steady state mathematical model for fin-and-tube heat exchanger based on graph theory". In: *International Journal of Refrigeration* 27.8 (2004), pp. 965–973.

[53] XY Liu. "Heterogeneous nucleation or homogeneous nucleation?" In: *The Journal of Chemical Physics* 112.22 (2000), pp. 9949–9955.

[54] Zhongliang Liu et al. "Frost formation on a super-hydrophobic surface under natural convection conditions". In: *International Journal of Heat and Mass Transfer* 51.25-26 (2008), pp. 5975–5982.

[55] Jin Luo et al. "A review of ground investigations for ground source heat pump (GSHP) systems". In: *Energy and Buildings* 117 (2016), pp. 160–175.

[56] Xiang Ma et al. "Condensation and Evaporation Heat Transfer Characteristics of Low Mass Fluxes in Horizontal Smooth Tube and Three-Dimensional Enhanced Tubes". In: *Journal of Thermal Science and Engineering Applications* 12.2 (2020), p. 021016.

[57] Prafulla Chandra Mahata. *The Effect of Contact Angle, Surface Roughness, and Adsorption on Heterogeneous Nucleation of Condensing Water*. University of Missouri-Rolla, 1974.

[58] R Mastrullo et al. "Transient model of a vertical freezer with door openings and defrost effects". In: *Applied energy* 121 (2014), pp. 38–50.

[59] LU Menglong et al. "A modeling study of sessile water droplet on the cold plate surface during freezing under natural convection with gravity effect considered". In: *International Journal of Multiphase Flow* 143 (2021), p. 103749.

[60] Matt S Mitchell and Jeffrey D Spitler. "Open-loop direct surface water cooling and surface water heat pump systems: A review". In: *HVAC&R Research* 19.2 (2013), pp. 125–140.

[61] Masashi Miwa et al. "Effects of the surface roughness on sliding angles of water droplets on superhydrophobic surfaces". In: *Langmuir* 16.13 (2000), pp. 5754–5760.

[62] Ehsan Moallem et al. "Experimental measurements of the surface coating and water retention effects on frosting performance of microchannel heat exchangers for heat pump systems". In: *Experimental Thermal and Fluid Science* 39 (2012), pp. 176–188.

[63] A Morales-Fuentes et al. "Analysis of the heat transfer area distribution in a frosted plain fin-and-tube geometry". In: *International Journal of Refrigeration* 75 (2017), pp. 26–37.

[64] Byeongchul Na and Ralph L Webb. "A fundamental understanding of factors affecting frost nucleation". In: *International Journal of Heat and Mass Transfer* 46.20 (2003), pp. 3797–3808.

[65] Saurabh Nath and Jonathan B Boreyko. "On localized vapor pressure gradients governing condensation and frost phenomena". In: *Langmuir* 32.33 (2016), pp. 8350–8365.

[66] Kashif Nawaz and Brian Fricke. "A Critical Literature Review of Defrost Technologies for Heat Pumps and Refrigeration System". In: *Proceedings of 18th International Refrigeration and Air Conditioning Conference at Purdue*. 2021.

[67] Linda Oberli et al. "Condensation and freezing of droplets on superhydrophobic surfaces". In: *Advances in colloid and interface science* 210 (2014), pp. 47–57.

[68] DL O'neal and DR Tree. "A review of frost formation in simple geometries". In: *Ashrae Transactions* 91.2A (1985), pp. 267–281.

[69] Robson O Piucco et al. "A study of frost nucleation on flat surfaces". In: *Experimental Thermal and Fluid Science* 32.8 (2008), pp. 1710–1715.

[70] Chao Chris Qin, Alan T Mulroney, and Mool C Gupta. "Anti-icing epoxy resin surface modified by spray coating of PTFE Teflon particles for wind turbine blades". In: *Materials Today Communications* 22 (2020), p. 100770.

[71] Frédéric Ransy, Samuel Gendebien, and Vincent Lemort. "Modelling of an exhaust air heat pump used for heating and domestic hot water production". English. In: *Proceedings of the 10th International Conference on System Simulation in Buildings*. Liege, Belgium, 2020.

[72] Saikat Sinha Ray et al. "Fluorine-free anti-droplet surface modification by hexa decyltrimethoxysilane-modified silica nanoparticles-coated carbon nanofibers for self-cleaning applications". In: *Progress in Organic Coatings* 153 (2021), p. 106165.

[73] Grand View Research. *Heat Pump Market Size, Share and Trends Analysis Report By Technology (Water Source, Air Source, Ground Source), By Application (Residential, Industrial, Commercial), By Region, And Segment Forcasts, 2019 - 2025*. Grand View Research, 2019.

[74] Paul Roach, Neil J Shirtcliffe, and Michael I Newton. "Progess in superhydrophobic surface development". In: *Soft matter* 4.2 (2008), pp. 224–240.

[75] Ricardo Romero-Méndez et al. "Effect of tube-to-tube conduction on plate-fin and tube heat exchanger performance". In: *International journal of heat and mass transfer* 40.16 (1997), pp. 3909–3916.

[76] C. Sanders. "The influence of frost formation and defrosting on the performance of air coolers". In: 1974.

[77] Ioan Sarbu and Calin Sebarchievici. "General review of ground-source heat pump systems for heating and cooling of buildings". In: *Energy and buildings* 70 (2014), pp. 441–454.

[78] Omer Sarfraz, Christian K Bach, and Craig Bradshaw. "A literature review of numerical modeling techniques for vapor compression systems with focus on heat exchanger modeling". In: (2018).

[79] Omer Sarfraz, Christian K Bach, and Craig R Bradshaw. "Discrete modeling of fin-and-tube heat exchangers with cross-fin conduction functionality". In: *International Journal of Refrigeration* 104 (2019), pp. 270–281.

[80] Stuart J Self, Bale V Reddy, and Marc A Rosen. "Geothermal heat pump systems: Status review and comparison with other heating options". In: *Applied energy* 101 (2013), pp. 341–348.

[81] Neil J Shirtcliffe et al. "Dual-scale roughness produces unusually water-repellent surfaces". In: *Advanced Materials* 16.21 (2004), pp. 1929–1932.

[82] John T Simpson, Scott R Hunter, and Tolga Aytug. "Superhydrophobic materials and coatings: a review". In: *Reports on Progress in Physics* 78.8 (2015), p. 086501.

[83] Varun Singh, Vikrant Aute, and Reinhard Radermacher. "Numerical approach for modeling air-to-refrigerant fin-and-tube heat exchanger with tube-to-tube heat transfer". In: *International Journal of Refrigeration* 31.8 (2008), pp. 1414–1425.

[84] Chang-Hyo Son et al. "Evaporation Heat Transfer and Pressure Drop of Low-Global Warming Potential Refrigerant HFO-1234yf in 6.95-mm Horizontal Smooth Tube". In: *Energies* 14.19 (2021), p. 6325.

[85] Mengjie Song and Chaobin Dang. "Review on the measurement and calculation of frost characteristics". In: *International Journal of Heat and Mass Transfer* 124 (2018), pp. 586–614.

[86] Jinchen Tang et al. "Computational modeling and prediction of the performance of air source heat pumps under frost prevention and retardation conditions". In: *Energy and Buildings* 224 (2020), p. 110264.

[87] Y-X Tao, RW Besant, and KS Rezkallah. "A mathematical model for predicting the densification and growth of frost on a flat plate". In: *International Journal of Heat and Mass Transfer* 36.2 (1993), pp. 353–363.

[88] Moussa Tembely, Reza Attarzadeh, and Ali Dolatabadi. "On the numerical modeling of supercooled micro-droplet impact and freezing on superhydrophobic surfaces". In: *International Journal of Heat and Mass Transfer* 127 (2018), pp. 193–202.

[89] *VDI Heat Atlas*. VDI-Verlag GmbH, 2010, pp. 1273–1274. ISBN: 978-3-540-77876-9.

[90] Max Volmer and Håkon Flood. "Tröpfchenbildung in Dämpfen". In: *Zeitschrift für physikalische Chemie* 170.1 (1934), pp. 273–285.

[91] C-C Wang, Y-T Lin, and C-J Lee. "An airside correlation for plain fin-and-tube heat exchangers in wet conditions". In: *International Journal of Heat and Mass Transfer* 43.10 (2000), pp. 1869–1872.

[92] Nan Wang et al. "Superhydrophobic surface on steel substrate and its anti-icing property in condensing conditions". In: *Applied Surface Science* 355 (2015), pp. 226–232.

[93] W Wang et al. "A generalized simple model for predicting frost growth on cold flat plate". In: *international journal of refrigeration* 35.2 (2012), pp. 475–486.

[94] Zuo-Jia Wang et al. "Frost formation and anti-icing performance of a hydrophobic coating on aluminum". In: *Experimental Thermal and Fluid Science* 60 (2015), pp. 132–137.

[95] Wikipedia. *Heat Pump*. https://en.wikipedia.org/wiki/Heat_pump. 2021.

[96] Wikipedia. *Thermodynamic free energy*. https://en.wikipedia.org/wiki/Thermodynamic_free_energy. 2022.

[97] Xiaomin Wu et al. "Visual and theoretical analyses of the early stage of frost formation on cold surfaces". In: *Journal of Enhanced Heat Transfer* 14.3 (2007).

[98] Yanping Xia and Anthony M Jacobi. "Air-side data interpretation and performance analysis for heat exchangers with simultaneous heat and mass transfer: wet and frosted surfaces". In: *International Journal of Heat and Mass Transfer* 48.25-26 (2005), pp. 5089–5102.

[99] YZPSY Xia et al. "Frost, defrost, and refrost and its impact on the air-side thermal-hydraulic performance of louvered-fin, flat-tube heat exchangers". In: *International Journal of Refrigeration* 29.7 (2006), pp. 1066–1079.

[100] Jian Xie et al. "Mode selection between sliding and rolling for droplet on inclined surface: Effect of surface wettability". In: *International Journal of Heat and Mass Transfer* 122 (2018), pp. 45–58.

[101] N Yamakawa, N Takahashi, and S Ohtani. "Forced convection heat and mass transfer under frost conditions". In: *Heat transfer-japanese research* 1.2 (1972), pp. 1–10.

[102] Dong-Keun Yang, Kwan-Soo Lee, and Simon Song. "Modeling for predicting frosting behavior of a fin–tube heat exchanger". In: *International journal of heat and mass transfer* 49.7-8 (2006), pp. 1472–1479.

[103] Huee-Youl Ye and Kwan-Soo Lee. "Performance prediction of a fin-and-tube heat exchanger considering air-flow reduction due to the frost accumulation". In: *International Journal of Heat and Mass Transfer* 67 (2013), pp. 225–233.

[104] Jon Daniel Yonko. "An investigation of the thermal conductivity of frost while forming on a flat horizontal plate". In: *ASHRAE transactions* 73.2 (1967), pp. 1–1.

[105] Jin Woo Yoo et al. "Determination of defrosting start time in an air-to-air heat pump system by frost volume calculation method". In: *International Journal of Refrigeration* 96 (2018), pp. 169–178.

[106] B Youn and NH Kim. "An experimental investigation on the airside performance of fin-and-tube heat exchangers having sinusoidal wave fins". In: *Heat and mass transfer* 43.12 (2007), pp. 1249–1262.

[107] Guichu Yue et al. "Bioinspired surface with special wettability for liquid transportation and separation". In: *Sustainable Materials and Technologies* (2020), e00175.

[108] Konstantin O Zamuruyev et al. "Continuous droplet removal upon dropwise condensation of humid air on a hydrophobic micropatterned surface". In: *Langmuir* 30.33 (2014), pp. 10133–10142.

[109] Martin Zogg. *History of Heat PumpsSwiss Contributions and International Milestones*. Swiss Federal Office of Energy SFOE, 2008.